Virtual Sky Surveys and Multi-wavelength Investigations of Galaxy Clusters

by

Brian D. Nord

A dissertation submitted in partial fulfillment
of the requirements for the degree of
Doctor of Philosophy
(Physics)
in The University of Michigan
2010

Doctoral Committee:

Professor August E. Evrard, Chair
Professor Fred C. Adams
Professor Timothy A. McKay
Professor Gregory Tarlé
Assistant Professor Jeffrey J. McMahon
Assistant Professor Marta Volonteri

But I guess I'd say, if it is just us ... it seems like an awful waste of space.

– Ted Arroway, *Contact*

I'd like to just continue to be able to...
express myself, as best as I can with this instrument.
I feel like I have a lot of work to do. Still, ya know
I'm a student, of the drums
And I'm also a teacher of the drums too.

– DJ Shadow, *Endtroducing*

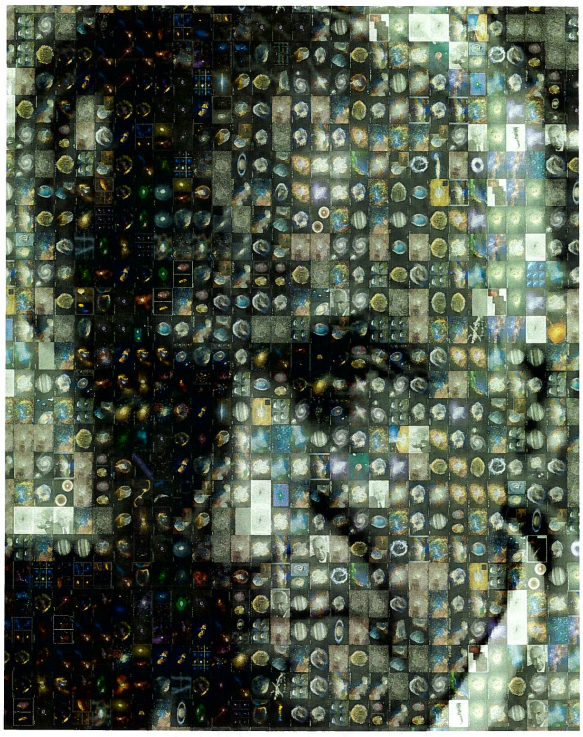

A picture of Subrahmanyan Chandrasekhar overlaid with a mosaic of astrophysical phenomena taken with the Chandra X-ray Space Observatory. Chandrasekhar is a preeminent astrophysicist of the 20th century and Nobel laureate, who contributed to our understanding of stellar evolution: in particular, he discovered the conditions required for a star to become a black hole. He persisted in a difficult social environment and rose above a negative political atmosphere to share his discoveries with the world.

To Matka and Steve

ACKNOWLEDGEMENTS

For the quarter of my life during which I developed the work in this thesis, many people have provided support and shared the joy and struggle of such an exploration, which has taken place on many levels – both scientific and personal. From the marathon stretches to the sprinting bursts, they have helped make the adventure an enjoyable learning experience and bring even more and deeper meaning to it.

First, I'd like to thank my advisor, Gus Evrard, for helping guide me toward the interesting questions and helping me to focus my energy, but also for begin flexible as I developed my own methods of investigation and explored multiple kinds of research. Thanks to Tim McKay for spending time underneath that Autumn tree and inspiring me toward a science about which I have become impassioned. Greg Tarlé has been very supportive in my broad interests; I appreciate his guidance through instrumentation work, his inspiringly consistent sense of awe for the abstract things that we do – and of course for the political debates and distractions. Thanks to Jeff for being an exceptional professor and sharing his youthful exuberance during our time together. Marta, with her hospitality, her chamomile tea, and her candor, have bolstered both my confidence and my comfort in pursuing a scientific career. Fred believed in me before I arrived at Michigan; his flexibility in allowing me to take some time to rejuvenate before starting school, and in presenting a great example of a scientist, are much appreciated. The members of my committee are not just great scientists, but great mentors and friends.

Thanks to Shanna banana for being a good little basement gnome and to her and

Jasper for sharing their couch with a stranger on the first day of school. Gracias a Ale por recordarme a la persona que yo soy y la persona que yo pueda ser. Thanks to Dharple for durpelling so well. Thanks to my office-mate and collaborator, Jiangang for helping me catch up on the ins, outs, beauty and ugliness of cluster-finding – and for keeping things simple when they appear complicated. I enjoyed a great deal our conversations about life, language, culture, and Chinese wine. Thanks to Brandon for believing in, and bringing out, my dark side; to Jake for commiserating in grunts and other noises while coding furiously; and to Anbo for the keeping the lights on and the office warm, and reminding me that there is basketball to played! Thanks to Carlos 'Cee-los' Cunha for the fun distractions and being supportive during the final stages.

I appreciate the time I was able to spend with all the cacklers and avatar 'imagineers' of the McKay lab – thanks for great conversations, for being great traveling buddies, and of course for cackling; Kimmy and I have had some great conversations about our work, and also about why we do it, especially in a world where there are so many people to experience and learn from outside the realm of science. Rachel has often helped bridge that divide to blur the line between our scientific minds and social realities. Those conversations have been a great source of grounding and inspiration.

The Kraushaus has been a great home: Nicolas has helped keep me nourished like it was his job; Le made me go to Fleetwood and challenged my dancing skills; Emmanuel, Ajay, and Jun have been great friends and roommates. Working and playing with the people of MISSION and Camp Take Notice has helped remind me why I love studying the physical world, and helped finding my; Thanks to Matt Becker for being the Hebrew hammer; to Ele for being such a great roommate and friend; to Bmac for being a brother in arms and the B1 to my B2; to Becky, Eli and Eduardo for their mentorship; to Ross for being so cynically funny and letting the wisdom leak out of his beard; to Mark for helping

remind me to do it my way (Thank you, good night!); to Matthew Isaac for being family; to the students I had the good fortune to mentor and from whom I also learned a great deal.

Also, thanks to the Michigan Space Grant Consortium and Dr. Alec Gallimore for his continued support over the years. Thanks to the student services office and technical support staff for making all the administrative issues easy to work through. A special thanks to Kimberly for being my mom away from home. Finally, thanks to the Rackham Merit Fellow Program for providing support and funding, which allowed me to focus on my research; also, thanks to the Michigan Space Grant Consortium, and in particular Alec Gallimore, for the many opportunities to share my work with the public and to advocate for science funding and education.

Finally, thanks to my Mom and Dad; I'm as proud of them as they are of me.

PREFACE

Cosmology and Cosmogony have long been the domain of traditional myths within distinct human subcultures. Mythical descriptions of the universe and the human role in it remain locally relevant to each human sub-culture: through their stories, they provide a keystone of shared meaning and ethics that can enrich social structure, and simultaneously buttress it in times of turmoil, helping preserve the human species existentially.

Though traditional subcultural myths share many fundamental building blocks, like those aforementioned, the vocabulary within the descriptions is distinct, which enriches the global human culture through diversity. This enrichment is driven by the growth that we undergo as we struggle to understand each other to live both within and beyond our diversity simultaneously; and the struggle is a large part of the current meaning that we bring to our shared life as a species.

However, within the last few centuries, and especially the last few decades, science has begun to drive a potentially trans-cultural understanding the universe: it need not supplant traditional cosmogonies in every aspect, but can reside alongside them. Physical cosmology is the culmination and latest iteration in modern science's effort to develop the largest-scale context for life and physical processes. It presents another kind of myth that is at once a product of the 'science' subculture, and a cosmogonic description that can potentially transcend the motivations and manifestations of traditional belief systems – with reverence, however, to the purposes that those systems serve. Physical cosmology tells a unique story and brings a unique meaning to our lives, and in that way, shares

something very deep with traditional myth. In a general sense they both speak to the presence and investigation of the unknown, but they share at least one commonality in their development: Claude Lévi-Strauss said that "the true constituent units of a myth are not the isolated relations but bundles of such relations." Through the exploration of these constituent bundles, we develop our stories, and the degree of their interconnectedness and self-consistency largely determines their perseverance.

Modern cosmology based in science may eventually provide a bridge among traditional myths across space and time. They presently co-exist in a healthy struggle, and they serve different needs of humankind. However, physical cosmology has also transformed the unknown into that which is known: science is a unique mythical endeavor, because it provides a story that is both universally relevant and governing; moreover, it evolves continuously and can be an agent to evolve our understanding of ourselves in the largest contexts. The stories of physical cosmology can reveal that which inspires awe, without treating it as unattainable.

TABLE OF CONTENTS

LIST OF FIGURES

Figure

LIST OF TABLES

Table

CHAPTER I

Introduction to Cosmology

Almost every human culture has developed a story of cosmic origins. These stories permeate religion, art and science, offering a linking strand between fields of study as well as cultures. They also offer a larger context in which to couch and share the human condition. Almost universally, cosmogonies position humankind as the conduit between the infinite and the finite, the unobserved event and the tale told. The human endeavor of science is no different: the potentially infinite physical universe provides clues from which its form and function can be uniquely reconstructed. From a finite number of puzzle pieces, an observer can begin to account for the kinds of energy in the universe, to measure the shape and age of the cosmos, and to predict with some fidelity its fate.

Dissertation Overview and Organization

In the remainder of the introduction, I provide an introduction to Big Bang Cosmology and the modern ΛCDM paradigm (§1.1). I first review the major epochs of cosmic evolution and the primary constituents of the universe. I then review the modern tests of isotropy and homogeneity, and how those tests lead to a set of cosmological parameters to be investigated. I guide the reader through the paradigm of the modern Big Bang ΛCDM of cosmology. First, the time-line covers the principal events of the Universe's birth, from the quark-gluon soup to the formation of large-scale structure, including the experiments

that have provided the modern accounting of the cosmic energy budget. I then discuss the underpinnings and formalism of physical cosmology, reviewing the building blocks of large-scale structure formation theory, and conclude with the role of clusters as probes of cosmic expansion. Along the way, I provide examples of the effects of dark energy on the observable features of the Universe.

If you are familiar with standard Big Bang Cosmology and the current state of affairs, but *not* the role of galaxy cluster abundance in the investigation of Dark Energy, then it is recommended that you skip to §1.4. If you are familiar with the basic arguments for how clusters can be used to discern between cosmologies, but not how cluster samples are gleaned from sky surveys or the physics of observable cluster signatures, then you may choose to start with Chapter II.

In Chapter II, I review the relationships among observable signals and mass in clusters of galaxies. Here, I develop the framework of the signal-mass correlation and argue for its pivotal role in constraining cosmologies, primarily through the halo mass function. This provides the reason for the construction and the backdrop for the analysis of my simulated cluster surveys.

Original research contributed by the author is covered in Chapter's III-V. In Chapter III, I and others performed a case study analysis of cluster scaling relations: we highlight the importance of observational biases in scaling relation analysis and the utility of multi-wavelength correlations; these discussions reflect work by the author contributed to published works, Stanek et al. (2006), Nord et al. (2008), and Rykoff et al. (2008).

Chapter IV reviews the construction of the Millennium Gas Simulation Virtual Sky Surveys (MGSVSS), the setting or arena in which we will later develop our methods for setting cosmological constraints via clusters. We perform diagnostic tests to ensure the survey's faithful representation of reality. In Chapter V, we show virtual observations and

analyses of clusters discovered in the virtual sky. We conclude with a summary and plans for future work in Chapter VI.

1.1 Time-line of Cosmic Events and the Current State of Affairs

The Universe was born into a state much hotter and denser than the current one. Space-time has since expanded and continues to expand, growing ever cooler and larger. The initial *big bang* may have bubbled up out of another universe (Linde, 1986), fallen out of a collapsed quantum-gravitational wave function (Wheeler, 1955; Hartle and Hawking, 1983), or resulted from high-dimensional brane collisions (Langlois, 2002); these concepts are just a few of the possibilities, and we have little experimental evidence to constrain the earliest moments of cosmic history. While the exact nature of the beginning is uncertain, new physics beyond that of the Standard Model of particle physics is expected: it potentially allowed the forces we see today (gravity, electro-magnetism, and the strong and weak forces) to be unified into a single force during the very first fractions of a second; as the cosmos cooled, gravity would likely have decoupled first, with the strong and weak interactions following soon after. The new physics at the earliest times may also be that which drives something like the theorized mechanism of *inflation*, which expanded space-time by orders of magnitude within fractions of a second, as depicted in Fig. 1.1 (far left). *Reheating* converted the inflaton (the particle that drives inflation) into a relativistic hot plasma of particles, starting the radiation-dominated era of the hot Big Bang. Particles, as well as their anti-matter counterparts, had survived up to this point, but then annihilated, removing all anti-matter from the Universe and leaving only a small fraction of the original matter. These processes of *Baryogenesis* and *leptogenesis* preserved the baryons and leptons, the fundamental building blocks of matter that have come to compose everything from galaxies to planets to bacteria. From baryons are built nucleons (*i.e.,* protons

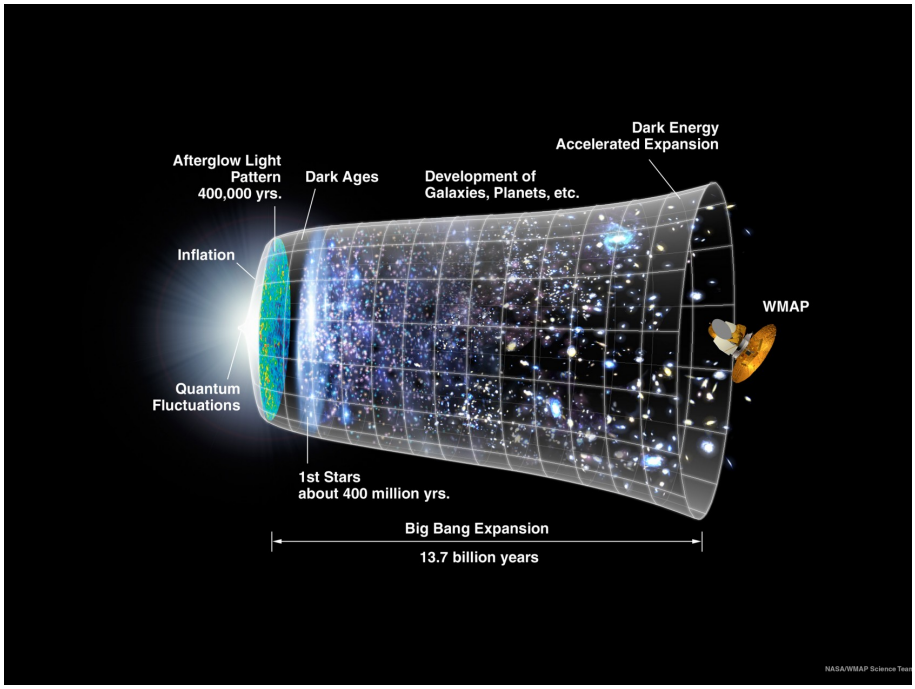

Figure 1.1: Pictorial representation of the cosmic time-line – from the theorized inception of "quantum fluctuations" to the epochs of large-scale structure formation and accelerated expansion. The Wilkinson Microwave Anisotropy Probe (WMAP) satellite (far right) has observed the afterglow of the *last scattering surface* (far left), the oldest part of the universe that can be seen today (NASA / WMAP Science Team, 2010a).

and neutrons), which subsequently formed out of the cooling quark-gluon plasma; they remained differentiated from the leptons (*i.e.,* electrons and neutrinos), however, while the high-energy photons remained in close proximity.

Relic abundances of nuclear species provide the evidence for the build-up of atomic elements (*e.g.,* , He, Li) from the nucleons. During *Nucleosynthesis* – one of the three pillars of the Big Bang Theory (Steigman et al., 1977) – less than 20 minutes were available for protons and neutrons to fuse into nuclei, and become confined with radiation into a baryon-lepton-photon fluid. As the expansion proceeded, the universe eventually cooled sufficiently to decouple matter particles and photons, allowing nuclei to capture electrons and form atoms. The "recombination" of baryons and leptons also marks the *last scattering surface*

(LSS) for photons, which were thenceforth free to stream throughout the now-transparent universe.

Measuring Isotropy and Homogeneity

The Cosmic Microwave Background (CMB) is the relic radiation from the LSS, which has been mapped by a series of experiments over the the last 20 years, the most recent of which being the Wilkinson Microwave Anisotropy Probe (WMAP) (Fixsen et al., 1994; Ruhl et al., 2003; Jarosik et al., 2010). Fig. 1.2 shows the WMAP seven-year all-sky

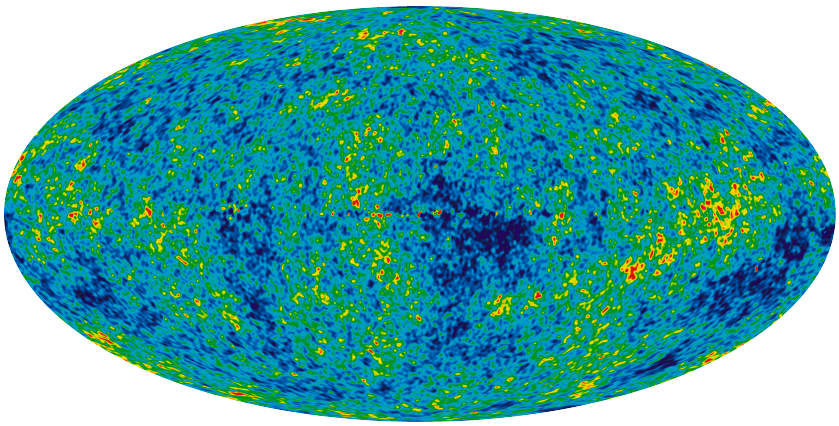

Figure 1.2: The Cosmic Microwave Background (CMB) observed by the WMAP satellite from the seven-year data release. The colors represent temperature fluctuations with respect to the mean temperature, $T_{\mathrm{CMB}} \approx 2.762\mathrm{K}$; reddest is warmest, and bluest is coolest. The fluctuations have a magnitude of about $10^{-5}K$ (NASA / WMAP Science Team, 2010b).

temperature map, where the mean temperature, dipole anisotropy, Milky way signal, and other astrophysical signals have been removed: the minute temperature variations, $\Delta T/T$, at just one part in 10^5, reveal rich information about the early universe.

The angular power spectrum of anisotropy, $\left\langle (\Delta T/T)^2 \right\rangle$, shown in Fig. 1.3, encode the density fluctuations of the baryon-electron-photon fluid during recombination. This class of *primary* anisotropy arises from physical processes that occur prior to and during

recombination. In particular, these features can be calculated with (a) an initial, set of perturbations from inflation, and (b) simple linear acoustics physics in the electron-baryon-photon fluid. these are drawn from instabilities in the fluid which set up a pressure wave that corresponds to the fluid's sound speed. The scale of this *Baryon Acoustic Oscillation* (BAO) in our universe is given by the first peak in the anisotropy spectrum. The physical scale of these features are calculable; measurement of this spectrum can be used to constrain the angular diameter distance comparable to the physical scale and the diameter shows the universe to be flat. The universe, on the other hand, could have turned out to be spatially "closed": this means that light leaving an observer would eventually return to the observer, as if traveling on the geodesic of a sphere. Alternatively, the universe could have been spatially "open", light paths would diverge relatively rapidly, and the space-time would expand ad infinitum. In a matter-dominated universe with no other energies, matter alone would determine this degree of curvature and the fate of the Universe: for example, with sufficient matter to close the space, the Universe would also eventually collapse under gravitational attraction (the *big crunch*). However, the CMB results show that the universe lies very near the *critical* density, such that it will expand eternally ever faster.

Secondary anisotropies are modifications of the angular power accumulated during the life of the universe following recombination. For example, the Sunyaev-Zel'dovich effect produces power on arc-minute scales: condensed, hot plasma in the intracluster medium is warm enough to scatter CMB photons from their otherwise unperturbed paths and energies (Sunyaev and Zeldovich, 1972).

The minute CMB *primary* anisotropies shown in Fig. 1.2 are tell-tale signs of inhomogeneities seeded in the early universe before the last scattering of primordial photons. At recombination, photons and matter were released to separately evolve. During the *Dark Ages*, the Dark Matter and baryons co-evolved, and density fluctuations grew through

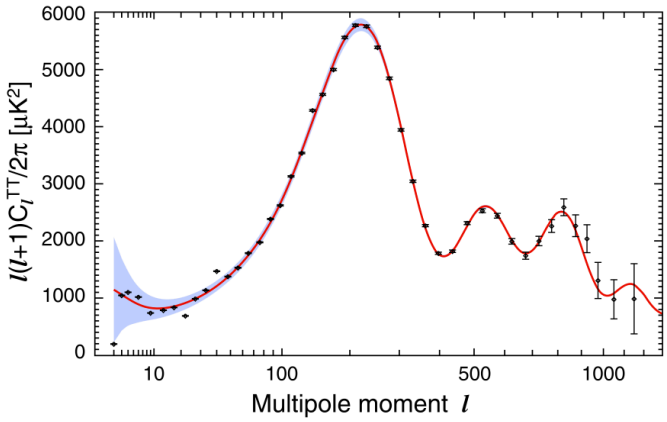

Figure 1.3: The binned seven-year WMAP power spectrum of the CMB on angular scales, $\ell = 2 - 1000$. The points are plotted with noise errors only. The red curve is the best-fit ΛCDM model, which is fit to WMAP data only (Spergel et al. 2006), and the band is the binned 1σ cosmic variance error (Larson et al., 2010).

gravitational instability: dark matter drove the formation of gravitational potential wells, into which baryons flowed and condensed to produce the first stars. In the following *Epoch of Reionization* (EoR), stars produced radiation that disintegrated the neutral pre-galactic medium (PGM). The gas, plasma, dust and stars then began to coalesce into the galaxies that, today, still trace the initial pattern of matter density fluctuations set at recombination.

Following the EoR, large-scale structure matured into a state revealed by modern galaxy surveys, such as the Sloan Digital Sky Survey (SDSS; York et al., 2000), the Two-degree-field Galaxy Redshift Survey (2dFGRS; Folkes et al., 1999), and Center for Astrophysics redshift surveys (CfA2; Ramella et al., 1992). The structure of these surveys is depicted in Fig. 1.4 and appears as a collection of nodes connected by filamentary streams of matter, with mostly empty regions in between. The apparent filamentary structure is a consequence of the collapse of matter density perturbations through gravitational instability in an expanding background. Hierarchical theories of structure formation have provided the

most faithful reconstructions of the cosmic web. Increasingly sophisticated N-body simulations have only added support for this view of structure formation (Bond and Myers, 1996; Bond et al., 1996).

The cosmic web can be quantified through the clustering of galaxies, which can provide information about both the mean matter density and the average size of spatial variations (aka, *perturbations* or *fluctuations*) in the matter density. On large distance scales (*e.g.,* 50 Mpc), where the evolution of density variations is relatively simple, we use the n-point correlation of galaxy positions and its frequency-space counterpart, the power spectrum of density fluctuations. These provide an adequate description of the total cosmic matter content on these scales. The former "Standard" Cold Dark Matter model (SCDM; White et al., 1987) held that the matter density is equal to the critical density with negligible curvature. However, galaxy clustering observations over the last 20 years constrain the cosmic matter density to be less than one-third the critical density of the universe (Maddox et al., 1990; Tegmark et al., 2006). When density perturbations have become sufficiently massive relative to the expanding background, they collapse and break away from the cosmic expansion. At this point their evolution is no longer linear, and they become self-bound structures, known as halos. These halos contain a hierarchy of astrophysical objects, depending on epoch and scale: the smallest halos (subhalos) are thought to contain a single galaxy, while the most massive halos host clusters of galaxies. This tends to happen near a scale of ~ 8 Mpc today. The abundance of clusters at each epoch is highly sensitive to the variance in the perturbation spectrum on that scale and has been used in tandem with the galaxy clustering on larger scales to constrain both that parameter and the matter density (*e.g.,* Bahcall et al., 1997). In fact, constraints on the universal baryon content from relic abundances and cluster formation processes make starkly clear the necessity for a sub-critical matter density (White et al., 1993b). More recent measurements of the X-ray

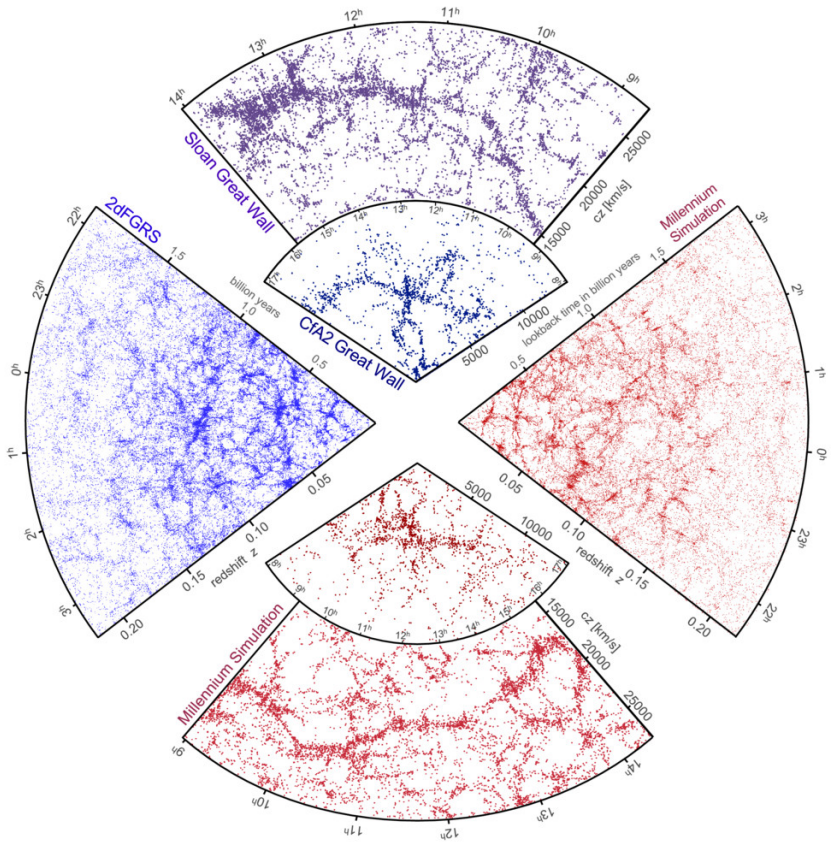

Figure 1.4: Density map of galaxy populations in the 2dFGRS, SDSS, CfA2 Survey (left and top wedges) and the Millennium Simulation (right and bottom wedges). The same cosmic web pattern exists in all four depictions. Redshift space distortions, known as "Fingers of God," betray coherent line-of-sight infall of galaxies into nearby massive superstructures; these are very clear to the eye in the Sloan Great Wall (Springel et al., 2006).

gas mass fraction in clusters further this argument by formally placing constraints on the matter density (Allen et al., 2002, 2004).

Measuring Cosmic Distances and the Speed of Cosmic Evolution

The cosmic distance ladder is comprised of a series of standard candles – objects whose intrinsic luminosity, and thus their distances, can be measured. An important rung on the cosmic distance ladder was set in place by Edwin Hubble who first observed the expansion of universe by determining distances to galaxies through their spectra. He found that, as

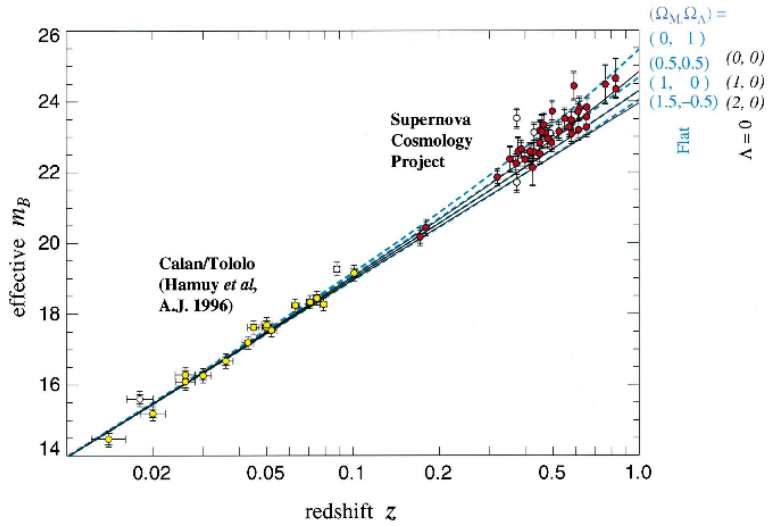

Figure 1.5: The magnitude-redshift distribution of supernovae in the local universe (points) from the Supernova Cosmology Project (SCP). Models for a variety of cosmologies are also displayed. The best agreement between data and theory occurs for cosmologies with a Cosmological Constant and flat geometry (Perlmutter et al., 1999b).

galaxies move away from a typical observer with the cosmic expansion, it appears that their recessional velocities are proportional to their distance:

$$\mathbf{v} = H\mathbf{r}, \tag{1.1}$$

where the Hubble constant is the proportionality factor, $\mathbf{v}$ is the relative velocity, and $\mathbf{r}$ is the physical distance: in an expanding universe and in the absence of peculiar (local) velocities of the galaxies, the physical distance should increase with the expansion rate. If some objects are further away than others, they must have been closer at some earlier epoch; generalizing, there must have been an *earliest epoch*. The earliest point in the universe, it's origin, is known as the Big Bang and Hubble's discovery of receding galaxies is the another pillar of the Big Bang Theory.

Since then, many have continued to look farther away and deeper into the past, establishing a cosmic distance ladder with standardized candles. Supernovae are the latest and the most distant of the rungs on the ladder. Fig. 1.5 shows the supernovae brightness as a

function of redshift, as well as theoretical predictions of the same function for matter-only, dark energy-only, and mixed-species cosmologies – all with the zero-curvature assumption. The supernovae are dimmer (or equivalently lie further away) than expected in the SCDM model – *i.e.,* further away than if matter currently dominated the energy budget (Perlmutter et al., 1999b; Riess et al., 1999). The supernovae are thought to have been accelerated away by a space-time that is expanding ever faster. The mechanism for this accelerated expansion, coined "dark energy" (Perlmutter et al., 1999a), however, has not been identified. It is indeed possible that vacuum energy (*i.e.,* Einstein's Cosmological Constant) can cause the expansion. Vacuum energy would provide negative pressure to space-time, forcing it to expand at an increasing rate. However, predictions from particle field theory suggest that a constant vacuum energy would be 120 orders of magnitude greater than what is measured or predicted in a cosmological context – a discrepancy known as the Cosmological Constant Problem. A variety of theories for the nature of Dark Energy abound, with few constraints to guide their development: no Standard Model particle, nor next-generation particle, has yet provided a suitable candidate. The model of *quintessence* takes dark energy to be an isotropic, ubiquitous scalar field but with a strength which evolves with time. Discerning whether the universe's dark energy comes in the form of a time-varying quintessence or a static Cosmological Constant is the first question that most cosmological experiments will seek to constrain in the next decade.

Assembling the pieces of evidence for our current model of the cosmos, we find that the curvature is negligible, but the total matter density is merely one-third of that needed to balance the universe; also, there is strong direct evidence for an accelerating expansion, which likely requires another form of energy. We then consider the possibility that the remainder – in fact, the majority – of the energy budget, that which balances the lack of curvature, is a new field or particle species with an unknown origin. Fig. 1.6 shows

constraints on the matter and vacuum densities from independent experiments: through mostly independent means, several experiments have implied the existence of dark energy.

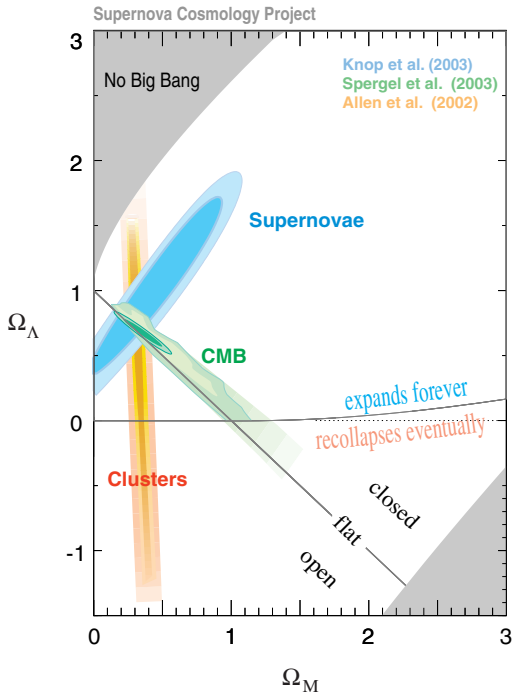

Figure 1.6: Independent constraints on the vacuum energy and matter densities at the current epoch from a suite of complementary physical probes – the CMB (from WMAP), supernovae (from SCP), and clusters of galaxies (via the cosmic gas fraction derived from X-ray-selected clusters). The three methods overlap to show that the current epoch of the universe is Dark Energy-dominated and lacks curvature (Perlmutter, 2003).

The future of the universe is yet to be determined, at least until the nature of the Dark Energy is discovered: is it a constant vacuum energy density, or does it evolve with time? Vacuum models of dark energy suggest that before the end (if it ever comes), local volumes of the cosmos will become isolated: as distances grow larger and at an ever-increasing rate, light will move too slowly to make it from one part of the universe to another. N-body simulations running into the far future of a ΛCDM universe depict the lonely, relaxed end state of halos and clusters (Busha et al., 2003).

Rather than conjure a new energy field to cause acceleration, it may be possible to modify Einstein's theory of gravity (known as General Relativity or "GR," and described in §1.2), such that an acceleration becomes unnecessary. Typical models of these theories invoke higher dimensions (*e.g.,* Dvali et al., 2000), modifications of the Einstein-Hilbert action (*e.g.,* Dunsby et al., 2010), or hybrid tensor-scalar fields (*e.g.,* Bergmann, 1968; Bekenstein, 2004). Hu (2009) outlines the general issues that plague cosmological tests of GR. Interestingly, primary among them is "Dark Energy equivalence"; in brief, without a pre-conception of the complete zoology of energy fields at the beginning of the universe, modified gravity models can be trivially re-scaled to appear identical to GR.

The era of precision cosmology has begun, as evidenced by Table 1.7, which displays the most recent compendium of constraints on cosmological parameters. Many of them are known to percent-level precision when multiple and complementary data sets are used.

Class	Parameter	*WMAP* 7-year ML[b]	*WMAP*+BAO+H_0 ML	*WMAP* 7-year Mean[c]	*WMAP*+BAO+H_0 Mean
Primary	$100\Omega_b h^2$	2.227	2.253	$2.249^{+0.056}_{-0.057}$	2.255 ± 0.054
	$\Omega_c h^2$	0.1116	0.1122	0.1120 ± 0.0056	0.1126 ± 0.0036
	Ω_Λ	0.729	0.728	$0.727^{+0.030}_{-0.029}$	0.725 ± 0.016
	n_s	0.966	0.967	0.967 ± 0.014	0.968 ± 0.012
	τ	0.085	0.085	0.088 ± 0.015	0.088 ± 0.014
	$\Delta^2_{\mathcal{R}}(k_0)$[d]	2.42×10^{-9}	2.42×10^{-9}	$(2.43 \pm 0.11) \times 10^{-9}$	$(2.430 \pm 0.091) \times 10^{-9}$
Derived	σ_8	0.809	0.810	$0.811^{+0.030}_{-0.031}$	0.816 ± 0.024
	H_0	70.3 km/s/Mpc	70.4 km/s/Mpc	70.4 ± 2.5 km/s/Mpc	70.2 ± 1.4 km/s/Mpc
	Ω_b	0.0451	0.0455	0.0455 ± 0.0028	0.0458 ± 0.0016
	Ω_c	0.226	0.226	0.228 ± 0.027	0.229 ± 0.015
	$\Omega_m h^2$	0.1338	0.1347	$0.1345^{+0.0056}_{-0.0055}$	0.1352 ± 0.0036
	$z_{\rm reion}$[e]	10.4	10.3	10.6 ± 1.2	10.6 ± 1.2
	t_0[f]	13.79 Gyr	13.76 Gyr	13.77 ± 0.13 Gyr	13.76 ± 0.11 Gyr

Figure 1.7: Cosmological parameters derived from the WMAP's seven-year data release; some are derived from multiple data sets. (adapted from Table 1 of Komatsu et al., 2010).

1.2 Foundations of Modern Cosmology

In the next three sections, I review the underpinnings of cosmological physics, establish the theory of large-scale structure formation, and discuss the utility of galaxy clusters as probes of the cosmic expansion history. In his *Principia*, Sir Isaac Newton documents

an observed equivalence between inertial mass, $m_{\rm i}$, and gravitational mass, $m_{\rm g}$ (Newton, 1760): that which incurs a weight also dictates motion. The extension of this correspondence to a geometric context occurs in Einstein's conception of the Equivalence Principle,

$$m_g \quad \leftrightarrow \quad m_i \tag{1.2}$$

$$\Phi_g \quad \leftrightarrow \quad g_{\mu\nu} \tag{1.3}$$

where the gravitational potential, $\Phi_{\rm g}$, corresponds to the deformation of, or curvature in, the space-time manifold; that curvature is encapsulated by the metric, $g_{\mu\nu}$. Local deformations dictate the trajectories of particles, rather than a force acting at a distance; and the universal energy content influences the dynamics of space-time as a whole. Einstein's set of coupled differential field equations

$$R_{\mu\nu} - \frac{1}{2}Rg_{\mu\nu} + \Lambda g_{\mu\nu} = 8\pi G T_{\mu\nu}, \tag{1.4}$$

encompass this interaction completely: the stress-energy tensor $T_{\mu\nu}$ (energy and matter) on the right induces curvature via the metric, $g_{\mu\nu}$, and via the Ricci scalar and tensor, R and $R_{\mu\nu}$, respectively; and the curvature dictates the trajectory of the matter and energy (*i.e.,* particles). Λ, known as the Cosmological Constant, represents the constant vacuum energy of space-time, a candidate for the Dark Energy; it acts counter to the attractive force of gravity and causes space-time to accelerate in its expansion.

For the assumptions of large-scale isotropy and homogeneity (the *Cosmological* or *Copernican Principle*), the three-dimensional volumes of space-time must be maximally symmetric, and thus invariant under translation and rotation. For this kind of space-time continuum, Robertson and Walker developed the unique space-time (r-t) metric

$$\mathrm{d}s^2 = c^2\mathrm{d}t^2 - a(t)^2\left[\frac{\mathrm{d}r^2}{1-\kappa r^2} + \chi_\kappa(r)\mathrm{d}\Omega^2\right], \tag{1.5}$$

where c is the speed of light, $\mathrm{d}\Omega^2 = \mathrm{d}\theta^2\sin^2\theta\mathrm{d}\phi^2$ the solid angle, and $\kappa = \{-1, 0, 1\}$ the degree of curvature of the space-time. The scale factor, $a(t)$, traces the expansion history

of the space-time as a whole, and the co-moving distance, χ, is the position of a typical observer embedded in that expansion. From this point on, we use natural units so that $c = 1$.

Cosmic expansion not only increases the distance between particles, but lengthens the wavelengths of photons. The fractional change in wavelength (*i.e.,* the redshift, z) is related to the scale factor by $a = 1/(1+z)$. The redshift denotes the reddening of photons whose wavelengths are stretched by cosmological expansion. As can be seen from this inverse proportionality, $z \to \infty$ and $a \to 0$ in the early universe, while $z \to 0$ and $a \to 1$ today.

The unperturbed Einstein Field Equations, when constrained by the Cosmological Principle, can be re-written as the two Friedmann equations. The first is garnered from the trace of the tensor equation, and it relates the acceleration of the expansion, $\ddot{a}$, to the energy densities, $\rho_{\rm i}$, of the fluid species:

$$\frac{\ddot{a}}{a} = -\frac{4\pi G}{3}(\rho + 3p) + \frac{\Lambda}{3}, \tag{1.6}$$

where p is the pressure. The second arises from the 00 tensor component and relates the expansion rate to the constituents:

$$H^2 \equiv \left(\frac{\dot{a}}{a}\right)^2 = \frac{8\pi G}{3}\rho - \frac{\kappa}{a^2} + \frac{\Lambda}{3}, \tag{1.7}$$

where H is the *Hubble* rate of Eqn. 1.1. The critical density

$$\rho_c \equiv \frac{3H^2}{8\pi G}, \tag{1.8}$$

marks a balance between energy and space-time curvature, such that $\Omega \equiv \sum_i \rho_i/\rho_{\rm c} = 1 + \left(\kappa/H^2a^2\right)$. In a flat universe, for example, $\kappa = 0$, $\Omega = 1$, and parallel light rays remain parallel; in an open universe, however, $\kappa < 0$, $\Omega < 1$, light rays that start parallel will diverge, and the universe will expand forever.

To complete the set of equations governing the interaction between the fluid and the space-time manifold, we apply conservation of energy, via a covariant derivative of the stress-energy tensor, $T_{\mu\nu}$, to obtain an equation of motion for the density,

$$\dot{\rho} = -3\frac{\dot{a}}{a}\left(\rho + p\right), \tag{1.9}$$

where we introduce the *equation of state*,

$$p = w\rho, \tag{1.10}$$

with equation-of-state parameter, w. For a particular species, we can substitute for the pressure (Eqn. 1.10), and solve for both the power-law dependence of the density on the scale factor, and the scale factor's time-evolution:

(1.11)

$$\rho_i(a) \propto \begin{cases} a^{-3} \\ a^{-4} \\ e^{-2t/3} \\ e^{-\int \frac{\mathrm{d}a}{a}[1+w(a)]} \end{cases} \quad \Longrightarrow \quad a(t) \propto \begin{cases} t^{2/3} & (\text{matter}, m) \\ t^{1/2} & (\text{radiation}, r) \\ e^{2/3t} & (\text{vacuum}, \Lambda) \\ & (w \neq \text{ constant}) \end{cases},$$

Each particular scaling is appropriate during the cosmic era in which the corresponding species dominates. Radiation dominates before recombination ($z_{\mathrm{rec}} = 3100$), at which time, matter becomes the primary influence on expansion. In the very recent past, dark energy has come to dominate. They can be woven together continuously, as shown in Fig. 1.8, which displays the expansion history of the universe for a suite of cosmological parameters and highlights the divide between an ever-expanding or an eventually collapsing universe. Dark energy as a cosmological constant may have a range of equations-of-state: $w < -\frac{1}{3}$ provides the negative pressure since the energy density must be positive; as w decreases, the power of the Dark Energy to drive acceleration increases. The set of cosmic energy

densities can be written with respect to the critical density of Eqn. 1.8:

$$\Omega_{\rm m} \equiv \frac{\rho_{\rm m}}{\rho_c}, \quad \Omega_{\rm r} \equiv \frac{\rho_{\rm r}}{\rho_c}, \quad \Omega_\kappa \equiv \frac{-\kappa}{a_0^2 H_0^2}, \quad \Omega_\Lambda \equiv \frac{\Lambda}{8\pi G}, \tag{1.12}$$

where Ω_κ is not really an energy density, but for the purposes of a unified formulation, that term in Eqn. 1.7 can be normalized to mimic one. Normalizing the Hubble constant to the current epoch shows how all the fluid species relate to the expansion rate:

$$E(a)^2 \equiv \frac{H^2(a)}{H_0^2} = \Omega_{\rm r} a^{-4} + \Omega_{\rm m} a^{-3} + \Omega_\kappa a^{-2} + \Omega_{\rm X} e^{-3\int {\rm dln}a[1+w(a)]}, \tag{1.13}$$

such that $w \rightarrow$ constant and $X \rightarrow \Lambda$ for the case of a constant vacuum state; X represents dark energy in general, when the exact mechanism is not specified.

In an expanding world model, distance measures must be modified to accommodate changes in the light travel time and the physical change of the light itself. The *co-moving* distance is that distance which remains constant for objects moving with the Hubble expansion. It can be written as a function of the cosmic time, the scale factor, or the redshift:

$$\chi = \int_0^t \frac{{\rm d}t'}{a(t')} = \int_0^a \frac{{\rm d}a'}{a'^2 H(a')} = \int_0^z \frac{{\rm d}z'}{H(z')}. \tag{1.14}$$

As light travels from a distant object to an observer, it undergoes modifications due to the background expansion. First, consider the intrinsic luminosity, L, emitted by an object, which is related to the flux, F (energy per unit time, per unit area), measured by some detector as

$$F = \frac{L}{A}, \tag{1.15}$$

with surface area, $A = 4\pi d_{\rm L}^2$, where $d_{\rm L}$ is the *luminosity distance*. The flux is diluted by two phenomena. The expansion of the space-time causes a stretching of the photon's wavelength, and so its energy is redshifted by a factor, $(1 + z) = 1/a$. Also, concentric shells of space-time are further apart in the present than they were when the photons were

emitted: if space has expanded by a factor of a in the time between the emission of two photons, the flux will be reduced by that same factor. If the co-moving distance and surface area maintain a constant flux for observers, then the physical surface area and luminosity distance reflect the physical changes in the photons:

$$F = \frac{L}{4\pi d_L^2 a^2} \qquad \Rightarrow \qquad d_L = \frac{\chi}{a}. \tag{1.16}$$

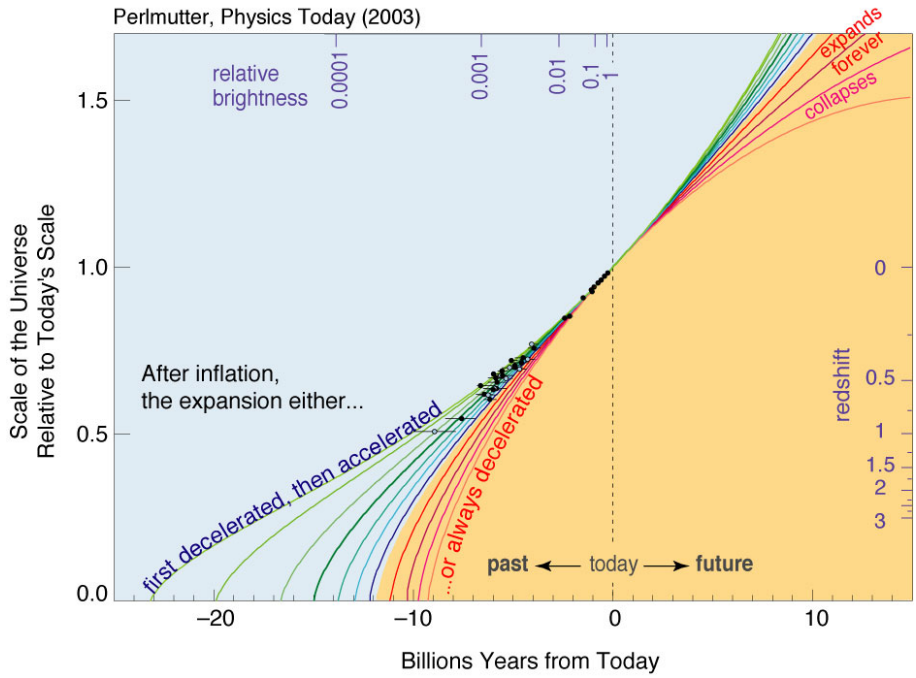

Figure 1.8: The expansion history of the universe for a variety of cosmological parameters. The left and right axes register the rate of expansion via the scale factor and redshift, respectively. The upper and lower show the time relative to today and the relative supernova brightness, respectively. The supernovae data are in agreement with the expansion curves that predict an eternal, accelerating expansion (Perlmutter, 2003).

Assuming Euclidean geometry, the co-moving size, $\chi\theta$, of a distant object remains constant with expansion, where θ is the angular size. It's proper size however, is affected by the expansion, such that

$$s = \chi\, a\, \theta, \tag{1.17}$$

$$d_{\rm A} \equiv \chi a \tag{1.18}$$

where $d_{\rm A}$ is the radial *angular diameter distance* between the object and the observer.

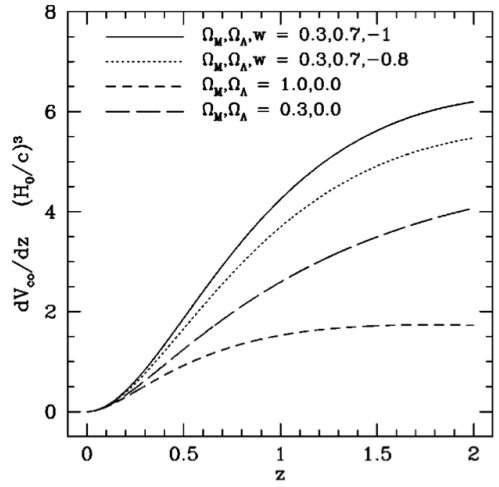

Figure 1.9: The co-moving differential volume, $\mathrm{d}V/\mathrm{d}z$, of a homogeneous expanding world model given four sets of values for the matter density, vacuum energy density, and equation-of-state parameter (Voit, 2005b).

There are a series of consequences for space-time dynamics in a dark energy-dominated world model. First, consider the age of the universe as measured via the Hubble constant: adding a constant vacuum term gives a Hubble time that is considerably smaller than the SCDM ($\Omega_{\rm m} = 1$) prediction. The repulsive force of a vacuum energy counteracts the gravitational attraction, and the universe effectively takes less time to expand to the same scale. Distances are affected, as seen in the supernovae samples that demonstrated the existence of dark energy (§1.1). Similarly, the expansion rate of co-moving *volumes* is affected: in Fig. 1.9, the differential co-moving volume, $\mathrm{d}V(z)/\mathrm{d}z$, is shown to evolve as a function of redshift. For SCDM (geometrically closed) universes, the greater the matter density, the stronger the gravitational deceleration, and thus the smaller the universe at a given epoch (the two lower curves). The upper pair of curves represent choices of ΛCDM cosmology with different equation-of-state parameters: the topmost curve shows the result for the canonical $w = -1$ setting, which provides a stronger effective pressure; this incurs a faster expansion rate than the lower of the pair.

1.3 Formation of Structure

With the decoupling of the photon-baryon fluid, the seeds of clusters and galaxies began to grow through gravitational instability, unfettered by pressure effects. This growth is *linear* until a density perturbation or fluctuation becomes unstable – *i.e.,* until it becomes much denser than the background. At this point, the growth of the fluctuations becomes *non-linear*: the set of differential equations still govern the evolution of the density perturbations, but they are no longer analytically soluble. We first discuss linear growth, and then the results of peak-background splitting – halos.

1.3.1 Linear Growth

An inhomogeneity, δ, is a local deviation from the mean density, ρ_0, such that

$$\delta(\mathbf{r}) \equiv \frac{\rho(\mathbf{r}) - \rho_0}{\rho_0}, \tag{1.19}$$

where $\rho(\mathbf{r})$ is the density of a given fluid species at a point $\mathbf{r}$, with Fourier components, $\delta_{\rm k} = \int \mathrm{d}^3\mathbf{r}\delta(\mathbf{r})e^{-i\mathbf{k}\cdot\mathbf{r}}$. To broadly characterize the distribution of inhomogeneities, there exists the matter two-point correlation function, ξ, and its counterpart the power spectrum, $P(k)$:

$$\xi(\mathbf{r}) = \langle\delta(\mathbf{r}_0\,)\delta(\mathbf{r}_0 + \mathbf{r})\rangle \qquad \Longleftrightarrow \qquad P(k) = \langle\delta(\mathbf{k})^\dagger\delta(\mathbf{k})\rangle; \tag{1.20}$$

these quantities are used in the context of the galaxies to trace the full matter distribution, as discussed in §1.1. Owing to gravitational instability, high-density regions accumulate matter at the cost of lower-density regions. This accumulation results in a linear growth of the density perturbation. Combining the Euler equations for hydrodynamical fluid flow with a Newtonian gravitational source in an expanding background, we can derive a second-order differential equation of the evolution of linear perturbations for a given fluid

species:

$$\ddot{\delta} + 2H\dot{\delta} = 4\pi G\rho\delta. \tag{1.21}$$

Linear perturbation theory leads to solutions of this equation that take both decaying and growing modes, the latter of which defines the linear growth factor,

$$D(a) \equiv \frac{\delta(a)}{\delta(a=0)} = \frac{5\Omega_{\rm m}}{2}\frac{H(a)}{H_0}\int_0^a \frac{{\rm d}a'}{[a'H(a')H_0]^3}, \tag{1.22}$$

which is an essential factor in connecting the primordial density spectra to that of today.

Gaussian fluctuations of unknown origin (but, perhaps from inflation or a similar but unknown process) are thought to provide the universe's *primordial* (ostensibly) scale-free (Harrison, 1970) power spectrum, $P_{\rm p}(k)$. In order to obtain the power spectrum observed today, the primordial spectrum of perturbations must be evolved through cosmic history. During recombination, the scaling of power in various modes depends on the interaction between baryons and dark matter, as well as the dwindling influence of radiation (Bardeen et al., 1986). After recombination, the matter power spectrum no longer depends on the photons and grows linearly. The *Transfer Function* encodes both of these elements generally as the ratio of amplitudes between two epochs scaled by the linear growth factor – *e.g.,* the current epoch in ratio with some time in the early universe of scale $a_{\rm early}$:

$$T(k) = \frac{\delta(k, a=1)}{\delta(k, a_{\rm early})}\frac{1}{D(a_{\rm early})}, \tag{1.23}$$

The exact evolution during the period of recombination requires solutions to the Boltzmann equation of particle annihilation for the reaction, $e^- + p \leftrightarrow H + \gamma$, of electrons, protons, Hydrogen and photons, respectively. The equations are analytically soluble until the point of decoupling, at which numerical integration is required (Seljak and Zaldarriaga, 1996). Analytic approximations and fit functions have been developed and parametrized in terms

of the matter density:

$$T(k) = \frac{\ln(1+2.34q)}{2.34q}\left[1+3.89q+(16.9q)^2+(5.46q)^3+(6.71q)^4\right]^{-1/4}, \tag{1.24}$$

where $q = k(\Gamma h)^{-1}$ and $\Gamma = \Omega_{\rm m} h$ for mode k (for pure cold Dark Matter only; Bardeen et al., 1986). More recent enhancements of the approximation include effects from baryons and massive neutrinos (Eisenstein and Hu, 1998). The power spectrum today $P(k)$, therefore, is connected to the primordial power spectrum through the transfer function, $T(k)$:

$$P(k,a) \propto P_p(k, a_{\rm early}) T^2(k), \tag{1.25}$$

for modes, k, that are still undergoing linear growth.

1.3.2 Non-linear Growth

To begin a study of non-linear structures, we calculate the distance and mass scales at which density perturbations become non-linear. They are based on the variance of fluctuations in the density field within spheres of co-moving radius r. To set this scale, we invoke a spherical top-hat window function, which integrates to one over all space, but drops to zero quickly outside the scale of interest; in Fourier space, it is

$$W_r(k) = 3\frac{\sin(kr) - kr\cos(kr)}{(kr)^3}. \tag{1.26}$$

The resulting amplitude of fluctuations on the scale r in the matter power spectrum is given by

$$\sigma_r^2 = \int {\rm d}k \frac{k^3}{2\pi^2} P(k) \left|W_r(k)\right|^2. \tag{1.27}$$

and in the linear (pre-collapse) regime, the *rms* fluctuations evolve at the rate of the linear growth factor

$$\sigma_r(a) = D(a)\sigma_r(a=0). \tag{1.28}$$

Note that the level of fluctuations on the characteristic scale of $8\,h^{-1}\,\mathrm{Mpc}$ ($\sigma_8 \sim 0.8$) are larger today than at earlier times. When an object collapses, structure growth reaches the *non-linear* regime ($\delta \leq 1$), the Eulerian equations of motion are no longer analytically soluble, and $D(a)$ no longer gives the proper evolution. Numerical N-body simulations, however, permit the tracking of overdensities well into the non-linear regime.

Across many scales, simulations display the acute sensitivity of structure evolution to the presence of vacuum energy. In Fig. 1.10, we show the projected mass distributions in a slice of a simulation box at its full scale (upper panel) and at an enlarged view of the region around a particular node in the web (lower panel). We show three different sets of cosmological parameters. Several observations can be made, but I will focus on the apparent effects of the relevant energy densities. In the panels from left to right, the ratio of dark energy density to matter density decreases; accordingly, the contrast in the log-density decreases. Once the density field has begun to collapse into a cosmic web, dark energy serves to enhance the contrast by aiding in the segregation of large structures from one another. But, this is critically dependent on the epoch of transition from matter domination to dark energy domination: if dark energy were to have set in earlier, then the initial structure formation itself would be inhibited, producing less structure overall; this is corroborated by the predictions for the distributions of massive halos in an expanding background, as will be discussed below (*i.e.,* Fig. 1.11).

1.4 Halos and Clusters

We proceed by focusing on the non-linear objects after they have decoupled from the background to become dark matter halos and clusters of galaxies. We wish to measure the abundance of these halos as a function of mass and redshift, setting them up as tracers of the cosmological expansion rate, or buoys in space-time. The first analytic model of the

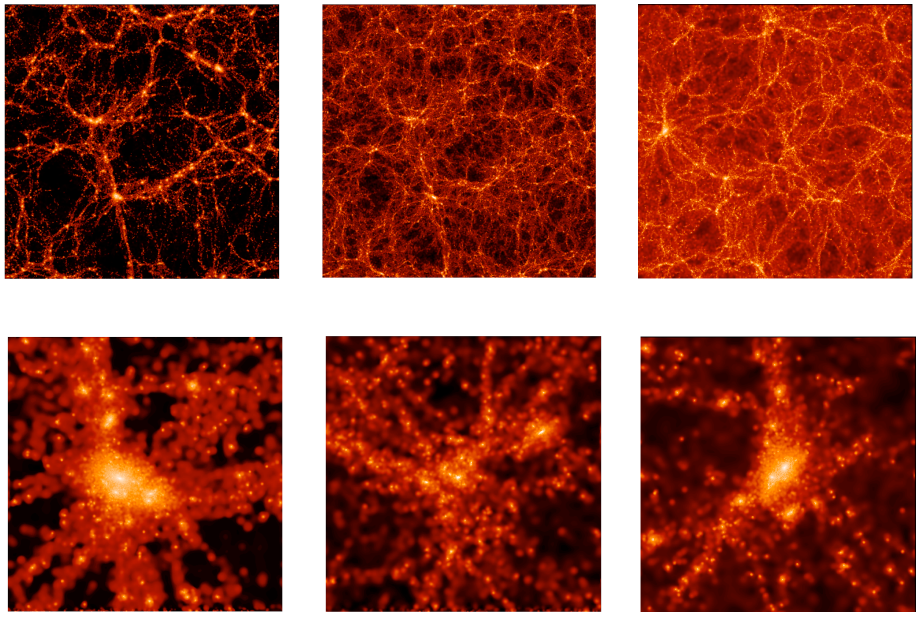

Figure 1.10: Projected mass distributions in a slice through a cold Dark Matter N-body simulation. The intensity is proportional to the log-density. From left to right, universes with the three following sets of parameters are shown. ΛCDM ($\Theta_\Lambda = \{\Omega_\mathrm{m} = 0.3, \Omega_\Lambda = 0.7, h = 0.7, \sigma_8 = 0.9, \Gamma = 0.21\}$) represents a critically balanced, accelerating universe; Open CDM ($\Theta_\mathrm{O} = \{0.3, 0.0, 0.7, 0.85\}$), represents a spatially open universe with runaway expansion; and Standard CDM ($\Theta_\mathrm{S} = \{1.0, 0.0, 0.5, 0.51, 0.5\}$) gives a spatially closed universe, bound to eventually collapse. The lower panel is an enlarged view of a large node/halo in the filamentary structure. The panels were accumulated from images of simulations by the Virgo Collaboration (Jenkins et al., 1998; Thomas et al., 1998).

halo abundance (mass function) was developed with the help of N-body simulations in a precursor effort to the more general Excursion Set formalism (Press and Schechter, 1974; Zentner, 2007). In successive iterations, similar forms were calibrated with increasingly sophisticated N-body simulations (Sheth and Tormen, 1999; Jenkins et al., 2001; Warren et al., 2006; Tinker et al., 2008). In the course of this dissertation, I use two different mass functions: they are formulated as distributions in the *rms* variation of density at a given mass scale and epoch, $\sigma(M, z)$, and normalized by mass and the mean mass density of the

epoch, $\bar{\rho}_{\rm m}$, as in

$$f(\sigma, z; \Theta) = \frac{m}{\bar{\rho}_m(z)} \frac{{\rm d}n(m, z; \Theta)}{{\rm dln}\sigma^{-1}(m, z)} \quad \longrightarrow \quad A \exp\left(- \left| \ \ln\sigma^{-1} + B \ \right|^{\epsilon}\right); \tag{1.29}$$

Θ represents a set of cosmological parameters, and the right-hand expression is the fitting form used in Chapter II (Jenkins et al., 2001). The fit parameters A, B, ϵ are dependent on cosmology. In Chapter IV, we use

$$f(\sigma, z; \Theta) \quad \longrightarrow \quad A \exp\left[\left(\frac{\sigma}{b}\right)^{-a} + 1\right] e^{c/\sigma^2}, \tag{1.30}$$

where the fit parameters A, a, b, and c are functions of redshift, and b is also a function of the halo size (Tinker et al., 2008). Most calibrations do not include the effects of baryons, but this is likely to be the next step in precision and universality of the mass function, once cluster-scale hydrodynamics can be correctly modeled (Stanek et al., 2009).

We can observe the effects of varying the Dark Energy equation of state on the halo mass function, as shown in Fig. 1.11. First, according to Percival (2005), the increase in amplitude with scale factor (the three triplets of curves) is due primarily to the effect of the linear growth fact $D(a)$ on the normalization, σ (recall Eqn. 1.28). Second, as one varies the equation of state (within each triplet of curves), the density required for collapse also varies: a more powerful dark energy (*i.e.,* more negative w) allows fewer halos at a given density to collapse. This is depicted in the simulations shown in Fig. 1.10.

The idealized collapse process of spherical infall provides a starting point for defining halo quantities like size and shape (Bertschinger, 1985). In this approximation, the point at which a halo decouples from the background expansion is known as the turnaround point; it defines the edge of an idealized spherical halo that has undergone dissipationless collapse. However, two real-world complications affect the usage of this edge definition. First, collapse is not dissipationless; chaotic motion of particles generate a kinetic pressure and thus a time-varying potential during the collapse phase – leading to a "violent relax-

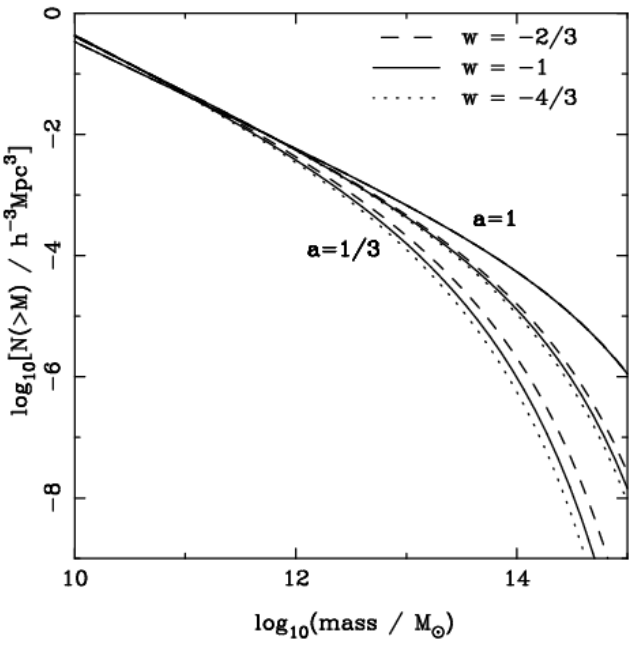

Figure 1.11: The predicted cumulative mass function of Sheth and Tormen (1999) for three different settings of the DE equation-of-state parameter, w, and at three different epochs, $a = 1/3, 2/3, 1$. The mass function changes with the scale factor, a, primarily due to the growth factor's evolution. The strength of the Dark Energy (the magnitude of w) determines how many halos can form at a given epoch. (Percival, 2005).

ation." Second, infall continues after the nominal collapse time: halos continue to accrete new material, blurring the edge between the halo and the background. Alternatively, halo edges and thus their masses may be defined as the total amount of mass encompassed by a sphere within which the local density is a factor, $\Delta = \rho/\rho_{\rm b}$, larger than the background density; that background density, $\rho_{\rm b}$, may be taken as the total critical energy density, $\rho_{\rm c}$, or the mean density, $\bar{\rho}$, at the given epoch. N-body simulations show that $\Delta \approx 200$ is approximately independent of cosmology and thus provides a basis for estimating edges and masses of halos.

The halo density profile is among the most simple and profitable of descriptions for halo shape. Under the assumption of spherical symmetry, or when they are spherically

averaged, halo density profiles are typically well-fit by a combination of power-laws,

$$\rho(r) \propto \left(\frac{r}{r_{\rm s}}\right)^{-a} \left(1+\frac{r}{r_{\rm s}}\right)^{-b}, \tag{1.31}$$

where $r_{\rm s}$ is the user-defined scale radius ($a = 1$ and $b = 2$ for Navarro et al., 1997). Triaxial halos have been explored primarily on the galactic scale (*e.g.,* Tinker and Ryden, 2002; Adams et al., 2007). Recent and upcoming works aim to shed light on halo and cluster structure in the context of galaxy cluster observations and cluster-finding (Corless and King, 2007; Rozo, 2010). This is an important area of research, since the halo abundance and cosmological constraints have been shown to depend on the size and shape of the halo (Lukić et al., 2009).

Cluster masses, however, cannot be observed directly. Only proxies for the mass can be observed. These observable signals can come in the form of emission from the baryonic components of clusters, or interactions between clusters and the cosmological background, like the CMB or space-time itself. A cluster's dark matter halo provides the primary potential well into which baryons fall, interact, and emit. The resulting melting pot contains galaxies, which shine in the optical (sub-μm) wavelengths; the typical mass proxy in optically selected clusters then is the *richness* or number of galaxies, $N_{\rm gals}$. The hot intracluster plasma permeates the potential and emits in X-rays (nm); from the plasma spectrum, gas temperatures and luminosities can be inferred to give two more mass proxies, $T_{\rm X}$ and $L_{\rm X}$, respectively; also, under some assumptions of the cluster shape and dynamical state, X-ray masses, $M_{\rm X}$, can be derived from the density distribution and temperature. The intracluster medium scatters CMB photons, creating distortions in the CMB temperature map, with magnitude $Y_{\rm SZ}$ and observable in the microwaves (sub-mm). The cluster potential can also deform space-time sufficiently to produce weak, but coherent distortions of background galaxies, producing a tell-tale pattern of alignment with the lensing cluster. This *weak lensing* signal provides another mass proxy, $M_{\rm WL}$, at optical wavelengths. In Fig. 1.12, we show

representative signals of each waveband for cluster, Cl-0016 (Holder, 2010). The physical origins of these signals, their relationships with mass, and their relationships amongst each other are discussed in detail in Chapter II.

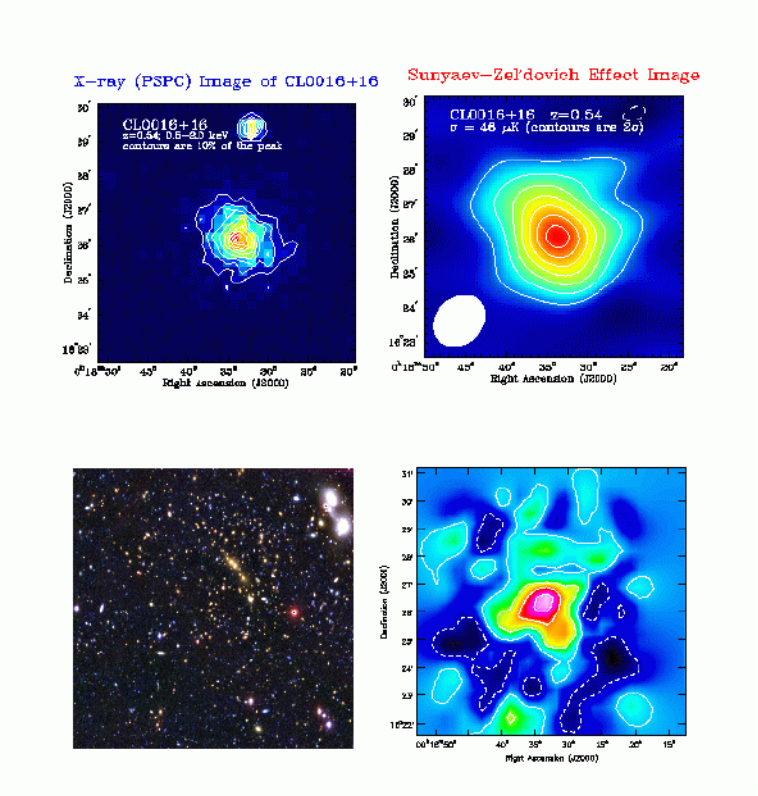

Figure 1.12: Multi-wavelength view of the intermediate redshift ($z = 0.53$) cluster, CL0016+16, in the X-rays (upper left), sub-mm wavelengths (upper right), weak lensing (lower right), and optical wavelengths (lower left). In the optical field of view, the red elliptical galaxies (which appear yellow) are strongly clustered immediately up and to the right of the image's center (Holder, 2010).

One of the principal challenges for cluster cosmology is the development of a robust relationship among all of the observed signals (mass proxies) and halo mass. The accuracy and precision of this relationship determines the fidelity of the halo mass function estimation, and thus the accuracy of cosmological parameter constraints. Mean signal-mass and signal-signal relationships typically take power-law form, where the probability for a halo of mass m and redshift z to produce a signal, S, is $\mathcal{P}(S|m,z)$. Convolving the distribu-

tion, $\mathcal{P}$, with the halo mass function over mass and redshift produces the expected number distribution function in a given signal,

$$n(S) \propto \int \mathrm{d}m\, \mathrm{d}V(z) n(m,z) \mathcal{P}(m,z|S). \tag{1.32}$$

like those found in Fig. 1.13. Characterizing these signal distributions (normalization, scatter, and form) and matching the predicted and observed signal distribution functions are key steps in constraining cosmology with clusters (Lima and Hu, 2005).

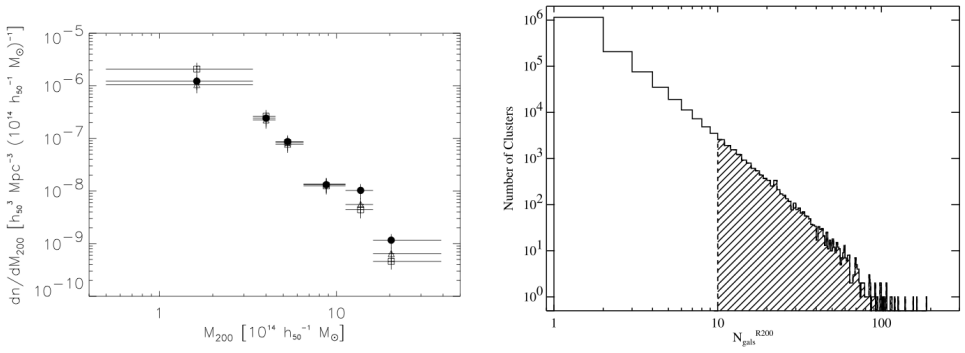

Figure 1.13: Number density distributions of clusters as functions of X-ray-derived hydrostatics mass, M_{200} (left; Reiprich and Böhringer, 2002), where '200' indicates the relative density with respect to the critical density; and numbers of galaxies, N_{gals} (right; Koester et al., 2007). Both distributions display strong power-law behavior – also a characteristic feature of halo mass functions.

The systematic uncertainties and peculiarities of cluster physics pose a challenge to drawing the connection between observable signal and mass. For example, the intracluster medium is not always relaxed and isothermal as many idealized studies have assumed in the past: evolving galaxies near the centers of clusters sometimes house active galactic nuclei (AGN), which can outshine both their host galaxies and clusters in the radio wavelengths and increase the entropy of the intracluster medium via jets of relativistic plasma. Moreover, the energy produced by AGN can significantly alter the ambient ICM and the evolution of surrounding galaxies; this activity modifies the entropy of clusters and amplifies the scatter in the relations between thermodynamic quantities, like L_{X} and T_{X}. Not

all clusters have relaxed to a virialized state, and many in fact just live as damped engines, forever approaching equilibrium at varying rates. The galaxies within a cluster can betray this continuous evolution via their asymmetric distribution; cluster morphology is likely to contribute scatter in the relationship between richness and cluster mass. Also, the SZ effect is susceptible to the systematic projection of all the gas along a cluster's line of sight; low-angular resolution SZ measurements alone are unlikely to be sufficient for removing this contamination.

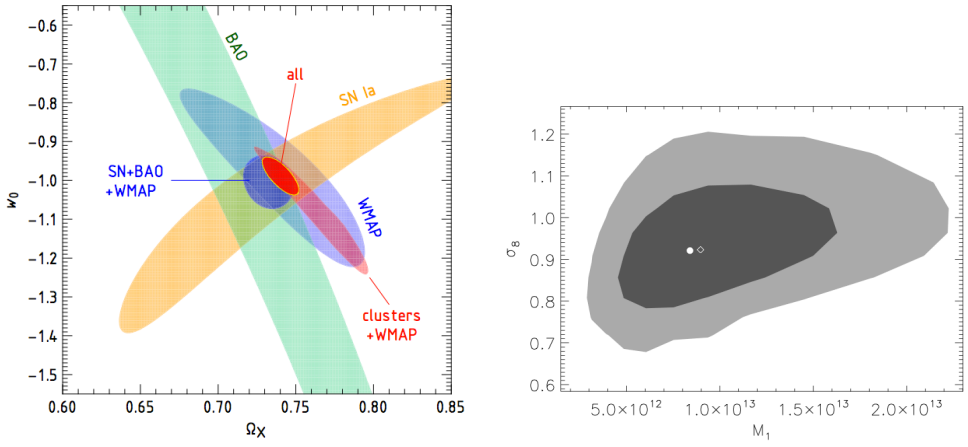

Figure 1.14: Confidence regions for cosmological parameters constraints from clusters. *Left:* X-ray-selected clusters from the 400 deg^2 survey are combined with complementary probes – supernovae, BAO and the CMB – to constrain the Dark Energy density and its equation-of-state parameter (Vikhlinin et al., 2). *Right:* Counts from the optical maxBCG galaxy cluster catalogue alone constrain the power spectrum normalization, σ_8 (recall §1.3.2), and a characteristic mass scale, M_1, which is used in the halo model to link richness and mass (Rozo et al., 2007).

Multi-wavelength observations of clusters have the potential to mitigate the aforementioned systematics. For example, the projection in the SZ signal is expected to be deconstructed with photometric redshifts from optical cluster observations. Some small-scale (often single and pointed) observations have been undertaken, but joint serendipitous surveys have not matured to the point of containing statistically profitable numbers of clusters. These are the holy grail of multi-wavelength cluster characterization, but it is not neces-

sarily the most efficient for modern observing capacities. It has been shown, however, that a well-planned medium-scale set of follow-up observations can achieve comparable precision on constraints as covering the same part of they sky with multiple full-size surveys (Wu et al., 2010). Nonetheless, ample cosmological constraints have arisen from independent cluster samples, like those from the SZ-selected sample from SPT (Vanderlinde et al., 2010), the optically selected maxBCG sample (Rozo et al., 2007) and the 400 deg^2 X-ray survey (Vikhlinin et al., 2); examples from the optical and X-ray wavelengths are shown in Fig. 1.14. They represent the state of the art for constraints from cluster samples in a single mass proxy.

1.5 Surveys of Galaxy Clusters: Toward a Multi-wavelength Future

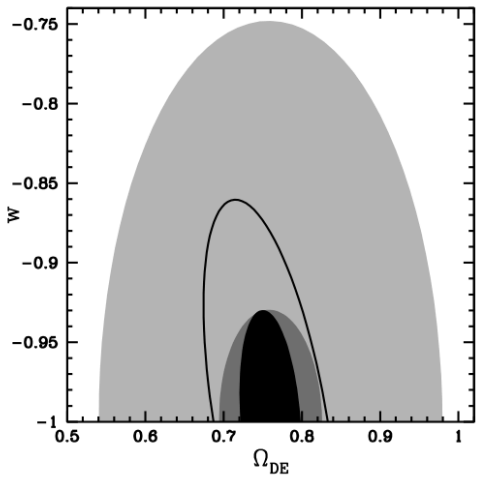

Figure 1.15: Theoretical constraints on the dark energy density and its equation-of-state parameter using both SZ and optical surveys of galaxy clusters. The largest (filled, light gray) ellipse shows constraints from clusters independently selected in each signal. The second-largest ellipse (solid, black line) indicates constraints when two-point correlations of clusters is added. The third largest (filled, dark gray) ellipse shows constraints from *jointly* selected clusters *without* correlation information, and the smallest (filled, black) ellipse shows constraints when clustering information is added to the joint selection (Cunha, 2009).

It has been predicted that the complementarity of some signals will make significant

enhancements in cosmological constraints. Consider a 4000 $\deg^2$ region of the sky, with two sets of clusters, each observed in different wavebands. Fisher analysis in the context of self-calibration (Levine et al., 2002; Majumdar and Mohr, 2004; Lima and Hu, 2005) predicts that cross-calibrating the two samples (*i.e.,* joining the samples before obtaining constraints) is more useful than combining the individual constraints – such a process can double the precision (Cunha, 2009). Now is the time to begin taking advantage of complementary data sets. Beyond SDSS and ROSAT, the future promises another round of larger surveys and instruments, like the Dark Energy Survey (DES, The Dark Energy Survey Collaboration, 2005), the Large Synoptic Survey Telescope (LSST, Ivezic et al., 2008) in the optical wavelengths, and the South Pole Telescope (SPT, Ruhl et al., 2004) and Planck (Mennella et al., 2010) in the sub-mm wavelengths. With such large-scale

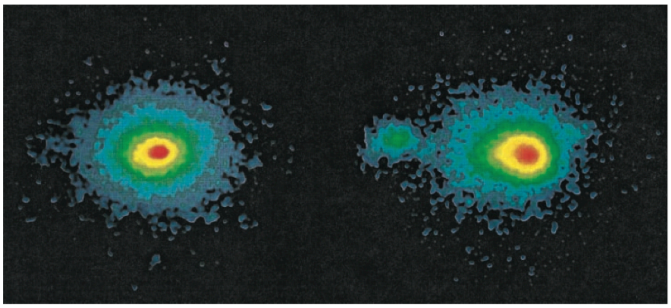

Figure 1.16: Maps of soft-band X-ray emission from the galaxy cluster AWM7 and from a Dark Energy-dominated hydrodynamical n-body simulation (Evrard, 1999).

science, must come intricate preparation for the surveys. A large part of our preparation and contemporary analysis involves large-scale simulations of the sky, against which to check our methods of data analysis for the real sky. From "God's-eye view" N-body simulations, we can construct virtual sky surveys that mimic observations. Fig. 1.16 shows an example of one simulated x-ray cluster and one real cluster, both from the point of view of an observer; can you tell which is which? The precision of our constraints will depend on the fidelity of our mimicry.

The aim for this dissertation is to provide the backdrop in which to test the hypothesis of this work and develop methods to enhance cosmological constraints for joint surveys. This dissertation aims to construct an arena for analysis of multi-wavelength signals of clusters in preparation for future astronomical surveys.

CHAPTER II

Observable Signatures of Galaxy Clusters

Clusters of galaxies live at the edge of linearity of large-scale structure, and, through the distribution of their masses, can serve as accurate tracers of the expanding background. Proxies of cluster mass originate with the cluster baryons (*e.g.,* thermodynamic quantities), as well as with interactions between the cluster and astrophysical objects in the background (*e.g.,* weak lensing). Typically, signal-mass scalings manifest as power-law relationships with non-negligible intrinsic scatter; and the power-laws can break or experience higher scatter at lower masses and signals. Both pure stochasticity and the evolutionary diversity of clusters still undergoing formation add to the scatter, but so do observational/analysis systematics, like the choice of cluster center and definitions of shape.

Each signal can describe a unique cluster aspect, but no individual signal betrays the entire morphology, dynamics, and matter content of a cluster. To fully account for their multi-faceted nature, the signals must be joined into a unified picture. Upcoming surveys at sub-millimeter and optical wavelengths will complement existing efforts in the X-ray (Ebeling et al., 1998; Böhringer et al., 2002; Boehringer et al., 2006; Pierre and Consortium, 2006) and optical (Miller et al., 2005; Koester et al., 2007) bands. The South Pole Telescope (SPT, Carlstrom et al., 2009) and the Atacama Cosmology Telescope (ACT, Hincks et al., 2009) have already taken first light; the former anticipates discovery of at

least $\sim$1000 clusters. Survey cross-calibration will enable detailed characterizations of the inter-relationships among observable mass proxies, and the future of precision cosmology derived from number counts and clustering (Levine et al., 2002; Majumdar and Mohr, 2004; Lima and Hu, 2004, 2005) may come to rely on such an interwoven tapestry. In this chapter, I discuss the individual threads in that tapestry, and how they have begun to interleave: I focus on the origin of observable cluster signatures and mass proxies, and their relation to the total cluster mass.

2.1 Galaxy Distributions in Clusters (Optical Wavelengths)

As the first halos collapsed, they drew gas from the pre-galactic medium into them; the gas then cooled and condensed to create stars which eventually returned their contents to the resultant inter-galactic medium, which grew warmer through this stellar feedback, as well as merging events, and a host of other processes. Mergers and relaxation periods created and smoothed out substructure, providing evolving wombs for the hierarchical build-up of galaxies. The "core condensation" theory (White and Rees, 1978) considers halos the birthplace of individual galaxies: these halos and galaxies may stream along cosmic filaments or already be born into the nodes. The local environment of the subhalo and galaxy then largely determines their character.

Galaxies were segregated into morphological types by Hubble (1936), whose classification is still used today. Red galaxies have an elliptical shape and were incorrectly thought to have formed first, leading to the misnomer, "early types"; they actually have a lower relative rate of star formation today, are thus redder, and tend to reside in the denser regions, like clusters. Spirals, on the other hand, tend to be bluer in color and were originally thought to form *from* the ellipticals – making them "late types"; they, however, have higher star formation rates, are thus bluer and younger, and reside in the field.

The earliest cluster catalogues were made counting galaxies by eye on photographic plates (*e.g.,* Zwicky, 1937; Abell, 1958). These early catalogues proved exceedingly useful. For example, Zwicky (1937) used the virial theorem and measures of galaxy velocities to deduce the existence of the "invisible" dark matter. Automated detections have accelerated in the last two decades, given the increasing availability of large galaxy redshift surveys, like the DEEP project (Koo, 1998; Gerke et al., 2005), the Two-micron All Sky Survey (2MASS, Kleinmann et al., 1994), the Palomar Distant Cluster Survey (Postman et al., 1996), the Sloan Digital Sky Survey (SDSS, York et al., 2000), and the Red Sequence Cluster Survey (RCS, Gladders and Yee, 2005). To identify, measure and characterize clusters, search

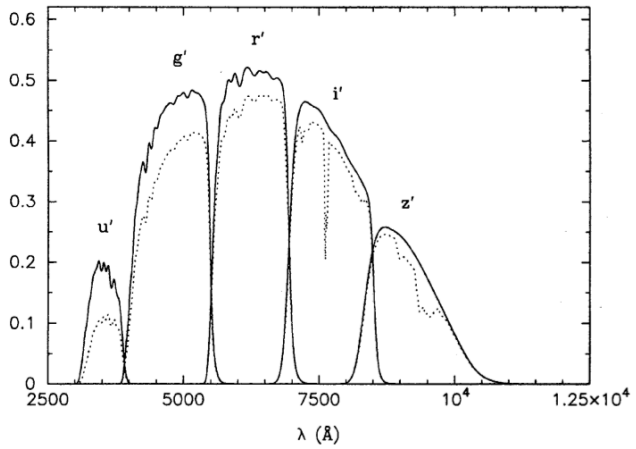

Figure 2.1: The filter spectra – $u'g'r'i'z'$ bands – for SDSS; the solid line shows the SDSS camera response, while the dotted line shows the Monitor Telescope response. The latter defines the photometric system, but the two responses are calibrated to be identical in the u' band (Fukugita et al., 1996).

algorithms typically take advantage of several characteristic features of galaxies in the cluster environment. In this section, we discuss these features in the context of cluster detection: color aids in general population segregation; central galaxies are potentially unique tracers of clusters; and the photometric redshift is a reliable distance proxy. We conclude with a brief overview of the scaling relations of clusters detected based on these

features.

2.1.1 Cluster Galaxy Photometry

A characteristic feature of the spectrum of elliptical and lenticular galaxies is the 4000 Å break, which arises due to an abrupt build-up of absorption lines in the spectrum near that wavelength in the galaxy's rest-frame. Only a small fraction of galaxies can be observed long enough in order to obtain a full spectrum. Modern surveys are thus often relegated to multi-band photometry, such as the *ugriz* system of SDSS (see Fig. 2.1 from Fukugita et al., 1996), which serves as a low-resolution spectrum. Photometric galaxy surveys produce multi-band data that can be used to classify their morphology and environment and triangulate galaxy positions.

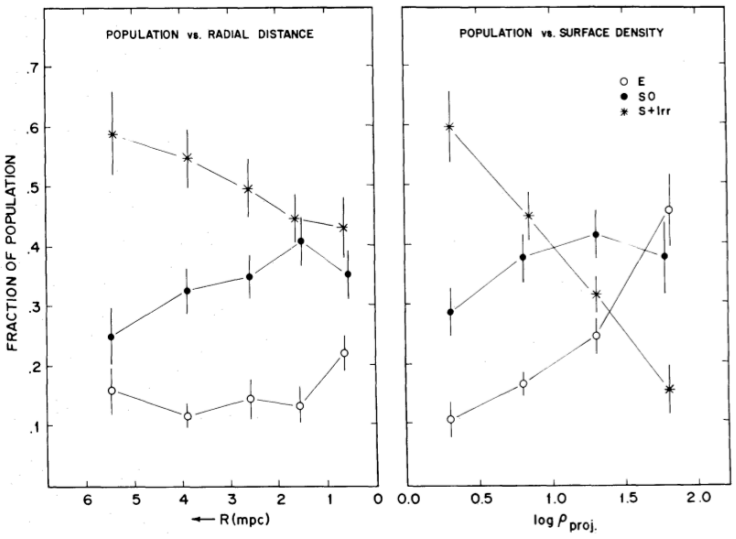

Figure 2.2: Relative fractions of galaxies by type as a function of cluster-centric radius (left) and log-surface density (right). In six moderately irregular, rich clusters observed at Las Campanas galaxies were classified as elliptical (E, open circle), lenticular/S0-type (closed circle), or spherical/irregular (S+I, asterisk). Each species is shown to trend with cluster-centric position and local density, displaying clear morphological segregation as function of environment. In Fig. 4 of that same work, the author shows the relative fraction as function of log-density for *all* galaxies in the cluster sample *and* the field; the trends in that figure are clearer and smoother, but only show functions of density, not radius (Dressler, 1980). Dressler later reiterated on this exercise to similar effect (Dressler et al., 1997).

The ratio of magnitudes in adjacent bands produce a relative flux, known as *color*, for a galaxy, which reflects star formation rate and often age. Local environments play a crucial role in shaping the evolution of galaxies: Dressler (1980) found that the fraction of red galaxies decreases with increasing cluster-centric distance, while the blue fraction does the opposite (see Fig. 2.2). Within the dense cluster environment, star formation in a galaxy is more likely to be quenched. A galaxy's transition from cluster outskirts toward the cluster center allows for, and often accelerates, the quenching process via interaction with the hot plasma of the intracluster medium (*e.g.,* ram pressure stripping) or with the central galaxy; while the effect is well observed, the mechanisms driving this stage of evolution are a matter of active research.

The observational fact that ellipticals and lenticulars are more likely to reside within clusters than in the field leads to a boon for cluster detection when these populations are viewed in *color-magnitude* space (Kodama and Arimoto, 1997). Cluster galaxies are scattered narrowly about the "E/S0 ridge-line" (Visvanathan and Sandage, 1977; Bower et al., 1992; Annis et al., 1999), which typically has null to negative slope depending partly on the cluster's evolutionary state (Gladders et al., 1998; Hao et al., 2009). The cluster red sequence was first used as a cluster identification tool by Gladders and Yee (2000); see Fig. 2.3. Not only can the cluster ridge-line be used to discriminate between cluster and field galaxies, but to provide a measure of distance. The color of cluster galaxies evolves with redshift, sufficiently enough to be an efficient distance proxy at many epochs – a relationship more robust at late times (Renzini, 2006; Maraston et al., 2009). Cluster analyses in the local universe ($z < 0.4$) use the color, $(g-r)$, but observations and population synthesis models of elliptical galaxies show that beyond $z \sim 0.4$, the slope of the $(g-r)$ color with redshift becomes negligible, and thus there is no mapping between color $(g-r)$ with redshift. The $(i-r)$ and $(z-i)$ colors have sufficient slopes with redshift

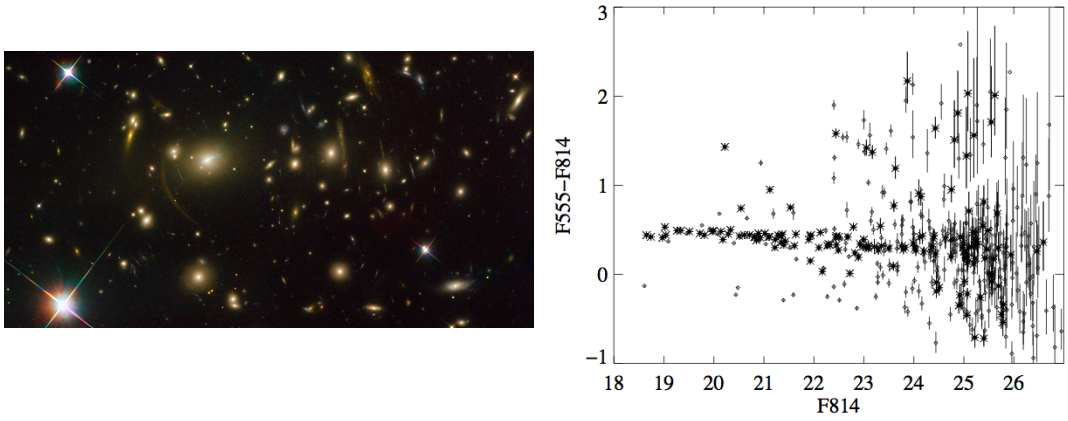

Figure 2.3: An image of the cluster, Abell 2390, from the Hubble Space Telescope (Martin and Long, 2008). The observed color-magnitude diagram – epitomizing the *red sequence* as a tight ridge-line from about 18.5 to about 23 in magnitude – for the same cluster in the Red-Sequence Cluster Survey (RCS; Gladders and Yee, 2000). The asterisks represent galaxies that were morphologically selected as early types, and diamonds indicate other galaxies in the image, which are then taken to be field galaxies. Error bars are 1σ.

to be employed at higher redshifts – $0.4 \leq z \leq 0.7$ and $0.7 \leq z \leq 1.0$, respectively.

2.1.2 Photometric Redshift as a Distance Proxy

An alternative (and occasional complement) to color discrimination for determining the distance is the *photometric redshift*. Galaxy spectra are redshifted by cosmological expansion. The photometric redshift is that which can scale the aforementioned 4000 Å break in the observer's frame to its rest-frame position (Connolly et al., 1995). Algorithms for the determination of photometric redshifts span a broad range, from template-fitting (Bolzonella et al., 2000; Massarotti et al., 2001) to machine learning (Collister and Lahav, 2004; Gerdes et al., 2010). Typical of all the methods, the scatter increases with redshift for a given color choice, but this might be expected due to an increase in scatter of the color itself with increasing redshift. Industrial comparison exercises have recently been undertaken, showing that outlier rates persist at the 5% level, which may be the bottleneck for some science in upcoming photometric surveys, like DES (Hildebrandt et al., 2010). Redshift errors in cluster and galaxy surveys range from $\sigma_z = 0.007$ (Kim et al., 1b) to

0.0147 (Goto et al., 2002) to $\sim$0.03 for SDSS; in other surveys, they are as large as 0.033 (Gal et al., 2009) and 0.05 (Gladders and Yee, 2005). The photometric redshift error evolution varies with survey configuration and algorithm (Hildebrandt et al., 2010), and the commonly assumed shape, $\sigma_z \propto (1+z)^{\alpha}$, has not yet been verified. The propagation of these errors to cluster-finding is a key issue, currently a subject of active research.

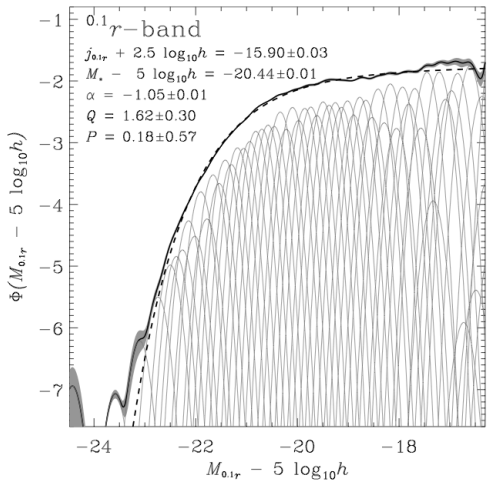

Figure 2.4: The luminosity function of 147,986 $z = 0.1$ galaxies observed by SDSS in the r band. The symbols in the upper left are fit parameters from the fit function for this work. The gray band about the fit represents 1σ uncertainties about the fit. The light gray curves show the individual Gaussian basis functions that comprise the fit function. The dashed line shows the fit to the Schechter luminosity function (Blanton et al., 2003).

2.1.3 The Search for Central Galaxies

Starting with the seed of matter residing in a region of high local density, halos and clusters from through two concurrent processes. In one process, the single initial seed or subhalo *monolithically* accumulates matter, as does the galaxy that forms at the center of the subhalo. The local gravitational potential attracts other subhalos and their galaxies from nearby cosmic filaments; these halos can evolve distinctly from the initial central galaxy or become disrupted and have their matter commingled with the central subhalo and galaxy. In either case, the seed galaxy has a high likelihood of becoming a bright, red

object that resides very near the center of the gravitational potential: it has a great deal of time to accumulate gas and stars from disrupted galaxies, increasing its brightness; and those stars are more likely to have relatively little star formation, given their tumultuous environment of accumulation and disruption in which they reside. The central galaxies of clusters are highly sought after objects: if we can identify the species of galaxy that is likely to be a center, then we know where to look for clusters and half the job is completed.

Brightest cluster galaxies (BCGs) comprise the broadest class of potential central galaxies: when classified as both the most luminous and the reddest of the cluster galaxies, they exhibit a set of unique characteristics: they have extended envelopes, and active galactic nuclei (AGN) are more likely to form within them; they have a higher internal velocity dispersion than satellite galaxies; and they appear to form via dissipationless mergers with primarily radial orbits (von der Linden et al., 2007). By definition, they reside at the bright end of the luminosity function, an example of which we show in Fig. 2.4: it contains the r-band luminosity density distribution of SDSS $z = 0.1$ galaxies, including a fit to the Schechter luminosity function.

Luminous red galaxies (LRGs) in clusters are often the BCG: they're redder than average and tend to occupy the bright end of luminosity functions. However, most massive halos should host multiple LRGs at some point, as required by LRG two-point correlation functions, which show high amplitude at small (sub-cluster) scales (Zheng et al., 2009); this may be at odds with the the expectation that each cluster has just one BCG.

In the construction of the velocity dispersion-richness relation for clusters, Becker et al. (2007) measure velocity dispersion with respect to the BCG. However, the BCG is often not at the spatial or density center of the cluster; and the extended profile and color do not always correspond with the brightest galaxy. The apparent inhomogeneity of the BCG population calls into question its consistent utility in identification of clusters and cluster

centers (Skibba et al., 2010). Nevertheless, in conjunction with photometric redshifts, the BCG has been incorporated into likelihood methods to find over 10^4 clusters with strong confidence in the SDSS (Koester et al., 2007).

2.1.4 Scaling Relations

Bulk measures of cluster size and content aid in characterizing an optically observed cluster. First, dimensional arguments suggest a power-law scaling between radius and richness via the assumptions of spherical symmetry and of a power-law scaling between richness and mass:

$$R \propto M^{1/3} \sim N^{\alpha/3}, \tag{2.1}$$

where mass is assumed to scale with N; $\alpha \sim 0.6$ for the maxBCG catalogue (Hansen et al., 2005). The radius can be measured in a similar fashion as halo masses in spherical-overdensity-based halo finders (recall §1.4). The virial theorem applied to galaxy clusters suggests that the galaxy velocity dispersion scales with the cluster mass to a factor of the velocity bias (Becker et al., 2007; Evrard et al., 2008).

The cluster mass can also be measured through the lensing of background galaxies. The cluster potential produces minor, coherent distortions of galaxy shapes and positions, which place the galaxies into a weak pattern of tangential alignment with the lensing cluster. From this shearing of galaxy light, a projected mass surface density can be derived. Since the signal is weak, stacking of clusters can be used to enhance the signal-to-noise ratio. However, the uncertainty of the cluster center persists as a limiting source of systematic error (Sheldon et al., 2001; Johnston et al., 2007).

The Halo Occupation Distribution (HOD) aims to model the probability that a halo of mass M contains $N_{\rm gals}$ galaxies – *i.e.,* $\mathcal{P}(N_{gals}|M)$ – a direct route between richness and mass. It has been used in exploring the galaxy-matter bias in simulations, testing

cosmological models, and informing galaxy formation theories (Berlind and Weinberg, 2002; Weinberg et al., 2004). A related model, the conditional luminosity function, provides a direct connection between galaxy light and the underlying dark matter (Yang et al., 2003). The HOD methodology also provides the basis for a measure of fidelity in cluster-finders, as will be seen in Chapter V.

The optical luminosity, $L_{\rm opt}$, has not yet proved as competitive a mass proxy as richness: it is incomplete without measures of the intracluster optical (stellar) light. Measurements of intracluster light (*e.g.,* Krick and Bernstein, 2004, 2007) will eventually be incorporated with cluster-finding and characterization for several potential purposes. For example, it could be used to discern internal cluster structure and thus differentiate classes of clusters – likely as a counterpart to X-ray studies of substructure in the hot intracluster plasma.

2.2 The Hot Intracluster Medium (X-rays)

Hot plasma surrounds cluster galaxies, suffusing the intra-cluster space. X-ray observations reveal thermal bremsstrahlung emission at temperatures of 10^7-10^8K ($1-10\,$keV), and particle densities in the range $10^{-2}-10^{-4}\,{\rm cm}^{-3}$ (*e.g.,* Kellogg et al., 1972; Serlemitsos et al., 1977) . The plasma is composed primarily of ionized hydrogen, along with trace abundances of heavier ions which have about a third of the solar abundance (0.3 $Z_\odot$); the spectral density of the continuum emission is related to the the electron number density, $n_{\rm e}$, and the plasma temperature of the ICM, $T_{\rm e}$, by

$$\epsilon_X \propto n_e^2 T_e^{-1/2} e^{-E/k_B T_e}, \tag{2.2}$$

where E is the photon energy. An instrument that is primarily sensitive in the soft band ($E = 0.3-2.0$keV) gives an image of a hot cluster (*i.e.,* $E \leq k_{\rm B}T$) that primarily reflects the density. At higher energies, however, the exponential cuts off the emission of a cooler cluster.

2.2.1 The Isothermal Assumption and Hydrostatic Mass Estimates

From the equation for emission (Eqn. 2.2), I focus first on the number density. The King density profile (King, 1966) was first used to describe star clusters and later dark matter halos. The β profile,

$$n_e(\theta|\beta,\theta_{\rm c}) = \left[1+\left(\frac{\theta}{\theta_{\rm c}}\right)^2\right]^{(1-3\beta)/2}, \tag{2.3}$$

is a robust approximation to the King profile for clusters with isothermal ICM (Cavaliere and Fusco-Femiano, 1976). Assuming isothermal ICM and spherical symmetry, the surface brightness profile is given by the integration over the density along the given line of sight at a cluster-centric radius, r, as in

$$\begin{aligned} S_X(\theta) &= \frac{1}{4\pi(1+z)^4}\int n_e(r) n_H(r)\Lambda(T){\rm d}\ell_r \\ &= S_{X,0}\left[1+\left(\frac{\theta}{\theta_s}\right)^2\right]^{-3\beta+1/2}. \end{aligned} \tag{2.4}$$

with appropriate approximations for the hydrogen density $n_{\rm H}$ (*e.g.,* as a multiple of the electron density) and the cooling function, $\Lambda(T)\sim\sqrt{T}$, for bremsstrahlung. The surface brightness can be fit for the parameters of the core radius, $\theta_{\rm c}$, and profile power, β, that go into the density model of Eqn. 2.3. To recover the cluster mass profile in the case of hydrostatic equilibrium, the electron density ($n_e\propto\rho$) is then combined with the equation for the binding mass, M,

$$M(r) = -\frac{k_B T\, r}{\mu m_p G}\left(\frac{{\rm dln}\rho}{{\rm dln}r} - \frac{{\rm dln}T}{{\rm dln}r}\right), \tag{2.5}$$

where $\mu\sim 0.6$ is the mean molecular weight, $m_{\rm p}$ the proton mass, G the gravitational constant, $M(r)$ is the total mass *within* radius r, and $T=T(r)$ the gas temperature *at* that radius. For isothermal (*i.e.,* ${\rm dln}T/{\rm dln}r\rightarrow 0$), virialized clusters with a β profile, the gravitational potential energy is proportional to the kinetic energy, such that

$$k_B T_X \propto \frac{M}{r}, \tag{2.6}$$

and the accompanying expectation from self-similar evolution is

$$M_{\rm X} \propto T_X^{2/3} E^{-1}(z), \tag{2.7}$$

where $T_{\rm X}$ is the X-ray derived temperature, $M_{\rm X}$ is the X-ray derived mass, and $E(z)$ is the normalized Hubble parameter of Eqn. 1.13 (Kaiser, 1986; Voit, 2005a). Self-similar evolution occurs when only gravitational interactions drive a cluster's formation.

The other main component of the emission equation, the temperature, is typically measured from a one- or multi-component fit to the plasma spectrum: the slope, as well as particular emission lines, determine the plasma temperature. The *emission-weighted* temperature,

$$T_{ew} = \frac{\int {\rm d}\ell n_e n_H \Lambda(T) T}{\int {\rm d}\ell n_e n_H \Lambda(T)}, \tag{2.8}$$

has often been used as a simple proxy for the spectroscopic temperature that is actually measured during observations. However, $T_{\rm ew}$ systematically underestimates the spectroscopic temperature in a thermally complex ICM. A *spectroscopic-like temperature*,

$$T_{sl} = \frac{\int {\rm d}\ell n_e n_H T^{-1/2}}{\int {\rm d}\ell n_e n_H T^{-3/2}}, \tag{2.9}$$

more faithfully tracks clusters, regardless of thermal complexity (Mazzotta et al., 2004). In simulations, the full effect of the mis-estimate can be uncovered. When $T_{\rm sl}$ is used with the hydrostatic mass model of Eqn. 2.5 and compared to the true measure of the gas temperature, the hydrostatic masses are underestimated by as much as 50%. This bias leads to significant biases in cosmological parameters (Rasia et al., 2005). Challenges to the assumption of isothermality in clusters were buttressed by observations of radially decreasing temperature profiles in hot clusters (Markevitch, 1998; Vikhlinin et al., 2005), as well as high-resolution hydrodynamic simulations of clusters (Rasia et al., 2004). The

temperature profile,

$$T(r) = \langle T \rangle T_0 \left[1 + \left(\frac{r}{\alpha\, r'}\right)^2\right]^{-\beta}, \tag{2.10}$$

provides a more apt description of the thermally complex ICM, but it still assumes spherical symmetry (Loken et al., 2002; Hallman et al., 2006); r' is a scale radius denoting the distance within which the average temperature, $\langle T \rangle$, is measured. When included as part of a *hydrodynamical equilibrium* model (along with the gas velocity structure) a more robust mass determination can be made (Rasia et al., 2006). In order to trace extra-cluster gas, properly model the intracluster gas dynamics, and test the link between clusters and the cosmic baryon fraction (Allen et al., 2004), we will likely need better substructure studies and a new methodology for describing density and temperature distributions in the ICM.

2.2.2 An Example of Thermal Complexity

Another link to the ICM, and in particular the temperature is the cluster luminosity, which is a measure of the emission over the volume V. Thus, we can relate the X-ray luminosity $L_{\rm X}$ to the temperature,

$$L_{\rm X} \propto \epsilon V \propto n_{\rm e}^2 T^{1/2} r^3, \tag{2.11}$$

and the self-similar expectation is

$$L_{\rm X} \propto T_{\rm X}^2 E(z), \tag{2.12}$$

given $M = \rho_{\rm c}(z) r^3$, $\rho_{\rm c}(z) \propto E(z)$, $n_{\rm e} \propto M/r^3$, and Eqn. 2.6.

Characterizations of scaling relations like that in Eqn. 2.12 have moved beyond the slopes and intercept to focusing on a stochastic model with log-normal scatter about the mean population behavior (Stanek et al., 2006; Reiprich, 2006). We focus on such efforts in Chapter III, but discuss a very useful example here, of the evidence that slope and scatter

can be affected by evolution and gasdynamics. Early models of the ICM were based on high central densities and an inferred central cooling time much less than the Hubble time. This led to the expectation that gas condensed to the cluster center and, upon cooling, had converted into stars and radiated away energy, necessitating the gas from larger radii to then *flow* toward the center and continuously feed this *cooling*. Given the low temperatures and high densities, this would produce universally low central entropies in clusters, as seen in

$$K = k_{\rm B} T_{\rm e} n_{\rm e}^{-2/3} \qquad \Longrightarrow \qquad K \propto T_{\rm X} E^{-4/3}(z), \tag{2.13}$$

where the expression on the right is the self-similar expectation. However, these cooling flows are rarely observed, and so X-ray clusters have typically been culled into two classes, cool-core and non-cool-core, those with and without a cooler central regions. These cooling flows add complexity to the ICM and the scaling relations, typically increasing the scatter, especially in the $L - T$ relation, as shown in Fig. 2.5. Markevitch (1998) excised the central regions in clusters with cooler cores, thereby reducing the $L - T$ scatter; and a power-law fit to the resulting relation gives an expectation steeper than self-similar. Non-cool-core clusters must have some non-gravitational mechanism to prevent the gas condensation. Simulations demonstrate that supernovae, stellar winds, or AGN feedback have the potential to produce this steepened slope (Metzler and Evrard, 1993; Bialek et al., 2001) through a pre-heating of the ICM at an early epoch (*e.g.,* $z \leq 4$). Physically, the pre-heat mechanism increases the gas energy, which makes the gas less bound, particularly in less massive clusters; this preferentially increases the entropy in low-mass clusters, shifts the adiabat, and breaks self-similarity. An example of non-gravitational heating is provided by the cluster, Abell 2052, viewed in the X-rays with radio contours overlapped (Fig. 2.6); it appears that something near the cluster core has expelled gas from most of the inner regions. Although they are the primary candidate for the single-mechanism preheat model,

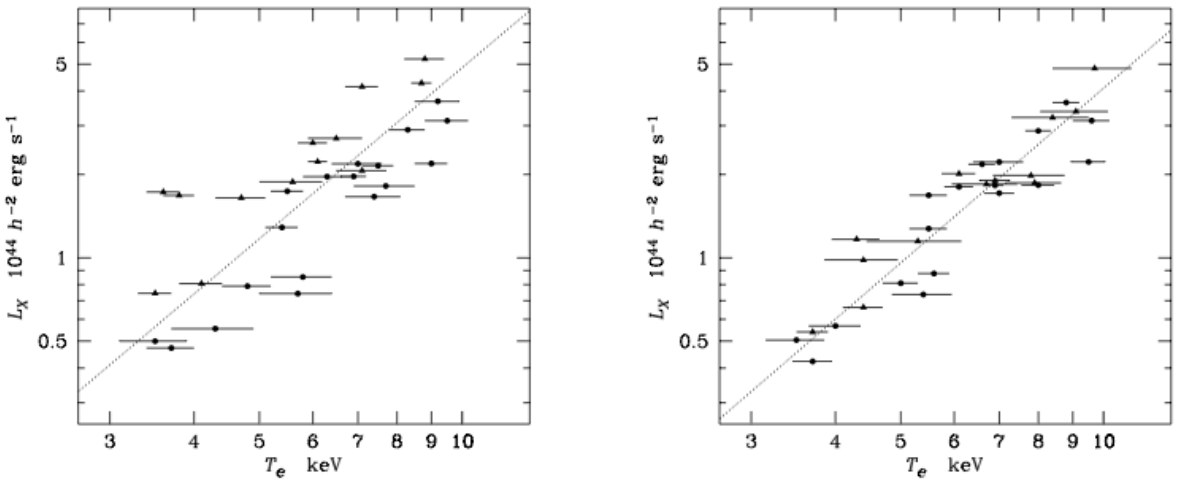

Figure 2.5: Soft-band X-ray luminosities (from ROSAT) and temperatures (from ASCA) for ~ 30 clusters. *Left*: total luminosities within $1\mathrm{h}^{-1}$Mpc and spectroscopic temperatures. *Right*: luminosities and emission-weighted temperatures from temperature maps with cooling flow regions removed (Markevitch, 1998).

AGN are not well understood, either in their exact origins or their distribution with respect to clusters; that they are the lone mechanism of non-gravitational heating remains a matter of debate (Conroy and Ostriker, 2008).

2.3 The Sunyaev-Zel'dovich (SZ) Effect (Radio Wavelengths)

As photons stream from the last scattering surface after recombination, they encounter large-scale structure. For example, photons passing through the intracluster medium are inverse-Compton scattered to higher energies (Sunyaev and Zeldovich, 1972). Non-relativistic thermalized electrons in random motion incur an effect that amounts to the integration of the plasma's electron pressure, $P_\mathrm{e} \propto n_\mathrm{e} T_\mathrm{e}$, along the line of sight, producing the *thermal* Sunyaev-Zel'dovich (tSZ) effect:

$$y_\mathrm{tSZ} = \frac{k_\mathrm{B}\sigma_\mathrm{T}}{m_\mathrm{e}c^2} \int \mathrm{d}\ell \, n_e T_e, \tag{2.14}$$

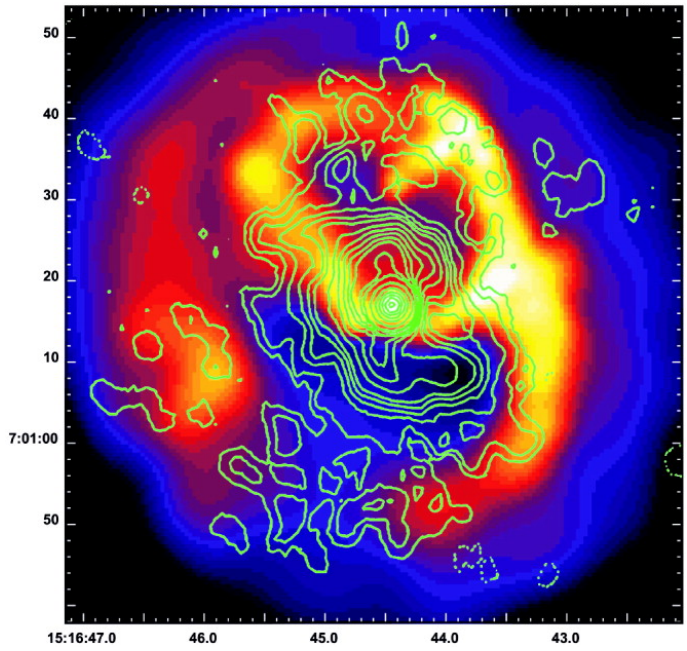

Figure 2.6: Radio contours of galactic radio source, 3C 317, overlaid onto a Chandra X-ray image of the central 76" x 76" region of cluster, Abell 2052. This gives an example of a mechanism – extended jets of radio emission – that can disrupt thermal relaxation of the ICM or prevent cooling flows (Blanton et al., 2001).

where $k_{\rm B}$ is the Boltzmann constant, $\sigma_{\rm T}$ the Thomson cross-section, $m_{\rm e}$ the electron mass; c the speed of light; and $n_{\rm e} = n_{\rm e}(\ell)$ and $T_{\rm e} = T_{\rm e}(\ell)$ are the electron number density and temperature at a distance, ℓ, from the observer along the line of sight. A much smaller *kinetic* Sunyaev-Zel'dovich (kSZ) effect is due to CMB Comptonization by bulk motion of plasma that occurs along the observer's line of sight

$$y_k = \frac{\sigma_{\rm T}}{c} \int {\rm d}\ell \, n_e v_r, \tag{2.15}$$

where $v_{\rm r}$ is the radial velocity along an observer's line of sight.

The individual spectral dependencies of the distortion from thermal and bulk motion take the forms,

$$g(x) \equiv x \frac{e^x + 1}{e^x - 1} - 4, \tag{2.16}$$

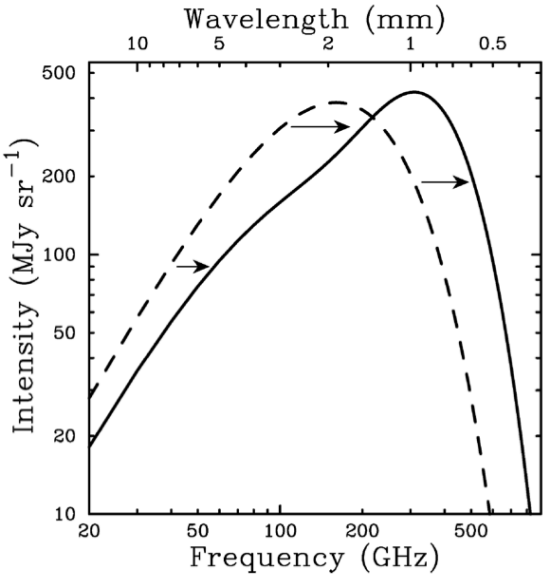

Figure 2.7: The CMB spectrum, undistorted (dashed) and distorted by the thermal SZ (solid). Following Sunyaev and Zeldovich (1980), the distortion shown is for a fake cluster that is 10^3 times as massive as a typical massive galaxy cluster (Carlstrom et al., 2002).

and

$$h(x) \equiv \frac{x^4 e^x}{(e^x - 1)^2}, \tag{2.17}$$

respectively, where $x \equiv h\nu/kT_{\rm CMB} \sim \nu/6.85\,{\rm GHz}$. The resulting CMB temperature fluctuations from the individuated effects are

$$\frac{\Delta T_{\rm tSZ}}{T} = y_{\rm tSZ}\, g(x) \tag{2.18}$$

$$\frac{\Delta T_{\rm kSZ}}{T} = y_{\rm kSZ}\, h(x), \tag{2.19}$$

where T is the CMB temperature. The distortion of the CMB due to the thermal effect is shown in Fig. 2.7: decrements (increments) in the brightness occur for frequencies below (above) the null frequency $\nu_{\rm null} = 218\,{\rm GHz}$, at which there is no SZ effect and the dashed and solid curves cross. The original formulation of these effects for non-relativistic electrons suffices for frequencies on the Rayleigh-Jeans side of the CMB spectrum – *i.e.,* $\nu \leq 350\,{\rm GHz}, x \leq 5$ (Kompaneets, 1957; Zeldovich and Sunyaev, 1969; Sunyaev and Zel-

dovich, 1972, 1980). Above this energy, that is for high electron temperatures, the frequency re-distribution must be re-calculated for strong scattering. However, modern SZ experiments measure the effect well below or near the null $\nu \leq 330\,\mathrm{GHz}$ (Wright, 1979; Fabbri, 1981). Fig. 2.8 shows a cluster observed in three frequency bands – two below the null and one very close the null: as expected, the sub-null observations produce a decrement (dark spots) in the CMB, while no discernible distortion occurs at the null.

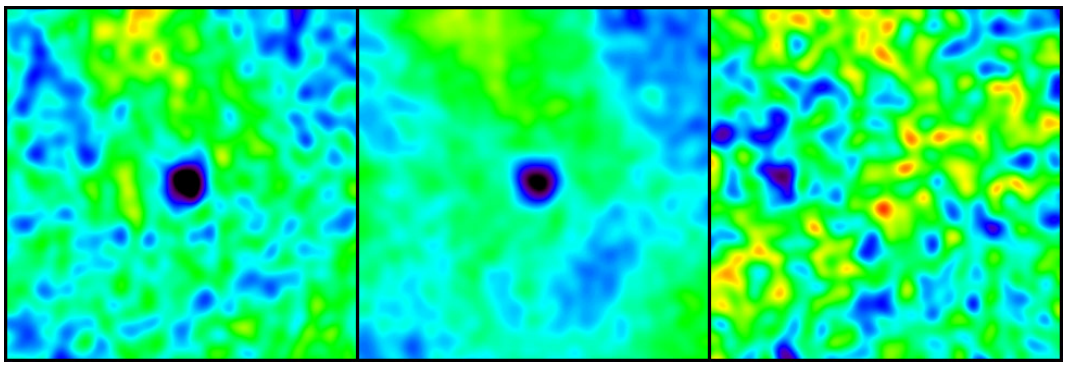

Figure 2.8: Images of a galaxy cluster in three bands (95, 150, and 220 GHz), discovered through its SZ effect by the SPT. The color scale in each band is $\pm 200\mu$K, and the images have side-lengths of $20'$. The cluster is clearly seen as decrement of CMB photons at 95 and 150 GHz and is not seen at 220 GHz, near the null. This is exactly the predicted spectral behavior of the SZ effect from the hot gas in galaxy clusters (The SPT Team, 2010).

2.3.1 SZ Power Spectra

The *secondary* CMB anisotropies due to the thermal and kinetic effects are shown alongside the CMB anisotropies in hydrodynamic simulations (Fig. 2.9). Springel et al. (2001) carried out simulations with various levels of pre-heating: the larger the entropy injection, the lower the thermal SZ power; also, the peak in the thermal SZ power shifts to lower angular scales. This can be related to how the gas is affected during pre-heating: gas of the ICM can escape the cluster potential, producing a stretched gas density profile, giving a larger correlation scale for the Comptonizing gas.

While the kinetic SZ effect causes a relatively small shift in the power spectrum, the

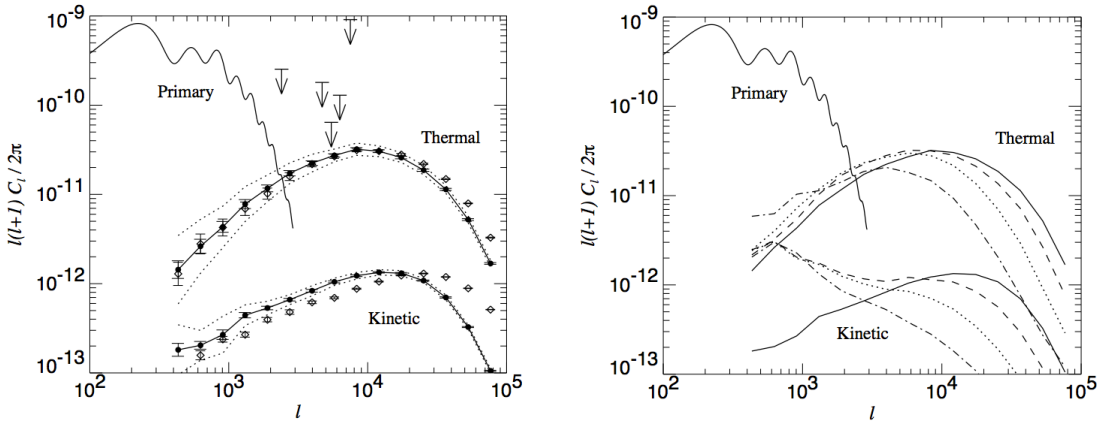

Figure 2.9: Angular power spectra of the "Primary" CMB anisotropy, and the "Thermal" and "Kinetic" SZ secondary anisotropies. The primary CMB power spectrum in both panels is based on numerical calculation (*e.g.,* CMBFAST;Seljak and Zaldarriaga, 1996). *Left*: the mean and error for power in an ensemble of 1° SZ sky simulations; filled points correspond to the ensemble from the large simulation box, while diamonds correspond to the smaller box; dotted lines show the variance between the maps. Arrows show upper sensitivity limits for contemporary surveys. *Right*: the angular power averaged over an ensemble of 15 maps in the large-box simulation; energy is injected at redshift $z = 7$ with the values, 0.0, 0.1, 0.3, 1.0 keV (solid to dot-dashed). The impact of the energy injection on the gas distribution is to de-localize it, and thus shift the peak of the spectrum of correlations to larger angular scales, and thus lower ℓ (Springel et al., 2001) .

thermal SZ power spectra has a large magnitude and very strong potential for contributing to cosmological constraints. First of all, modelling of the gas distribution near clusters has helped to feed a variety of methods for studying gas physics, and has provided a template for cosmological constraints (Komatsu and Seljak, 2001, 2002). The amplitude of the high-multi-pole portion ($2000 < \ell < 10000$) of the CMB angular power spectrum, C_ℓ, scales with the matter power spectrum normalization and baryon fraction as

$$C_\ell \propto \sigma_8^\gamma \left(\Omega_{\rm b} h\right)^2 , \tag{2.20}$$

where the power, γ, is large and varies with cosmology. A series of experiments within the last two years have measured a high-ℓ band of the CMB anisotropy spectrum in search of SZ distortions with varying constraints on σ_8. QuAD (Friedman et al., 2009), SZA (Sharp et al., 2010), and ACT (The ACT Collaboration, 2010) find values in accordance

with or near WMAP results (*i.e.,* $\sigma_8 \sim 0.80$), while Bolocam (Sayers et al., 2009) and APEX-SZ (Reichardt et al., 2009) just set upper limits of $\sigma_8 \leq 1.57$ and 1.18, respectively. SPT, on the other hand, finds lower values near $\sigma_8 \sim 0.78$ (Lueker et al., 2010). Each of these studies must model the expected secondary anisotropy of the thermal SZ power in order to remove it and obtain the primary CMB power. Although the assumption of the template in Eqn. 2.20 in modelling the SZ power does not significantly bias the results from these studies, a lax accounting of the intracluster gas distribution significantly imperils the cosmological constraints – beyond 2σ for the power spectrum normalization (Taburet et al., 2010). The impact of AGN feedback may be very important in the correct modeling of the SZ power spectra and could potentially bring the SPT constraints into alignment with those from CMB power measurements alone (Battaglia et al., 2010).

Hopes for cosmological investigations through the kinetic SZ take two avenues. First, the kinetic SZ effect may provide measurements of large-scale flows through cluster peculiar velocities (Ostriker and Vishniac, 1986b; Haehnelt and Tegmark, 1996; Holder, 2004) or can be used to identify clusters (Ostriker and Vishniac, 1986a). Recent simulation studies have focused on the application of the kinetic SZ effect in measuring the Epoch of Reionization (Zhang et al., 2004; Iliev et al., 2007). In particular, correlations with other markers, like neutral hydrogen, appear to have the highest potential for determining the rate of reionization independently of the CMB primary anisotropies (Jelić et al., 2003; Hernández-Monteagudo et al., 2006).

2.3.2 The $Y_{\rm tSZ} - M$ Relation

As seen in the power spectra, the scale of distortion is $\mathcal{O}(1')$ and arises from the Comptonizing cluster ICM. The bulk thermal SZ signature arises from the total distortion integrated over an aperture of about that scale; by summing over all lines of sight through the

aperture, two quantities can be determined:

$$Y_{\rm obs} = \int {\rm d}\Omega\, y \propto M^{5/3} d_{\rm A}^{-2} E^{2/3}(z) \tag{2.21}$$

$$Y_{\rm int} = \int {\rm d}A\, y \propto M^{5/3} E^{2/3}(z). \tag{2.22}$$

The first expression for the dimensionless, $Y_{\rm obs}$, is the observed SZ decrement projected along the entire line of sight through the cluster and within an angular aperture Ω, where d_A is the angular diameter distance. The second equation for $Y_{\rm int}$ is the *intrinsic* distortion when the cluster's position and extent (co-moving surface area, A) are known; this quantity is free of non-cluster line-of-sight projection effects. The approximation of the mass dependence in both expressions is derived under assumption of self-similarity, where $T \sim M^{2/3}$.

The earliest measurements of the $Y - M$ relation from SuZIE show good agreement with X-ray observations of the same clusters (Cooray, 1999), as well as evolution in accordance with self-similar expectations. Also, they first observed the lower scatter in the integrated flux, Y, at fixed mass, compared to that of the central decrement, y_0, which is highly susceptible to details of gas physics and merging events (Benson et al., 2004); this contrast is corroborated in simulations for multiple gas prescriptions (Motl et al., 2005). Recent models have evolved to embrace non-isothermality of the ICM (Liao et al., 2010; Chaudhuri and Majumdar, 2010) – for example, by incorporating a temperature profile (Hallman et al., 2006). The degree of scatter in the $Y - M$ relation is thought to be small for two reasons: first, the integration of the pressure all the way to the last scattering surface is likely to include diverse cross-sections of the cosmic web, smoothing out structures local to the cluster in question; second, the thermal SZ effect has a relatively weak dependence on the electron density, compared to X-ray emission. Much as in the case for the work by Markevitch (1998) with cool-core samples, scatter is reduced uniformly (by

80%) through the exclusion of *high*-substructure clusters in simulated samples (as demonstrated in simulations, Shaw et al., 2008). Moreover, in small-sample hydrodynamic cluster simulations, including the crucial elements of galaxy formation, Nagai (2006) find that a scatter of $10 - 15\%$ can be achieved, independent of gas physics – as long as the cluster volume included in the flux integration is sufficiently large (3-4r_{500}).

A slew of small-sample (≤ 40) measurements of evolution in scaling relations over the last three years range from de-evolution, to self-similar, to stronger than self-similar (*e.g.,* Menanteau et al., 2009; Marrone et al., 2009; Rines et al., 2010; Culverhouse et al., 2010; Andersson et al., 2010); the masses are derived from a variety of methods, from weak lensing, to galaxy velocities, to X-ray emission measures. Early hydrodynamic simulations including various levels of feedback and cooling display $Y - M$ relations that self-similarly evolve and display a tightness that implies the mass-limited potential of SZ surveys (White et al., 2002). More recent simulations with realistic feedback show a steeper $Y - M$ slope than expected with self-similarity; feedback tends to expel gas at a higher rate from low-mass clusters, thus depleting the electron density and the SZ flux (Sehgal et al., 2007). The details of the earlier simulation are not available, but the discrepancy suggests that the feedback was not strong enough, or was not incurred early enough in the simulation. Nevertheless, X-ray observations imply a steeper relation, in accordance with gas fractions increasing with cluster mass.

The typical method for these studies of evolution (see also §3.2) is to subdivide the survey sample into redshift intervals and then fit the scaling relation, $Y \sim M^{\alpha} E^{\beta}(z)$, for α and β, where β is then compared to the self-similar expectation of Eqn. 2.22. This type of analysis is susceptible to several points of confusion. The derived masses, as discussed in §2.2, are highly dependent on the gas model. Also, the covariance between the SZ, X-ray and optically derived signals that are inputs to these fitting studies has not yet been

constrained – nor has the scatter in Y at fixed mass. In Nord et al. (2008), we investigated the potential for confusion in the X-ray relation $L_{\rm X} - T_{\rm X}$ alone, and found that the intrinsic correlation, scatter, and survey selection work in tandem to obfuscate the true nature of the scaling relation evolution (see §3.2). A similar study regarding SZ and X-ray signals is warranted.

2.3.3 Cluster Counts and Astrophysical Contamination

SZ surveys have the potential to produce highly complete mass-limited samples of clusters throughout the age of the universe that will be useful for constraining the matter power spectrum, Dark Energy, and perhaps even non-Gaussianity (Holder et al., 2001; Benson et al., 2002; White, 2003; Roncarelli et al., 2010). SPT and ACT have recently begun taking data and discovered a few dozen clusters, with more soon to come (Staniszewski et al., 2009; Vanderlinde et al., 2010; Hincks et al., 2009; Menanteau et al., 2009). An alternative method has been pursued to search for SZ clusters in the WMAP five-year data, detecting a few SZ clusters with high significance, but relying on gas density models that are discordant with X-ray studies of the same clusters (Diego and Partridge, 2010). The lower mass-limits for SPT and ACT are 5×10^{14} and $8 \times 10^{14}\, h^{-1}$ $\mathrm{M}_{\odot}$, respectively, for near perfect completeness (Vanderlinde et al., 2010; Menanteau et al., 2009), but several early forecasts were slightly optimistic (*e.g.,* $1 - 2 \times 10^{14}\, h^{-1}$ $\mathrm{M}_{\odot}$; Sehgal et al., 2007; Pace et al., 2008).

Changes in the estimation of σ_8 and higher than expected observation noise account for the discrepancy between predictions of cluster counts and reality. However, there remain a few contamination factors that must be dealt with to maximize survey counts; they include line-of-sight filamentary gas, line-of-sight cluster-cluster overlap and sub-mm point sources. The confusion limit imposed by faint and diffuse sources of SZ signal is expected to be a challenge for modern surveys, principally inflicted on low-mass systems,

which have lower gas fractions and thus provide a lower signal-to-noise ratio (da Silva et al., 2001). Ultimately, "realistic" cluster models derived from hydrodynamic simulations will be necessary (Holder et al., 2007). In one such hydrodynamic simulation with AGN feedback and radiative cooling, Hallman et al. (2007b) found that clusters right near the mass limits of modern surveys obtain a median mass bias of $\sim 79\%$ due to projection, with $\sim 16\%$ coming from gas outside halos. Projection effects for line-of-sight overlap of clusters have been investigated in a semi-analytic effort, which found that high-mass halos ($\geq 2 \times 10^{14}\, h^{-1}\ \mathrm{M}_{\odot}$) are not signficantly contaminated (Ostriker et al., 2005; Bode et al., 2007; Shaw et al., 2008), but this model did not include extra-cluster filamentary gas that might be found in full hydronamic simulations.

White and Majumdar (2004) used an analytic model with realistic telescope parameters across a range of frequencies to determine that $1'$-resolution surveys will be "confusion limited." Sub-mm point sources fall into two categories – radio and infrared (IR). Radio sources are typified by the synchrotron emission of AGN, while dusty galaxies heated by recent star-formation principally comprise the IR sources. The exact distributions in number, brightness, and energy of small-scale sources are poorly constrained, but often considered to follow power-laws. Masking, as well as band-pass and high-pass filtering are the typical techniques for point-source removal (Tegmark and de Oliveira-Costa, 1998; Vale and White, 2005). The latest SPT results estimate the 2010 sample is affected by at most $\sim 10\%$ for dusty sources and $\sim 1\%$ for radio sources (Vanderlinde et al., 2010). A better understanding of gas physics and the cluster-point source correlation will provide the greatest boons to eliminating this contamination. Radio galaxies have potential to bias 20% of cluster decrements above $\sim 2.5 \times 10^{14}\, h^{-1}\ \mathrm{M}_{\odot}$ (*e.g.,* Sehgal et al., 2010).

2.4 Conclusions

Multi-wavelength imaging has been extended to include the radio for high-resolution studies of single clusters, as well as for lower-resolution, larger area studies. In the former scenario, clusters of varying levels of structure have been observed. Recently, the SZ effect was found in 1E 0657-56, the Bullet Cluster, with sub-arcminute resolution, revealing substantial substructure: the SZ peak was found on the opposite side of the cluster as the X-ray peak (Malu et al., 2010). An observation of the massive cluster CL J0152–1357 revealed a similar offset (Massardi et al., 2010). These imply significant differences in the pressure and gas emission distributions, with potential cosmological constraint implications. The angular diameter distance is the link to cosmology through the Hubble constant, but without proper modeling of cluster morphology, the cluster size will be biased.

Overlapping surveys are beginning to provide multi-wavelength data for large sets of clusters, as well (Menanteau et al., 2010; Vanderlinde et al., 2010). Since the next-generation X-ray all sky surveys will not occur for another one or two decades, the best opportunity for taking advantage of SZ survey completeness is to join them with optical surveys which can provide redshifts. However, SZ surveys are proving to be limited to high masses ($\geq 5 \times 10^{14}\, h^{-1}\ \mathrm{M}_{\odot}$); therefore, we will have to rely on ingenuity to probe further down the mass function. I anticipate that one of the best methods will be to stack SZ clusters based on a quantity from their optical counterparts, like richness. Li et al. (2010) have predicted the benefit of such an exercise, but it has yet to be realized in analyses of simulation or data.

The famed bullet cluster has been observed in at least three wavelength bands. To have multiple perspectives for each cluster is our ultimate goal, so that we might exploit each signal's strength to find the unified view of a galaxy cluster.

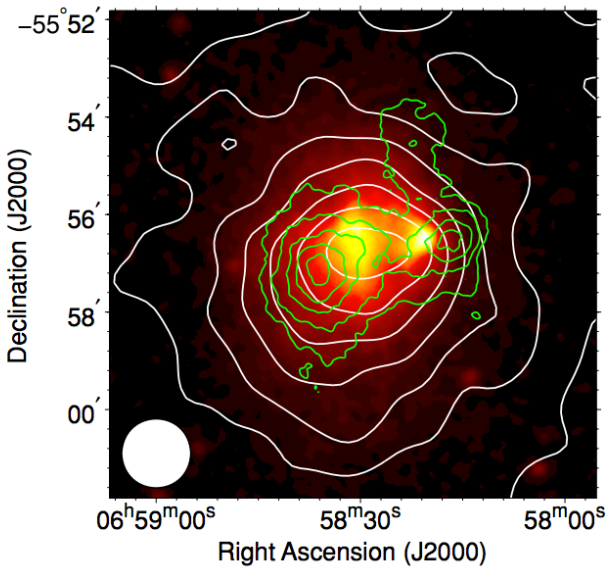

Figure 2.10: Cluster 1E 0657-56, the famed Bullet Cluster, observed in multiple wavelengths. The white, less-concentrated contours show the Sunyaev Zel'dovich signal; the green, more centrally concentrated contours show the weak lensing signal; and the underlying map is from an *XMM* survey (Halverson et al., 2009).

CHAPTER III

Galaxy Cluster Scaling Relations: Case Studies in Observational Biases and Multi-wavelength Correlations

Encoded within observed galaxy cluster populations are important keys to cosmic structure evolution. The decryption of these clues requires an accurate understanding of survey selection. The character of the cluster population selected on an observable signature, S, will depend strongly on how S relates to the underlying halo mass and how that relation varies over time. Below, we discuss a suite of studies in X-ray-selected populations of clusters to illustrate the effects of observational biases on cluster investigations, and to demonstrate the power of multi-variate analyses. Intrinsic cluster evolution, intrinsic scatter in a given mass or signal sample, and observational biases combine to effectively confuse the signal-mass connection and degenerate the information derivable from monochromatic and sparsely sampled cluster populations. We then discuss how this bias, in combination with the scatter of the population, obfuscates the true nature of the evolution in the X-ray $L - T$ plane (§3.2) – particularly in the absence of a constraint on the intrinsic correlation between the luminosity and temperature. With the onset of broader, deeper, more complete, and overlapping cluster surveys, multi-band data is becoming increasingly accessible. In §3.3, we discuss the power of multi-wavelength, multi-variate analyses for probing covariance in cluster populations.

To those ends, here we initiate a joint/multi-variate approach to scaling relation analysis, with a joint log-normal distribution of cluster signals,

$$\mathcal{P}(\mathbf{S}|\mu,z) = \frac{1}{(2\,\pi)^{n/2}\ |C|^{1/2}} \mathrm{e}^{-\boldsymbol{\delta}^T C^{-1} \boldsymbol{\delta}}, \qquad \boldsymbol{\delta} \equiv \begin{bmatrix} \delta_{S_1} \\ \delta_{S_2} \\ \vdots \\ \delta_{S_n} \end{bmatrix}, \tag{3.1}$$

where $\delta_{S_i} \equiv \left(S_i - \bar{S}_i\right)/\sigma_{S_i}$ is a normalized deviation in a given signal, S, with σ_{S_i} the variance in that signal; and C is the correlation matrix. This is similar to the probability used in Eqn. 1.32, except that mass and redshift have become the parameters here, because we are discussing observable signatures; given knowledge or assumption of prior distributions, the application of Bayes' theorem trivially leads to this re-casting. We have these signals in mind for this chapter

$$\mathbf{S} = \{N_{\rm gal}, T_{\rm X}, L_{\rm X}\}, \tag{3.2}$$

and we will refer to their logarithmic quantities frequently; we define their symbols with lower-case Greek letters, *e.g.,* $\mu \equiv \ln M$ (see Table 3.1). Note that, even though it is not the strict translation between English and Greek, we have used η as the proxy for the logarithm of richness, $\ln N_{\rm gal}$, for visual clarity.

Table 3.1: Logarithmic symbols for scaling relations

Physical Quantity	Logarithmic Quantity	Symbol
Mass, M	$\ln M$	μ
Luminosity, L	$\ln L$	ℓ
Temperature, T	$\ln T$	t
Richness, $N_{\rm gal}$	$\ln N_{\rm gal}$	η

3.1 Observational Biases and Mass Selection in X-ray Surveys

The first determination of the mass function from X-ray survey data alone was performed by Reiprich and Böhringer (2002), who also measure the $L - M$ relation from a

"highly complete" sample of X-ray bright clusters (*HIFLUGCS*, the HIghest X-ray FLUx Galaxy Cluster Sample), derived from the ROSAT All-Sky X-Ray Survey (RASS; Truemper, 1993; Voges et al., 1999). In the derivation of cluster masses from surface brightness observations, they assume that the gas is isothermal and in hydrostatic equilibrium, and they defer considerations of flux-limit-induced mass incompleteness to future work. The intrinsic scatter in their resulting $L - M$ relation is explained as central emission in excess of the isothermal β model; this relegates to the log-mass intrinsic scatter a maximum of $\sim$0.10, with a total dispersion in log-mass of 0.21.

Stanek et al. (2006) provide an update to the $L - M$ relation that is based on a likelihood analysis of number counts of the strongly flux-limited *REFLEX* cluster sample matched to halo counts from the Jenkins mass function (Jenkins et al., 2001). The signal-mass relation of interest acts as the intermediary between the observed and theoretical counts, allowing constraints on the slope, normalization and scatter of the relation. In the course of this analysis, we discover that survey flux limits incur a mass incompleteness in the halo sample, effecting a bias of about a factor of two in the $L - M$ normalization at low masses. Throughout the remainder of this chapter, Reiprich and Böhringer (2002) and Stanek et al. (2006) will be referred to as RB02 and S06, respectively.

In the following investigation, we discuss the implementation of a flux limit in the model of the $L - M$ relation, and the implications of the resulting Malmquist bias for survey counts and for discerning between cosmological models. Starting with a simple probability distribution of luminosities conditional upon halo mass (in this case, a reduction of Eqn. 3.1 to one dimension), we construct the mean luminosity in the context of a halo mass function and canonical X-ray survey flux limits.

Throughout this section, we assume the following conventions: L is a rest-frame, soft-energy band ($0.1 - 2.4$ keV) X-ray luminosity – such as that provided by RASS – in units

of $10^{44}\,\mathrm{erg\,s^{-1}}$ with $h = 0.7$ ($\mathrm{H_0} = 100\,h^{-1}\,\mathrm{km\,s^{-1}\,Mpc^{-1}}$); M is the mass within a sphere encompassing $200\rho_\mathrm{c}(z)$ in units of $10^{15}\,h^{-1}\,\mathrm{M_\odot}$. Note the difference in Hubble constant conventions for luminosity and mass. We use two distinct sets of cosmological parameters, which differ in the choice of the power spectrum normalization, but each is consistent with a concordance world model: $\Theta_\mathrm{A} = \{\Omega_\mathrm{m}, \Omega_\Lambda, \sigma_8\} = \{0.3, 0.7, 0.8\}$ and $\Theta_\mathrm{B} = \{0.3, 0.7, 0.9\}$; the former has a lower power spectrum normalization that is consistent with WMAP three-year data (Spergel et al., 2006), a fact which will manifest in general as a difference in the number of halos. We will alert the reader to which set is used at the time of implementation; the choice has no effect on the broad interpretation of results.

To begin, we assume that the soft-band X-ray luminosity of halos follows a uni-variate log-normal distribution, $\mathcal{P}(\ell|z,\mu)$, with variance, σ_ℓ, about a mean, $\bar{\ell}$, that varies with mass and epoch as

$$\bar{\ell}(\mu, z) = \ell_{15,0} + p\,\mu + s_\mathrm{e} \ln[E^2(z)], \tag{3.3}$$

where the power-law form is derived from combining Eqn. 2.7 and Eqn. 2.12). In Eqn. 3.3, the normalization, $\ell_{15,0} \equiv \ln L_{15,0}$, defines the present-epoch geometric mean luminosity at the scale of $10^{15}\,h^{-1}\ \mathrm{M_\odot}$; p is the mass-scaling slope; $s_\mathrm{e} = \{7/6, 0\}$ are the parameters for self-similar (SS) and no-evolution (NE) scenarios; and $E^2(z) \propto \rho_\mathrm{c}(z) = \Omega_\mathrm{m}(1+z)^3 + \Omega_\Lambda$ represents the Hubble parameter evolution for a flat metric (recall Eqn. 1.13). The scatter $\sigma_\ell = p\sigma_\mu$ is assumed to be constant and mass- and redshift-independent.

A survey's flux threshold, f, sets the redshift-dependent luminosity limit, $\ell_{min}(z,T) = \log[\,4\pi d_\mathrm{L}^2(z)\ f/K(z,T)]$, where $K(z,T)$ is a K-correction derived from *Xspec* runs (Arnaud, 1996), and d_L is the luminosity distance to the cluster. To convert rest-frame to observed soft-band ($0.5 - 2.0\,\mathrm{keV}$) flux, we multiply the former by a correction factor obtained from fitting the output of a $0.3\ \mathrm{Z_\odot}$ metallicity plasma model (from `mekal` Mewe et al., 1985,

1986). Specifically, we use $L_{\rm obs} = K(z, kT)\, L_{\rm rest}$ with

$$
\begin{aligned}
K(z, kT) &= 1 + z\,[\,K_1(kT) + K_2(kT)\,z\,] \\
K_1(kT) &= -0.209 + \log kT(1.18 - 0.39 \log kT) \\
K_2(kT) &= -0.098 + \log kT(-0.092 + 0.085 \log kT),
\end{aligned} \tag{3.4}
$$

and kT in keV. The fit is accurate to a few percent within $z = 2$.

3.1.1 Mass Selection and Malmquist Bias

By integrating the Gaussian distribution in luminosity with this lower luminosity limit, we can derive a mass selection (or window) function:

$$
W(\mu, z) = \int_{\ell_{min}}^{\infty} {\rm d}\ell\, \mathcal{P}(\ell|z, \mu) = \sqrt{\frac{\pi}{2}} {\rm erfc}(\Delta_{\ell,min}), \tag{3.5}
$$

where $\Delta_{\ell,min} \equiv \left[\ell_{min}(z, T) - \bar{\ell}(\mu, z)\right] / \sqrt{2}\sigma_\ell$, and the error function is a consequence of a finite limit on the integral over the Gaussian distribution. For non-negligible scatter, σ_ℓ, a sharp selection in luminosity maps to a smooth mass selection. We then employ this model in conjunction with the Jenkins mass function to calculate the impact of the flux limit on the number count:

$$
\frac{{\rm d}N_f(z)}{{\rm d}z} = \frac{1}{2} \frac{{\rm d}V(z)}{{\rm d}z} \int {\rm d}\mu\, n(\mu, z) {\rm erfc}\left[\ell_{min}(\mu, z)\right] \tag{3.6}
$$

represents the differential number of halos of mass e^μ –within a co-moving volume element, ${\rm d}V(z)$–whose luminosities satisfy the threshold, $\ell_{min}(z, T)$, and thus the flux limit.

Fig. 3.1 displays the window functions of current and next-generation X-ray surveys for mass scales of the Coma-cluster ($10^{15} h^{-1} M_\odot$, upper panel) and for halos near the limits of modern Sunyaev-Zel'dovich surveys ($10^{14} h^{-1} M_\odot$, lower panel; Holder and Carlstrom, 2001). We employ two canonical flux limits, 3×10^{-12} and $1 \times 10^{-14}\,{\rm ergs\,s^{-1}\,cm^{-2}}$, representative of the existing REFLEX survey and of future, or next-generation, surveys such

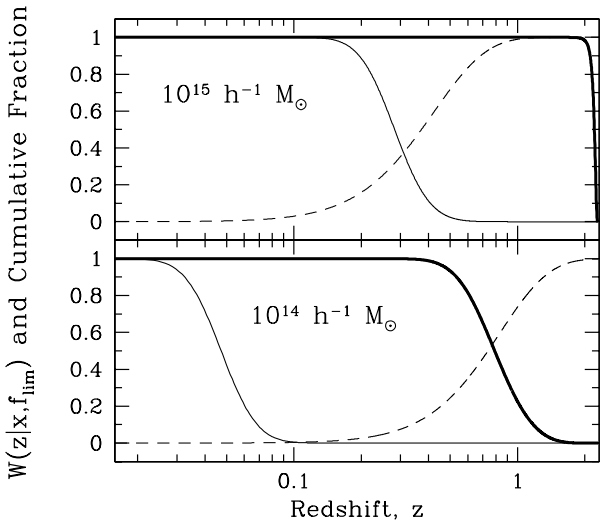

Figure 3.1: Window functions of current (solid) and next-generation (solid, bold) X-ray surveys are shown along with the cumulative fraction, $N(<z)/N_{\rm tot}$ (dashed), of *all* halos at $10^{15}\,h^{-1}{\rm M}_\odot$ (upper) and $10^{14}\,h^{-1}{\rm M}_\odot$ (lower).

as ChaMP[1] (Kim et al., 1a; Green et al., 1), the XMM-Newton serendipitous survey samples (AXIS; Carrera et al., 2007), and Spectrum X-Gamma.[2] For the $L-M$ relation, we employ the best-fit parameter values $p=1.6$, $\sigma_\ell=0.59$, and $\ell_{15,0}=1.81$, which are derived in S06, and a choice of $s_{\rm e}=1$, consistent with self-similar evolution in the soft X-ray band. We choose to operate within the low-normalization world model, $\Theta_{\rm A}$. Dashed lines in Fig. 3.1 show the cosmic cumulative fraction, $N(<z)/N_{\rm tot}$, of halos within redshift, z. For our chosen normalization $\sigma_8=0.8$, most $10^{15}\,h^{-1}{\rm M}_\odot$ halos lie within $z=1$, while the $10^{14}\,h^{-1}{\rm M}_\odot$ population continues growing to $z=2$. The next-generation window function allows detection of 100% of the $10^{15}\,h^{-1}{\rm M}_\odot$ halos in the sky. The decline in the window function at $z\sim0.5$ permits detection of $\sim56\%$ of the universal population at $10^{14}\,h^{-1}{\rm M}_\odot$.

[1]See http://hea-www.harvard.edu/CHAMP
[2]See http://hea-www.harvard.edu/SXG/sxg.shtml

By contrast, the shallow flux limits of current surveys detects only 34% and 0.06% of these totals, respectively.

Such incomplete mass sampling leads to a Malmquist bias that brightens the $L-M$ relation relative to the intrinsic (mass-limited) population. The log-mean luminosity in a flux-limited survey, as a function of mass and epoch, is

$$\begin{aligned} \ell(\mu,z) &= \int \mathrm{d}\ell\, \mathcal{P}(\ell|\mu,z)\ell \\ &= \frac{1}{2}\bar{\ell}(\mu,z)\,\mathrm{erfc}(\Delta_\ell) + \sqrt{\frac{1}{2\pi}}\sigma_\ell\, e^{-\Delta_\ell^2}, \end{aligned} \tag{3.7}$$

where $\Delta_\ell = \left(\ell - \bar{\ell}\right)/\sqrt{2}R\sigma_\ell$ The second term manifests the bias such that when $\ell_{\rm min}$ becomes negligible and W remains appreciable (*i.e.,* when the median luminosity is near the flux limit), the geometric mean is enhanced by an amount comparable to the scatter, σ_ℓ. The log-mean luminosity, $\langle\ell\rangle$, as function of mass, μ, for halos in the Universe in a flux-limited sample is

$$\langle\ell(\mu)\rangle = \frac{\int \mathrm{d}V(z)\, n(\mu,z)\, \ell(\mu,z)}{\int dN_f(\mu)}, \tag{3.8}$$

where $\mathrm{d}N_{\rm f}(\mu) = \frac{1}{2}\int \mathrm{d}V(z) n(\mu,z)\mathrm{erfc}(\Delta_\ell)$ is the differential number of halos that satisfy the flux limit as a function of mass.

We demonstrate the existence of this bias in real sky survey data and Monte Carlo simulations, in the context of a high-normalization cosmology – *i.e.,* $\Theta_{\rm A}$. Fig. 3.2 shows the HIFLUGCS data as open triangles, which lay systematically above $z=0$ best-fit SS model of the $L-M$ relation formulated in Eqn. 3.8. The model $L-M$ relation expected for the HIFLUGCS survey, with the ROSAT soft-band flux limit $2\times10^{-11}\mathrm{ergs\,s^{-1}cm^{-2}}$ is shown by the dashed line. The HIFLUGCS sample systematically selects brighter objects at fixed mass, leading to a brightening, by roughly a factor of 2, in the $L-M$ relation relative to the present-epoch relation, shown by the solid line. In addition to the analytic calculation, we also create a mock realization of the HIFLUGCS sample using the Hubble

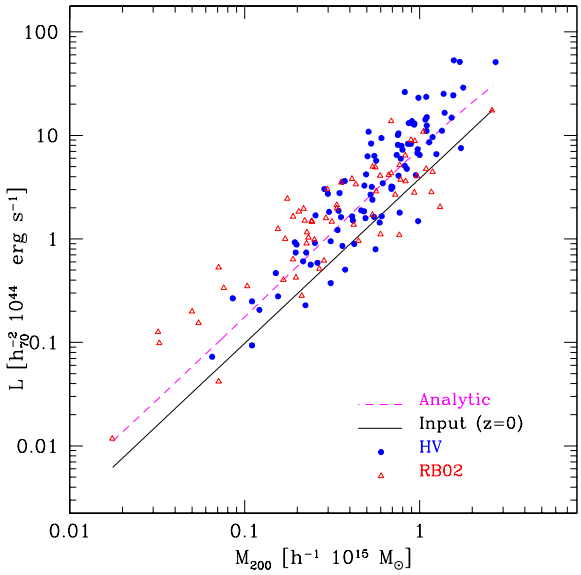

Figure 3.2: Best-fit SS model relation between rest-frame, soft X-ray luminosity and mass at $z = 0$ (solid line) compared to the relation expected from a HIFLUGCS flux-limited sample (dashed line), computed from Eqn. 3.7. Triangles show the HIFLUGCS data, while filled circles show an Hubble Volume (HV) mock version of these data.

Volume (HV) sky survey samples based on our best-fit models of the $L - M$ and $T - M$ relations. The result for one random realization is shown by filled circles in Fig. 3.2. The points scatter about the analytic expectation with *rms* deviation of $\sigma_\mu = 0.63$, close to the input (mass-limited) scatter of 0.59. Due to the finite size of the HIFLUGCS sample, the degree of bias varies from the analytic expectation. We estimate this variance using 200 Monte Carlo realizations of HV mock samples, derived from the MS and VS sky surveys (Evrard et al., 2002), adjusted to a sky area of 5.5 Sr to match the cluster counts in RB02. From this exercise, we derive correction terms of -0.70 ± 0.11 to $\ell_{15,0}$ and -0.06 ± 0.07 to p. The correction terms strongly depend on the degree of scatter in the $L - M$ relation.

The brightening for this high-flux sample results mostly from scatter and not from evolution in the SS model. Fig. 3.3 demonstrates this by comparing the increase, relative to $z = 0$, in log-mean luminosity, calculated for both SS and NE models. At low masses

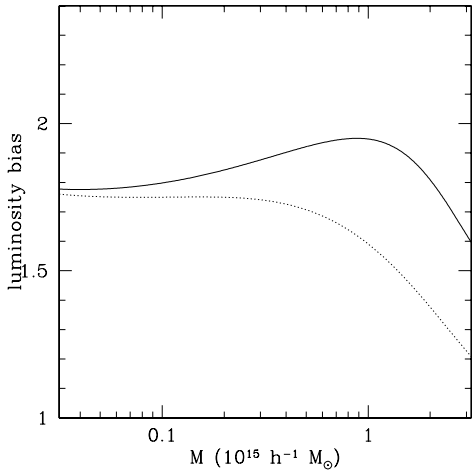

Figure 3.3: Ratio between the logarithmic mean luminosity (Eqn. 3.8) of a $1.7 \times 10^{-11}\,\mathrm{ergs\,s^{-1}cm^{-2}}$ flux-limited sample and the $z = 0$ relation (Eqn. 3.3) for the best-fit SS (solid line) and NE (dotted line) models. The difference in the two models is the result of redshift evolution, which is more important for higher mass halos that satisfy the sample flux limit at larger distances.

and luminosities, the volume probed is small, and there is little evolution in the SS model. Above $10^{14}h^{-1}$ $\mathrm{M}_\odot$, the survey depth approaches $z \sim 0.1$, and the SS model bias becomes larger than that of the NE model. As the survey probes to higher redshifts at higher masses, the SS model bias continues to grow up to $M \sim 10^{15}h^{-1}$ $\mathrm{M}_\odot$. Beyond this mass scale, the bias drops because the number of the most massive halos falls to zero at high redshift. A similar decline is seen in the NE model.

Fig. 3.4 compares the $L - M$ relation for shallow and deep flux-limited surveys to the underlying, mass-limited relation. To discern between the effects of survey selection and redshift evolution, we plot the *de-evolved* geometric mean, $\langle L/E^{2s_\mathrm{e}} \rangle$, using the model value, $s_\mathrm{e} = 1$. Samples with the shallow flux limit show a gradual deviation from a power law at the high-mass end. At extremely high masses (above $3 \times 10^{15}\,h^{-1}$ $\mathrm{M}_\odot$) the bias disappears as the sample becomes mass-complete. For the deeper flux limit, surveys become mass-complete above $2 \times 10^{14}\,h^{-1}$ $\mathrm{M}_\odot$ (see Fig. 3.1), and the resultant $L - M$ relation is unbiased above this mass scale. Here, we have assumed the low-normalization cosmology, Θ_B.

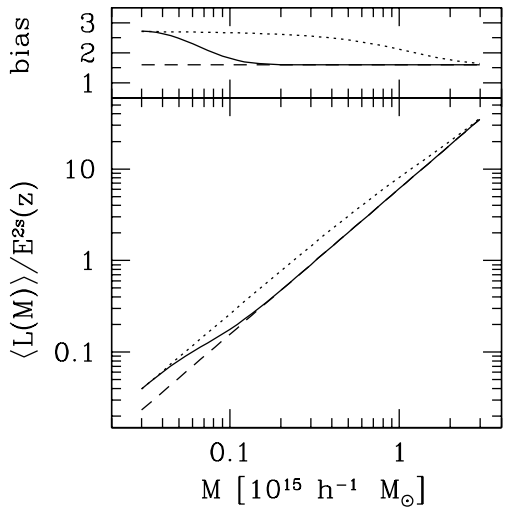

Figure 3.4: Geometric mean, $\langle L \rangle \equiv e^{\langle \ell \rangle}$, of the de-evolved luminosity for current (dotted) and next-generation (solid) flux-limited samples. The upper panel shows the bias relative to the underlying, mass-limited population (dashed). Since deep samples are mass-complete above $\sim 2 \times 10^{14}\, h^{-1}$ $M_\odot$, no luminosity bias is apparent above this mass. N.B., $s = s_e$.

The best-fit scaling parameters derived in the context of flux limits and non-negligible mass scatter differ substantially from those of RB02 principally due to the correction for the flux-cut bias. Previous analysis of the REFLEX cluster abundance and power spectrum (Schuecker and Böhringer, 2001, 2003) assumed a much smaller level of scatter ($\sigma_\ell \sim 0.2 - 0.3$), based on the impression that the main contribution to the L-M scatter derived in RB02 was large uncertainty in the binding mass measurement. Given the smaller mass, no Malmquist bias correction appeared necessary, so the value of $\ell_{15,0}$ used in the cosmological parameter derivation was higher, and the resulting value of the power spectrum normalization was lower, compared to the values used here.

3.1.2 Impact of Bias on Cosmological Parameter Estimation

The normalization of the luminosity-mass relation, $\ell_{15,0}$, the scatter in mass, σ_μ, and the power spectrum normalization, σ_8, interact strongly and co-determine the observed cluster number counts. We briefly discuss the interaction among these parameters by

looking at resulting scaling relation fits in different cosmologies. In S06, we perform the fit to the scaling relation for a suite of cosmologies, in which σ_8 and Ω_m are varied, such that $\sigma_8{\Omega_m}^2$ is held constant by varying the power spectrum normalization; this condition holds constant the number of halos above $\sim 2 \times 10^{14}$ $M_\odot$ (White et al., 1993a; Viana and Liddle, 1998).

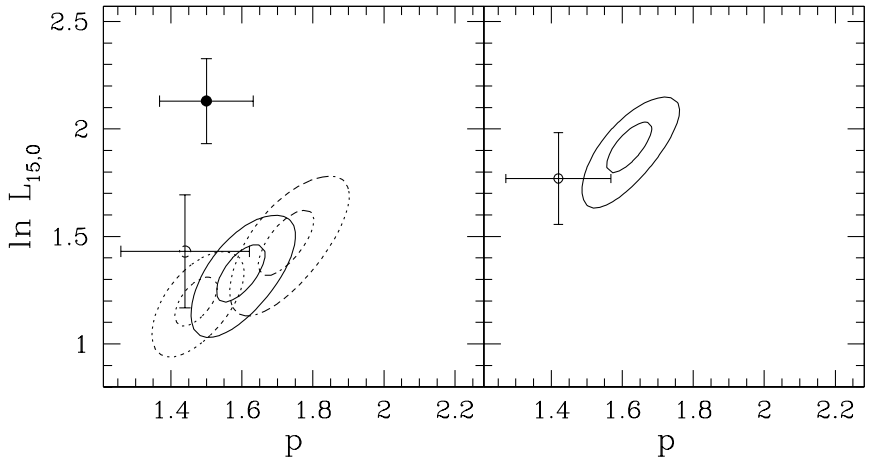

Figure 3.5: Left: The 68% and 99% intervals of the slope and normalization for Ω_m =0.24,0.3, and 0.36 (left to right), with $\Omega_m\sigma_8^2$ constant, and after applying the joint constraints on counts, clustering, and σ_μ scatter. The filled circle in the left panel plots the original RB02 result, with 90% error bars. Right: the 68% and 99% confidence intervals of the slope and normalization for the WMAP compromise cosmology, $\Omega_m = 0.24$ and $\sigma_8 = 0.85$ – after applying the joint constraints on counts, clustering, and a lower $\sigma_\mu = 0.25$ scatter. In both panels, the open circle gives the RB02 result after correcting for the flux-cut bias, with 90% error bars that include the variance of HV Monte Carlo realizations.

Fig. 3.5 displays the results of this analysis, including the effect of the flux-limit bias. In the left panel, each set of contours shows the 68% and 99% confidence intervals in the best-fit slope and normalization; the centers of the contour shift rightward and upward as Ω_m is increased. As the slope of the mass function steepens, driven by the increase in the matter density, the best-fit value of p must also increase so that more low-mass halos may appear as bright as what is observed. A change in the power spectrum normalization shifts

the mass function almost constantly for all space densities in the mass direction; and the mass, M_*, at fixed space density, n_*, has been shown to scale with the normalization as $M_* \propto \sigma_8^{1/\alpha}$ for high-mass halos ($> 5 \times 10^{14}$ $M_\odot$. Again, the luminosity is held fixed at fixed space density by observations: therefore, as σ_8 (and thus M_*) vary, one can compensate by changing the best-fit characteristic luminosity, $\ell_{15,0}$, as seen in Fig. 3.5. The closed and open dots show the fit result from RB02 in its original form, and as corrected for the flux-limit bias, respectively. The error bars are enlarged by adding in quadrature the scatter in the corrections that were derived in the HV Monte Carlo analysis.

To provide reference to contemporary data, in the right panel of Fig. 3.5, we assume a world model inspired by WMAP3 (Spergel et al., 2006): $\Omega_{\rm m} = 0.24$, $\sigma_8 = 0.85$, and a lower initial estimate of the scatter, $\sigma_\mu = 0.25 \pm 0.06$. The open circle shows the RB02 best-fit parameter corrected for the flux-cut bias. The Malmquist bias correction for the $L - M$ relation is thus robust to variations in cosmology.

3.2 Evolution, Scatter, and Covariance in Scaling Relations

Although efforts to understand cluster covariance will ultimately be pan-chromatic, this section focuses on the behavior of two bulk X-ray properties—luminosity, L, and temperature, T—derived from observations of flux-limited samples. In particular, we investigate how the form and evolution of the $L - T$ relation depend on assumptions regarding the covariance in these observables with mass.

Self-similar evolution of the type envisaged by Kaiser (1986) has been tested with several observational samples, including those drawn from surveys from ASCA (Mushotzky and Scharf, 1997; Novicki et al., 2002), XMM-Newton (Vikhlinin et al., 2002; Kotov and Vikhlinin, 2005), CHANDRA (Lumb et al., 2004), and ROSAT (Fairley et al., 2000; Maughan et al., 2006). Several investigations of X-ray evolution have compared $L - T$

relations among low- and high- redshift populations; results range from somewhat stronger than self-similar scaling to slightly negative. Early work by Mushotzky and Scharf (1997), Fairley et al. (2000), and Novicki et al. (2002) find trends that are consistent with no evolution ($s_e = 0$) to $z \sim 0.8$. A recent study by Maughan et al. (2006) compares the WARPS (Scharf et al., 1997) subsample with data from Arnaud and Evrard (1999) and Vikhlinin et al. (2002) to probe conventional and modified forms of self-similar evolution. The $L - T$ slopes of differing redshift populations are found to be consistent among all the samples, and slightly *steeper* than the self-similar model. In a sample of 10 clusters at $z > 0.4$, Kotov and Vikhlinin (2005) measure evolution somewhat steeper than, but consistent with, self-similarity. Lumb et al. (2004) report near-self-similar evolution, and acknowledge the possibility of a flux-limit bias in their eight-cluster sample at $0.45 < z < 0.62$.

Balogh et al. (2006) compare observations with analytic models of the ICM, finding that the degree of evolution in the scaling relations depends strongly on that of the $L - M$ scatter. S06 determine the redshift-independent $\sigma_{\mu|\ell}$ in the presence of a flux-limit; they also note that simulations suggest a weak intrinsic correlation of the deviations in luminosity and temperature at fixed mass.

The work presented here addresses a potential source of confusion for such studies. Shallow flux-limited surveys are mass-incomplete, while samples derived from deeper flux-limited samples become complete at sufficiently high masses. This difference in selection, essentially a redshift-dependent Malmquist bias, manifests effects similar to genuine population evolution. We develop formalism in §3.2.1 for studies of correlated observable properties by introducing intrinsic covariance within a joint distribution of luminosity and temperature. Second, we address the role of covariance in the study of scaling relation evolution (§3.2.1).

3.2.1 $L-T$ and Correlation

We next incorporate covariance into scaling relation analysis. After computing observables under a multi-variate Gaussian model, we add an explicit demonstration of the model using halos from the HV sky survey catalogues (Evrard et al., 2002). Our aim is to demonstrate the interplay between covariance and scaling relation parameters for flux-limited samples.

Joint Luminosity-Temperature Distribution

To calculate the geometric mean and dispersion of the $L-T$ relation, we begin with a power-law scaling of the temperature with mass and the normalized Hubble constant – *i.e.,* $T \propto M^q E^{s_{\mathrm{e},T}}(z)$, where q is some integer, and $s_{\mathrm{e},T}$ is the evolution parameter. We assume that the log-mean temperature of the intracluster medium takes on a virial scaling behavior with mass (similar to Eqn. 2.7):

$$\bar{t} = t_{15} + \frac{2}{3}\mu + \frac{1}{3}\ln[E^2(z)], \tag{3.9}$$

where the normalization is $t_{15} = \ln(kT_{15})$ and $kT_{15} = 6.8$ keV. We further assume that there is constant log-normal scatter about the mean with $\sigma_t = 0.10$, equivalent to a 15% dispersion in mass at fixed temperature.

Using the normalized deviations, $\delta_\ell \equiv \left(\ell - \bar{\ell}\right)/\sigma_\ell$ and $\delta_\mathrm{t} \equiv \left(t - \bar{t}\right)/\sigma_\mathrm{t}$, we form the joint log-normal distribution of luminosity and temperature at a given mass and epoch,

$$\mathcal{P}(\ell, t|\mu, z) = \frac{1}{2\,\pi\,R}\mathrm{e}^{-\boldsymbol{\delta}^T C^{-1}\boldsymbol{\delta}}, \qquad \boldsymbol{\delta} \equiv \begin{bmatrix} \delta_\ell \\ \\ \delta_\mathrm{t} \end{bmatrix}, \tag{3.10}$$

where $C_{ij} \equiv \langle \delta_i \delta_j \rangle$ is the correlation matrix with off-diagonal elements equal to the correlation coefficient, $r \equiv \langle \delta_\ell \delta_t \rangle$, and $R \equiv \sqrt{1-r^2}$. The ξ^{th} moment of the distribution at

fixed temperature is

$$\langle \ell^{\xi}(t) \rangle = \frac{\int \mathrm{d}V(z) \int \mathrm{d}\mu \, n(\mu, z) \, \mathrm{e}^{-\delta_t^2/2} \mathcal{L}^{(\xi)}(t|\mu, z)}{\int \mathrm{d}N_f(t)} \tag{3.11}$$

$$\mathcal{L}^{(\xi)}(t|\mu, z) = \int \mathrm{d}\ell \, \ell^{\xi} \, \mathcal{P}(\ell, t|z, \mu), \tag{3.12}$$

where $\mathrm{d}N_{\mathrm{f}}(t) = \mathrm{d}V(z)\mathrm{d}\mu \, n(\mu, z) W(\mu, z) \mathrm{e}^{-\delta_t^2/2}$. The first moment (*i.e.,* the geometric mean luminosity) is

$$\mathcal{L}^{(1)}(t|\mu, z) = W(\mu, z) \, \hat{\ell} + \sigma_{\ell} R \, \mathrm{e}^{-\Delta^2_{\ell|\mathrm{t}}}, \tag{3.13}$$

where $\hat{\ell} \equiv \bar{\ell}(\mu, z) + r \, \sigma_{\ell} \, \delta_t$, $\Delta_{\ell|t} = \left(\ell - \hat{\ell} \right) / \sqrt{2} R \sigma_{\ell}$, and $W(\mu, z)$ is the window function of Eqn. 3.5. At a given mass, non-zero correlation effectively shifts the mean luminosity, either enhancing or suppressing the probability that a halo of given mass survives the flux cut. This has important implications in the counts and mean masses discussed below. In the no-correlation limit ($r = 0$), Eqn.'s (3.12) and (3.13) reduce to Eqn. (3.8), but convolved with a temperature-selection filter. From the $L - T$ distribution's second moment,

$$\mathcal{L}^{(2)}(t|\mu, z) = W(\mu, z) \left(\hat{\ell}^2 - R^2 \sigma_{\ell}^2 \right) + e^{-\Delta^2_{\ell|t}} \left(2 \, R \, \sigma_{\ell} \, \hat{\ell} + \sqrt{2} R^2 \sigma_{\ell}^2 \, \Delta_{\ell|t} \right), \tag{3.14}$$

we compute the observable variance, $\sigma_{\ell}^2 = \langle \ell^2 \rangle - \langle \ell \rangle^2$.

In Fig. 3.6, we show the expected $L - T$ relation mean and dispersion for REFLEX flux-limited clusters assuming three degrees of $L - T$ correlation, $r \in (-0.7, 0.0, 0.7)$. Points in the figure represent explicit realizations of the model derived from HV sky survey samples of massive halos above $5 \times 10^{13} \, h^{-1} \, \mathrm{M}_{\odot}$. Using redshifts and masses of an all-sky survey, we assign luminosities and temperatures via Eqn.'s 3.3 and 3.9, using two independent random Gaussian deviates, g_1 and g_2: g_1 controls the luminosity, and $g_t = r \, g_1 + R \, g_2$ sets the temperature. We then apply a flux limit including K-correction terms (the same as those used in Eqn.'s 3.5).

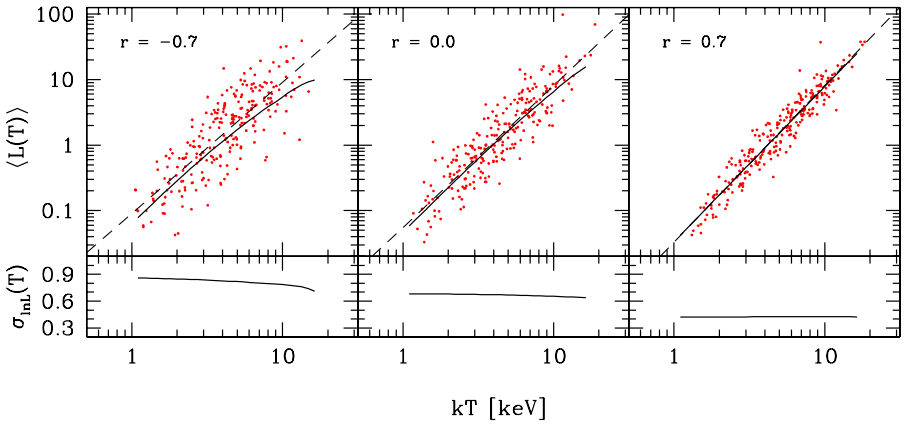

Figure 3.6: The X-ray luminosity–temperature relation ($L-T$, upper panels) and its dispersion ($\sigma_\ell(T)$, lower panels) expected for current, flux-limited (3×10^{-12} erg s^{-1} cm^{-2}) samples and for different correlation coefficients, $r=(-0.7,0.0,0.7)$. Solid lines show the analytic expectations, points show discrete realizations from HV full-sky halo realizations, and dashed lines are power-law fits to these discrete samples.

Similar to the flux-limited $L-M$ relation (Fig. 3.4), the $L-T$ relation deviates from a pure power-law, although this deviation is extremely weak for values, $r \gtrsim 0.5$. The scatter depends strongly on the correlation coefficient, with magnitude varying from 0.8 to 0.4 as r varies from -0.7 to 0.7. Anti-correlation causes scatter orthogonal to the mean input relation, enhancing the magnitude of the observable dispersion. Positive correlation reduces this dispersion.

Markevitch (1998) fit a power-law to a population of low-redshift clusters, uncorrected for cool cores. The resulting prediction of the soft-band X-ray luminosity, $L_{\mathrm{X},[0.1,2.4]} = 1.6\pm0.2\times10^{44}\,\mathrm{erg\,s^{-1}}$, for a 4 keV cluster lies slightly nearer to our models with *non-negative* correlation.

Gas dynamic simulations show weakly positive correlation, $r\sim0.2$ (S06), but the sensitivity of this result to physical treatment of the gas is unclear. Comparison of the model predictions to the growing body of $L-T$ observational data should yield constraints on the correlation, but we defer that exercise to future work. We turn next to observable

features at high redshift that next generation X-ray samples will provide.

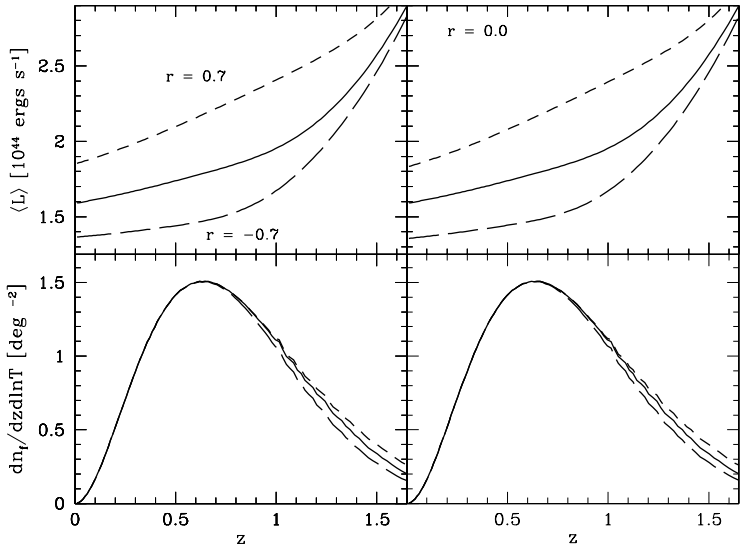

Figure 3.7: Redshift behavior of the geometric mean luminosity (upper), and the sky surface density (lower) of 4 keV clusters above a next-generation survey flux limit (10^{-14} erg s^{-1} cm^{-2}). The solid line in all panels is our default model ($s_{\rm e} = 1$, $\sigma_\ell = 0.59$, $\ell_{15,0} = 1.81$, $r = 0$). The left panels vary the correlation coefficient, $r = 0.7$ (short-dashed), and $r = -0.7$ (long-dashed), otherwise retaining the default model parameters. The right panels hold $r = 0$ and show the effects of changing the evolution and scatter: $s_{\rm e} = 0.95$, $\sigma_\ell = 0.72$, $\ell_{15,0} = 1.65$ (long-dashed); and $s_{\rm e} = 1.1$, $\sigma_\ell = 0.35$, $\ell_{15,0} = 1.95$ (short-dashed).

Evolution Diagnostics

For mass-complete samples, the mean $L - T$ relation will behave as $L \propto T^{3p/2} \rho_{\rm c}(z)^{s-p/2}$, where p is the luminosity-mass scaling, and $s_{\rm e}$ is the scaling with the normalized Hubble constant; $p = 4/3$ and $s_{\rm e} = 7/6$ recovers the self-similar, virial expectation of Eqn. 2.12. For a flux-limited sample, the geometric mean soft-band luminosity at fixed temperature is

$$\langle \ell(z) | t \rangle = \frac{\int {\rm d}\mu \, n(z,\mu) \int {\rm d}\ell \, \ell \, \mathcal{P}(\ell | z, \mu, t)}{\int {\rm d}n_f(z|t)}, \tag{3.15}$$

where ${\rm d}n_f(z|t) = {\rm d}\mu \, n(\mu, z) W(\mu, z) {\rm e}^{-\delta_t^2/2}$. The luminosity in Eqn. (3.15) and the sky surface density, $(4\pi)^{-1} {\rm d}V(z)/{\rm d}z {\rm d}n_f(z|t)$, are shown in Fig. 3.7 for the case of $kT = 4$ keV

clusters selected with a next-generation (10^{-14} erg s^{-1} cm^{-2}) flux limit.

The left panels show models with different $L-T$ correlation within our default model with $(s_{\rm e}, \sigma_\ell, \ell_{15,0}) = (1.0, 0.59, 1.81)$. The survey is mass-complete at 4 keV out to $z \sim 0.7$, independent of r, giving counts that are identical in this redshift range. The mean luminosities shift from the mass-limited mean by an amount $r\,\sigma_\ell \langle \delta_t \rangle$, where $\langle \delta_t \rangle$ is the mean temperature deviation of the selected sample. For halos of fixed temperature, the steepness of the mass function implies that $\langle \delta_t \rangle > 0$; there are more low-mass halos to scatter upward into the temperature bin than high-mass halos to scatter downward. This effect either brightens or dims the mean luminosity at low redshifts, depending on the sign of the correlation, r. At $z \gtrsim 0.7$, the differences in 4 keV mass selection among the models become appreciable. Compared to the $r = 0$ case, this selection effect drives the counts up and the mean masses down for the $r = 0.7$ model, and vice-versa for $r = -0.7$. The magnitude of this mass shift is small, however, amounting to -3% and $+6\%$ at $z = 1.5$, respectively.

The right panels of Fig. 3.7 show two zero correlation models tuned to produce behavior similar to the $r = \pm 0.7$ cases. The parameter sets, $(s_{\rm e}, \sigma_\ell, \ell_{15,0}) = (1.10, 0.35, 1.95)$ and $(0.95, 0.72, 1.65)$, are within the 95% error contours that result from the REFLEX analysis of S06. The solid line reproduces our default model, as in the left panels, where $r = 0$. The luminosity moments and sky surface densities of these models lie within a few percent of the respective covariance models shown in the left panels, but the driving mechanisms are different. The dimmer intercept and larger scatter of the $s_{\rm e} = 0.95$ case force this model to become mass-incomplete earlier than the default case. The counts drop beyond $z \gtrsim 0.7$ and the mean luminosity rises as the Malmquist bias is triggered. The $s_{\rm e} = 1.10$ case, with a smaller scatter and higher intercept, remains mass-complete to a higher redshift, leading to larger counts and a smaller Malmquist bias.

Unlike the $r = \pm 0.7$ case, the mean halo mass selected by the 4 keV constraint is not shifted at high redshift in these models. When $r = 0$, halos that scatter up or down into a fixed temperature bin are equally likely to be culled by the sample flux limit. Mass estimates from weak lensing of stacked ensembles could potentially be a useful discriminatory diagnostic, but systematic effects must be controlled at the one-percent level at $z \simeq 1$. The upside is that next-generation surveys will produce large numbers of high-z clusters. According to Fig. 3.7, a 5000-deg^2, deep-flux limit survey will yield 445 clusters with temperatures between 3.8 and 4.2 keV, and between 0.9 and 1.1 in redshift.

3.3 Multi-wavelength Scaling Relations

The earliest X-ray-Optical cross-correlation studies of clusters focus on the $L_{\rm X} - L_{\rm opt}$ relation. Although they potentially suffer from non-uniform selection of the cluster sample (Miller et al., 1999; Donahue et al., 2001), they indicate positive power laws down to moderate luminosities ($\sim 10^{42}$ and $\sim 10^{44}$, in the X-ray and optical, respectively). Constraints on the $L_{\rm X} - L_{\rm opt}$ scatter (~ 0.2, orthogonal) have been found to be highly sensitive to the observation band and cluster size as measured by the optical data when simple linear regression on the data is used (Popesso et al., 2004). Stacking RASS clusters in richness bins has the potential to reduce dispersion incurred by variation in cluster size (Dai et al., 2007; Rykoff et al., 2008). Sufficiently resolved X-ray images allow one to probe the intracluster gas for reliable signatures of substructure (Buote and Tsai, 1995; Ventimiglia et al., 2008; Böhringer et al., 2010). Low-richness clusters are often those undergoing evolution and are not yet relaxed. Given the low signal-to-noise nature of clusters with a high degree of substructure, the study of internal cluster dynamics is a natural candidate for a cross-calibration exercise (Lopes et al., 2009).

In the next case, we extend the multi-variate analysis across wavebands to probe the

relationship between the X-ray and optical signals. The present discussion, based on the work in Rykoff et al. (2008), seeks to to illustrate the potential of a multi-variate, multi-*wavelength* analysis of scaling relations. In brief, X-ray luminosities and weak lensing signals are derived from stacked sets of clusters discovered in independent serendipitous surveys in overlapping sky regions. Below, we describe the essentials of the input data sets, the stacking procedures and, finally, the $L - M$ correlation and consequences for future studies.

The input optical data are galaxies from the Sloan Digital Sky Survey (SDSS: York et al., 2000), and the clusters discovered via the maxBCG algorithm (Koester et al., 2007). The cluster sample is nearly volume-limited between redshifts 0.1 and 0.3, with high purity and completeness for clusters above richnesses of 10 galaxies. The richness estimator N_{200} is defined as the number of members on the E/S0 ridge-line, brighter than $0.4L_*$ in i band and contained within r_{200} of the cluster center (Hansen et al., 2005; Johnston et al., 2007). Weak lensing masses are derived from projected surface density contrasts about stacked cluster centers (Sheldon et al., 2009), which are inverted with a probabilistic mass model that includes mis-centering, an NFW profile (Navarro et al., 1997), and large-scale clustering (Johnston et al., 2007).

The ROSAT All-Sky Survey (RASS), which was described in §3.1, is the origin for the X-ray catalogue used here. The low exposure time for RASS ($\sim 400s$) gives dim clusters, so they must be stacked to achieve sufficient signal-to-noise for a detection. With brightest cluster galaxies as their centers, the clusters are stacked on N_{200} (and L_{200} for a cross-check) within apertures scaled to $z = 0.25$. K-corrections are used to shift the soft-band emission to the rest frame at that epoch. Combining the stacked luminosities $\langle L_{\rm X}|N_{200}\rangle$ and weak lensing masses $\langle M_{200}|N_{200}\rangle$, we find

$$\langle L_{\rm X}|N_{200}\rangle = 12.6^{+1.4}_{-1.3}\left(\frac{\langle M_{200}|N_{200}\rangle}{10^{14}h^{-1}\ {\rm M}_\odot}\right)^{1.65\pm1.3} 10^{42}\ {\rm erg\,s^{-1}}, \tag{3.16}$$

which is shown in Fig. 3.8, along with from S06 and RB02. The independent analysis

methods generally agree on the $L - M$ scaling.

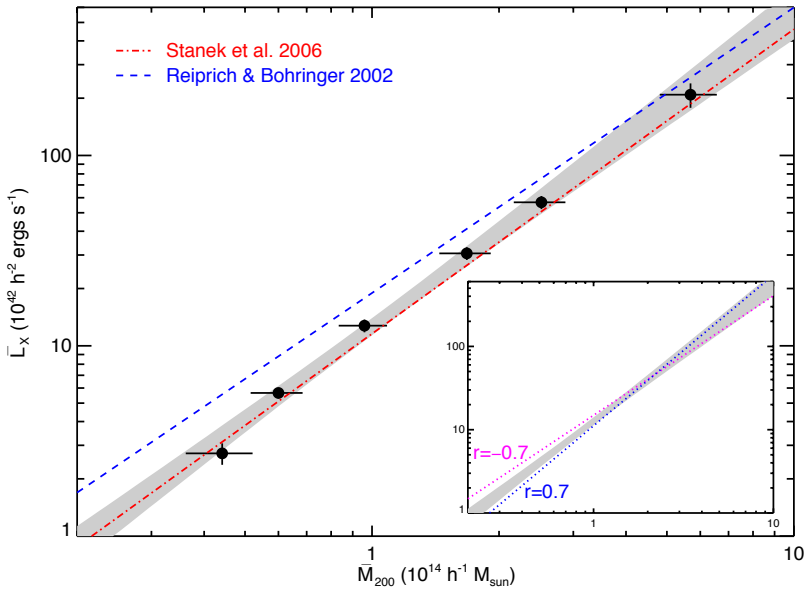

Figure 3.8: Points show maxBCG-RASS (algebraic) mean L_X and M_{200} values found by binning on N_{200} (solid circles) or L_{200} (empty circles). The dark gray band represents the ± 1 contours on the best-fitting relations using the N_{200} bins. The dot-dashed line shows the S06 relation, while the dashed line shows the S06 fit to the HIFLUGCS clusters from RB02 based on hydrostatic masses. Both relations have been scaled assuming self-similar evolution. The error bar in the legend shows the typical 1σ systematic error in the SDSS lensing masses, representing an overall shift in normalization that is possible in the maxBCG-RASS relation. The inset plot indicates the effects on the slope due to covariance, r, between L_X and N_{200} at a fixed mass. If L_X and N_{200} data at a fixed mass are correlated (r=0.7), this will bias the slope steeper, and if they are anti-correlated, this will bias the slope shallower.

Next, we discuss the sensitivity of cross-band scaling relations to covariance between the mass proxies. This sensitivity is not restricted to multi-wavelength studies, but is well illustrated by simple considerations in this particular study. Starting again with Eqn. 3.1, we set the bivariates to the X-ray luminosity, L_X, and cluster richness, N_{200}, and define the correlation coefficient in consistent fashion – $r \equiv \langle \delta_\ell \delta_\eta \rangle$, where $\ell \equiv \ln L_X$ and $\eta \equiv \ln N_{200}$.

We can construct the total probability of all the variables in terms of two signals conditional on the third: $P(\ell, \eta, \mu) = P(\ell, \eta|\mu)P(\mu)$; it is traditional in theoretical studies

(*i.e.,* investigations of the halo occupation distribution) to treat the mass as the condition. However, the combined maxBCG-RASS clusters are binned by richness, the $L_{\rm X} - N_{200}$. With Bayes' theorem and the number density function of halos approximated as a power law, $n(\mu) \equiv {\rm d}n/{\rm d}\mu \sim {\rm e}^{-\alpha\mu}$, we reformulate the conditional probability as $P(\ell, \mu|\eta)$. We then marginalize over the luminosity to obtain the mean mass as a function of richness, $\bar{\mu}(\eta) = \bar{\mu}_0(\eta) - \alpha\sigma^2_{\mu|\eta}$.

To probe the luminosity-richness covariance, however, we calculate the mean luminosity as a function of richness,

$$\bar{\ell}(\mu) = p\left[\bar{\mu}(\eta) + \alpha r \sigma_{\mu|\eta}\,\sigma_{\mu|\ell}\right], \tag{3.17}$$

and the variance

$$\sigma^2_{\ell|\eta} = p^2\left[\sigma^2_{\mu|\eta} + \sigma^2_{\mu|\ell} - 2r\sigma_{\mu|\eta}\sigma_{\mu|\ell}\right], \tag{3.18}$$

where p is the same slope of the $L - M$ relation used throughout this chapter. From the equations, we read off the effects of X-ray-richness covariance. First, at null correlation, the luminosity scales with the mean mass. However, for $r \neq 0$, the mass function slope α moves the mean luminosity by the same amount independent of the richness, but only if the mass function is truly scale free. When the slope is a function of the mass itself, as for cold Dark Matter, the relative bias in the slope p is proportional to the derivative of the mass function slope.

To illustrate this interaction, we apply richnesses and luminosities to Dark Matter halos in the Hubble Volume Simulation for a particular case of potential fit parameters ($p = 1.6$, $\sigma_{\mu|\ell} = 0.25$, and $\sigma_{\mu|\eta}$). The mock-up of this Monte Carlo sample is performed in the same fashion as the original analysis: X-ray luminosities are stacked in richness bins. As in Nord et al. (2008), we explore both negative and positive correlation ($r = \pm 0.7$), which tilts the

luminosity-mass slope by ~ 0.2, as shown in Fig. 3.8; this gives scaling relations that are all consistent with those found in the above study.

Next, consider the dependence of the scatter in luminosity at fixed richness on the covariance of Eqn. 3.18. It was constrained in Rykoff et al. (2008) to be $\sigma_{\ell|\eta} = 086 \pm 0.03$, and in the current model it takes values 1.1, 0.90, and 0.72 for $r = -0.7$, 0.0 and0.7, respectively. It also depends on the scatter in mass at fixed richness, which we assumed to be smaller than that inferred from velocities in Becker et al. (2007). Using the scatter value from that study results $\sigma_{\ell|\eta} > 1$, in contradiction with Rykoff et al. (2008). Either Becker et al. (2007) overestimated the scatter or the log-normal assumption must be revisited.

3.4 Discussion and Conclusion

The multivariate properties of massive halos selected by X-ray flux-limited surveys are sensitive to assumptions about the correlation between bulk observable properties at fixed mass. Using a model in which the $L - M$ relation is tuned to match local REFLEX counts, we show how the Malmquist bias in mean luminosity (which arises from mass-incompleteness) disappears during the transition from shallow to deep flux-limited samples. Although the underlying model is based on power-law behavior, the geometric mean $L - M$ relation from a flux-limited sample will deviate from a pure power-law, with a kink at the mass scale above which the survey becomes mass-complete. For a survey with a flux limit, 10^{-14} erg s^{-1} cm^{-2}, this feature is expected to lie near $M = 2 \times 10^{14}\, h^{-1}$ M$_\odot$.

Using a model with Gaussian covariance to describe how L and T jointly relate to mass and redshift, we compute luminosity moments and sky counts of clusters at fixed X-ray temperature. The slope and scatter of the $L - T$ relation for bright, local samples is sensitive to the covariance between these properties. Placing limits on the covariance from local samples will require prior information on the intrinsic L and T variance at fixed

mass, and such priors can be obtained from external observations or from gas dynamic simulations.

Finally, we address attempts to extract information on cluster evolution from the behaviour of the $L-T$ relation within a flux-limited survey. We show that non-zero $L-T$ covariance affects counts and luminosity moments as a function of redshift in a manner that is degenerate with redshift evolution at zero covariance.

A deep X-ray survey of clusters, by itself, is limited to the information provided by counts and luminosity moments. Combining such a sample with optical and sub-millimeter observations offers the potential to break the evolution-covariance degeneracies through lensing-mass estimates and additional signatures that can be computed via extensions to the approach introduced in this chapter. Such an exploration has been carried out for clusters stacked on optical richness, where the mean luminosities and weak lensing masses in each bin are correlated. The resulting scaling relation is in very good agreement with results from other independent methods.

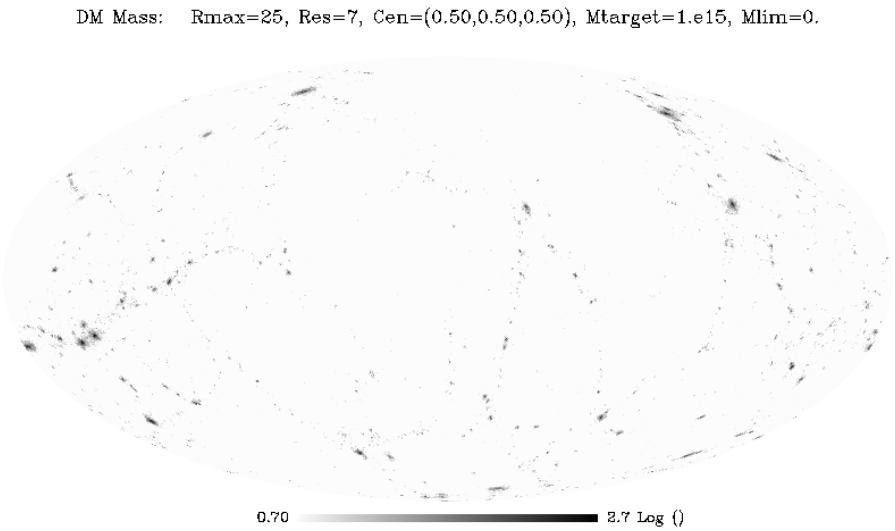

Figure 3.9: Projected Dark Matter mass surface density on the sky surrounding a high-mass ($10^{15}\,h^{-1}$ $M_\odot$) halo found in the Millennium Gas Simulation. The intensity is log-scale and the maximum distance for including particles is $25\,h^{-1}$Mpc (co-moving).

A potentially large lever arm on the commingling biases and confusion discussed above is an investigation of cluster projection and substructure. Both of these sources of contamination (or information) should inform the spatial definition of a cluster, and thus how its bulk properties are measured; this consideration draws into question the assumption of log-normal scatter in a signal at fixed mass. To promote a visual sense of projection

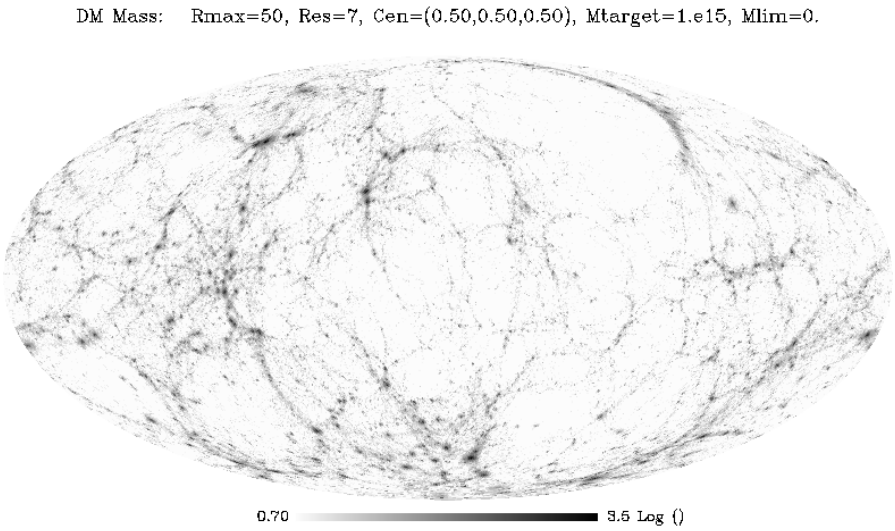

Figure 3.10: Same as Fig. 3.9, but with a maximum distance of $50\,h^{-1}$Mpc (co-moving).

effects, we give examples in Fig.'s (3.9) and (3.10). The intensity represents the log-mass surface density of dark matter surrounding a particular halo in the Millennium Gas Simulation (MGS; Gazzola and Pearce, 2006), within $25h^{-1}$Mpc and $50h^{-1}$Mpc (co-moving), respectively. Projection for this very massive halo ($\sim 10^{15}h^{-1}$ $M_\odot$) is non-negligible, and correctly modeling it is important for future cluster-finders (Cohn et al., 2007).

CHAPTER IV

The Millennium Gas Simulation Virtual Sky Survey: Construction and Diagnostic Tests

The first simulation of gravitating bodies was performed with light bulbs in place of galaxies (Holmberg, 1941). N-body simulation methods have since evolved the capacity to incorporate many scales of time and distance, and many different physical processes; today's cosmological simulations have billions of particles and probe scales from single galaxies up through the Hubble volume. Algorithms may be differentiated into two classes: Eulerian grid codes include the sub-class of 'Adaptive Mesh Refinement' techniques (*e.g.,* Enzo; Bryan et al., 2001), while Lagrangian codes track fluid elements and include the sub-class of 'Smoothed-Particle Hydrodynamics' (*e.g.,* GADGET; Springel et al., 2000; Springel, 2005). Precise hydrodynamic codes are necessary for reproducing both the ICM and the process of galaxy formation; we refer the reader to comparison studies of these codes (Frenk et al., 1999; O'Shea et al., 2005) for more information. Although the ICM has not yet been modelled perfectly, faithful reproduction of galaxy formation from first principles has proved more elusive, primarily due to the difficulty of including multi-scale physics (Evrard, 2000). Rather than directly simulating all processes required to form a galaxy, alternative approaches use proxies for individual processes within N-body simulations; or they add galaxies to dark matter lightcones after they have been created.

Simulations are useful not only for obtaining a complete view of large-scale structure;

future cosmological constraints will rely on simulated observations: we must test the robustness of the connections drawn between observations and the underlying matter distribution. To this end, we focus on virtual sky surveys constructed from simulated lightcones, which have a pedigree over two decades long (spanned by, Park and Gott, 1991; Evrard et al., 2002; Hallman et al., 2007b). Along with particle and halo lightcones, virtual sky maps are critical for testing observing and source-detection methods. In preparation for modern surveys, the simulation of SZ sky maps has received increasing attention over the last five years (Pires et al., 2006; Schäfer et al., 2006; Juin et al., 2007; Sehgal et al., 2010). Halo lightcones, combined with sky maps of varying degrees of observational noise, form a virtual sky survey.

The primary aim of this chapter is to discuss the construction of the Millennium Gas Simulation Virtual Sky Survey (MGSVSS) and to evaluate the fidelity of the galaxy populations and SZ properties against theoretical and phenomenological expectations. We discuss the production of particle and halo lightcones and virtual sky maps in the SZ. This chapter sets the stage for the multi-signal cluster-finding work in Chapter V.

4.1 General Description of the MGS

The results shown in this work are derived from analysis of the Millennium Gas Simulation (MGS; Gazzola and Pearce, 2006; Hartley et al., 2007; Stanek et al., 2009, 2010) – a GADGET-2-driven replica of the Millennium Simulation (Springel et al., 2005), in which half of the one billion particles are treated as gas particles and subject to hydrodynamics as well as gravity. Both simulations have cubic volumes of dimension $500\,h^{-1}\,\mathrm{Mpc}$ (co-moving), and the cosmological parameters are set to $\Omega_\mathrm{m} = 0.25,\ \Omega_\mathrm{b} = 0.045,\ \Omega_\mathrm{DE} = 0.75,\ h = 0.73,\ \sigma_8 = 0.9$, and $n = 1$. The Dark Matter particles and gas particles have masses of $1.422\,10^{10}\ \mathrm{M}_\odot\,h^{-1}$ and $3.120\,10^{9}\ \mathrm{M}_\odot\,h^{-1}$, respectively.

The MGS begins at redshift, $z = 49$, with snapshots of the simulation taken at logarithmically spaced intervals, resulting in 160 outputs. The gas prescription features a "pre-heating" of the proto-ICM at redshift, $z = 4$, where each gas particle receives an entropy injection of $S = 200\,\mathrm{keV\,cm^{-2}}$. The time and magnitude of entropy injection are set to reproduce the observed $L_\mathrm{X} - T_\mathrm{X}$ at the present epoch. In addition to preheating, the simulation includes radiative cooling of the gas, with the metallicity set at a constant value of $0.3\,\mathrm{Z_\odot}$, similar to that observed within the intra-cluster medium (Sarazin, 1986). The effect of the pre-heating in this simulation is so extreme as to prevent any star formation since $z \sim 4$.

From the full-box simulation, we create particle lightcones out to redshift $z \approx 2$ by interpolating particle properties between snapshots. The lightcones subtend $100\mathrm{deg}^2$ on the virtual sky. We use a spherical overdensity halo finder to identify halos within critical density, $\Delta = 200$: potential halo centers are first identified by ranking the local density of each dark matter particle. These densities are inversely proportional to the distance, R_NN, of a particle to its Nth nearest neighbor. We then measure total masses, gas fractions and SZ decrements for all halos.

4.2 Lightcone Construction

Next, we discuss the construction of the lightcone. There exist several methods for simulating cosmological lightcones. The most basic method involves a simple stacking of redshift slices taken from full three-dimensional cosmic volumes (*e.g.,* Cohn et al., 2007; Cohn and White, 2009). They can also be built on the fly while the full three-dimensional simulation is running (*e.g.,* Hallman et al., 2007b). Finally, particles can be interpolated between redshift slices for a more accurate 'stacking' of snapshots (Evrard et al., 2002), which is the method we use for MGSVSS.

An observer at the present epoch, t_0, receives photons from an earlier epoch, t, after they have traversed a co-moving distance, $r(t)$ (recall Eqn. 1.14). The observer's past light cone (see the solid, blue line in Fig. 4.1) are comprised of events that lie on the continuous set of concentric co-moving spheres of radius, r, leading back to the earlier epoch. This lightcone from redshift, $z = 0$ to $z_{max} = 2$, reaches to co-moving distance, $r_{lc,max} \sim 3h^{-1}\,\mathrm{Gpc}$; and it must be selected from the original simulation volume – a cube of side-length, $500h^{-1}\,\mathrm{Mpc}$ (co-moving) – which evolves through discrete snapshots in time back to z_{max}. Below, we describe this selection. In the discrete environment of the N-

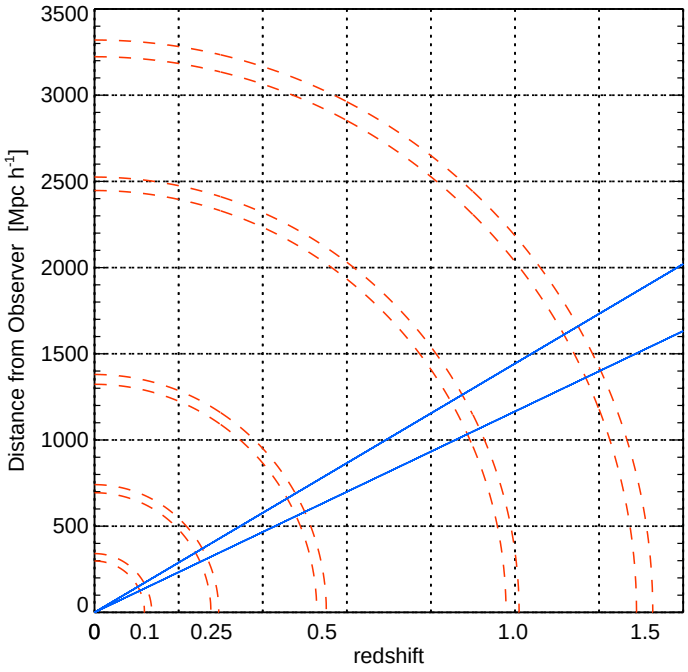

Figure 4.1: A cartesian view of the MGSVSS, within simulation volumes of side-length, $l_{\mathrm{box}} = 500\,h^{-1}\mathrm{Mpc}$ (demarcated by dotted lines). The lightcone of the MGSVSS, with the observer at the origin, intersects a full volume of many times the MGS volume and is demarcated by solid (blue) lines. Consecutive spherical shells are shown as dashed (red) arcs. The vertical axis shows the co-moving distance, and the horizontal axis shows redshift.

body simulation, the same particles are saved in consecutive time steps. First, we select the same spherical shells of finite co-moving thickness within the simulation (the small region

between red, dashed lines in Fig. 4.1) at consecutive snapshots; that is, in each shell, we obtain the same particles at two different time steps. Within these shells the particle's trajectory and the lightcone intersect. The inner and outer radii receive small buffers to ensure the acquisition of high-speed particles, whose peculiar motion could take them out of a shell during a time step.

To obtain the particle properties on the lightcone as they intersect with particle trajectories within the snapshot pair, we employ a linear interpolation, similar to Evrard et al. (2002). A particle's position relative to the observer is $\mathbf{x}_i$ at one time step and $\mathbf{x}_{i+1} = \mathbf{x}_i + \Delta\mathbf{x}$ at the next time step. The interpolated position, $\mathbf{x} = \mathbf{x}_i + \alpha\Delta\mathbf{x}_i$, is between those two points, where α is the interpolation parameter,

$$\alpha \equiv \frac{r^2(t_i) - x^2(i)}{2\left[\mathbf{x}_i \cdot \Delta\mathbf{x} + r(t_i)\Delta r\right]}, \tag{4.1}$$

the spherical vector location magnitude is $|\mathbf{x}| \equiv r(t_i + \alpha\Delta t)$; and the change in position between snapshots is always positive – *i.e.,* $\Delta r \equiv r(t_i) - r(t_{i+1}) > 0$.

The MGS volume has side-length, $500h^{-1}\,\mathrm{Mpc}$ in co-moving coordinates (equivalent to a redshift, $z \sim 0.2$). To reach beyond the local universe to higher redshifts, we take advantage of the periodic boundaries of the simulation: we scale particle positions by a multiple of a side-length, when the particle's redshift exceeds that of the distance within the co-moving volume. For example, consider a particle on the lightcone of Fig. 4.1 at redshift, $z = 0.3$; it must also be at the appropriate co-moving distance which is beyond the side-length of the original simulation cube. Therefore, we shift the x-coordinate of the particle in the $z = 0.3$-snapshot of the original volume by one side-length. A potential concern in replicating simulation volumes is the replication of large-scale structure. For example, a lightcone lying horizontal along the x-axis would acquire the same particles that are found at redshift, $z = 0.25$, would be found again at redshift $z = 1.5$ (see Fig. 4.1), as well as at many points in between. We have chosen a sufficiently small survey area and

a declination angle such that replications will be as small as possible. (Kitzbichler and White, 2007).

4.3 Particle Diagnostics: Measurement of Interpolation Error

We next assess the errors in particle properties that is incurred during the interpolation process by carrying out our method in a cartesian, rather than spherical, geometry (*i.e.,* $\alpha \rightarrow 0.5$). In this test, a target snapshot, $s_{\rm targ}$, is taken to provide true values of particle properties. We interpolate between two snapshots, $s_{\rm targ} - {\rm d}s$ and $s_{\rm targ} + {\rm d}s$. The resulting interpolated values can be compared to values at the target snapshot, giving mean deviations and variances on those deviations.

Table 4.1: Interpolation error in position and velocity for the particle subsample of $\sim 2.5 \times 10^8$ at redshift, $z \sim 0$.

ds	Time (Δt) $[\Delta t / t_{\rm hub}]$	$\sigma_{r,{\rm DM}}$ $[h^{-1}\,{\rm Mpc}]$	$\sigma_{v,{\rm DM}}$ [km/s]	$\sigma_{r,{\rm gas}}$ $[h^{-1}\,{\rm Mpc}]$	$\sigma_{v,{\rm gas}}$ [km/s]
1	0.0123	0.002	12	0.001	11
2	0.0257	0.007	38	0.002	24
3	0.0391	0.014	71	0.004	32
4	0.0514	0.023	105	0.007	39

The results from the interpolation of position and velocity for 2.5×10^8 particles near redshift $z \sim 0.05$ are shown in Table 4.1. The *rms* errors, σ, in position and velocity deviations increase with the snapshot interval, ds: at larger intervals, the true trajectory has received more perturbations and modifications than what is found through linear interpolation. Also, the magnitude of the errors for the gas particles is much lower than that of the dark matter, because gas particles typically reside in much sparser environments than the dark matter and receive fewer perturbations. The simulation's force-softening length is a distance added to the distance between particles when calculating gravitational potential, in order to prevent the potential from becoming unbound; this sets an effec-

tive level of precision for particle positions in a simulation. Even for the largest snapshot interval, the *rms* errors are well within the simulation's force-softening length (for MGS, $l_{\rm s} = 2.50 \times 10^{-2}\, h^{-1}\,{\rm Mpc}$); thus, errors due to interpolation will remain unresolved.

Table 4.2: Interpolation error in position and velocity of the Hubble Volume simulation at low redshift

ds	Time (Δt) [$t_{\rm hub}$]	$\sigma_{r,{\rm DM}}$ [$h^{-1}\,{\rm Mpc}$]	$\sigma_{v,{\rm DM}}$ [km/s]
1	0.003	0.0001	0.37
2	0.006	0.0003	1.41
3	0.011	0.0011	5.19
4	0.022	0.0042	17.9

It is also instructive to compare the results from MGS with those of a similar study on an unpublished simulation, the softening length of which is $\sim 5.0 \times 10^{-2}\, h^{-1}\,{\rm Mpc}$; the results of that study are shown in Table 4.2. For the appropriate comparison, see the shaded regions: they show the snapshot intervals of nearly equivalent time, Δt. At each snapshot interval, the errors in the MGS are generally about a factor of 2 higher than those for the Hubble Volume. The higher force and mass resolutions of MGS allow its particle trajectories to experience more forces in a similar amount of time as the Hubble Volume, allowing their velocities to be modified more frequently. The size of rms errors

Table 4.3: Interpolation error for the nearest neighbor distance of dark matter particles, and density and gas energy of gas particles, based on the interpolation of the test particle subsample at redshift, $z \sim 0$.

ds	Time (Δt) [$\Delta t/t_{\rm hub}$]	$\sigma_{R_{\rm NN},{\rm DM}}$ [$h^{-1}\,{\rm Mpc}$]	$\sigma_{u,{\rm gas}}$ [keV]	$\sigma_{\rho,{\rm gas}}$ [$\rho/\langle\rho\rangle$]
1	0.0123	0.003	0.00859	0.0133
2	0.0257	0.006	0.0183	0.0246
3	0.0391	0.009	0.0262	0.0336
4	0.0514	0.011	0.0332	0.0429

on the nearest neighbor distances, $R_{\rm NN}$, are similar to the dark matter position errors, but

scale more weakly with increasing snapshot interval (see Table 4.3). We will discuss later the dynamical quantities of the gas as a function of the local density, which will be more informative than global measures.

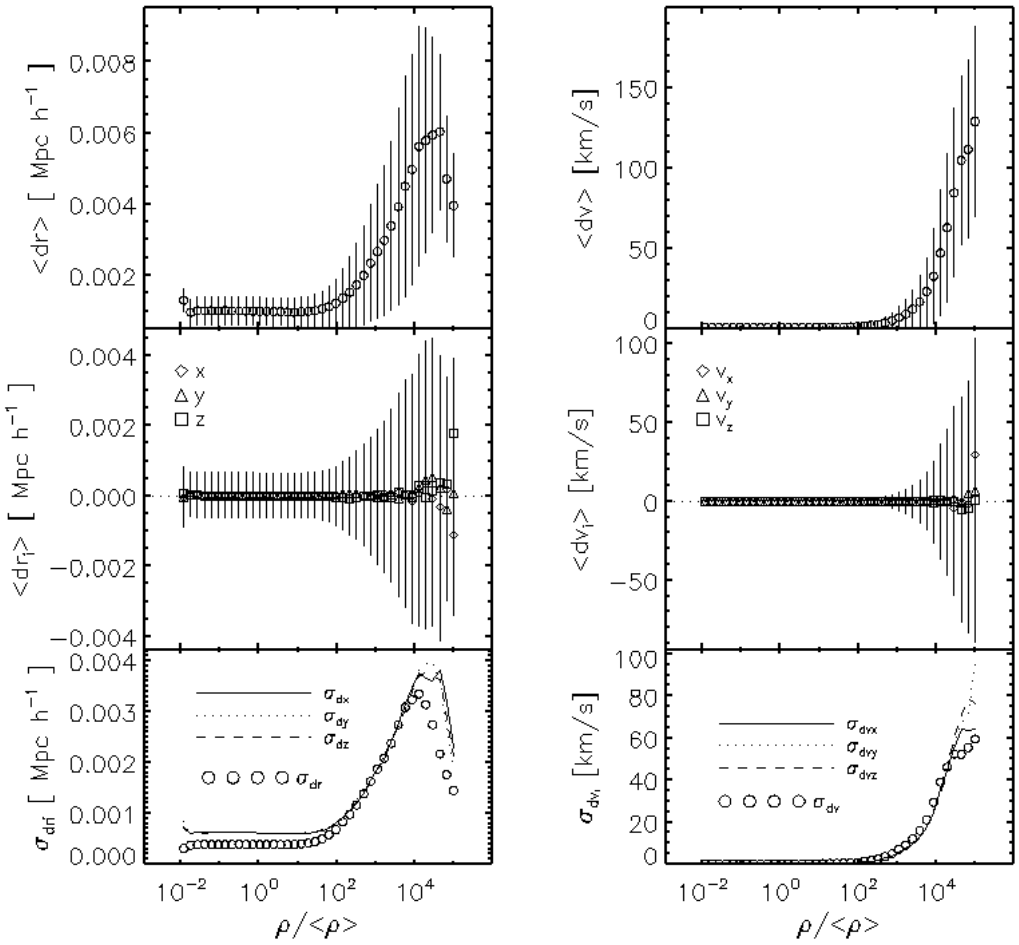

Figure 4.2: Interpolation errors in the position (velocity) of dark matter particles at redshift, $z \sim 0$, for an interpolation interval, $\mathrm{d}s = 1$, and binned by local density; the local density is normalized to the mean density of the current epoch and that particle species (*i.e.,* $\rho/\langle\rho\rangle$). The top panel shows the *mean deviation* in the three-dimensional position, $\langle \mathrm{d}r \rangle$, (velocity, $\langle \mathrm{d}v \rangle$). The middle panel shows the mean deviations in position (velocity) for each cartesian coordinate, $\mathrm{d}r_i$ ($\mathrm{d}v_i$). The bottom panels show the error in the mean position, $\sigma_{\mathrm{d}r_i}$, (velocity, $\sigma_{\mathrm{d}v_i}$) for both the three-dimensional quantity and the individual cartesian coordinates. The errors in the mean are shown as error bars in the top two panels.

We next look at the errors in interpolated quantities binned by local density. In general, mean deviations between the interpolated position and the true value in the target snapshot (*e.g.,* $\langle \mathrm{d}r \rangle \equiv \langle r_{\mathrm{targ}} - r_{\mathrm{interp}} \rangle$), as well as errors on the mean (*e.g.,* $\sigma_{\mathrm{d}r}$), increase as a function

of local density: particles interact more often in high-density environments, and are thus likely to have their trajectories perturbed. We show the mean errors and errors on the mean for dark matter and gas kinematics in Fig.'s 4.2 and 4.3 at redshift $z \sim 0$ for snapshot interval of $\mathrm{d}s = 1$. The densities are normalized to the mean cosmic density of the epoch for each particle type.

For the dark matter particles, the mean errors in position rise to a maximum of $\sim 6\,h^{-1}\,\mathrm{kpc}$, while the cartesian coordinates scatter about zero (even at the highest densities); and the errors on the mean deviation are as high as $\sim 3\,h^{-1}\,\mathrm{kpc}$. The gas particles behave similarly, with mean deviations as large as $3\,h^{-1}\,\mathrm{kpc}$ and errors on the mean as high as $\sim 2.5\,h^{-1}\,\mathrm{kpc}$. The mean deviations in velocity are $\sim 140\,\mathrm{km\,s^{-1}}$ and $\sim 80\,\mathrm{km\,s^{-1}}$ for dark matter and gas, respectively. The radial velocity errors may have a strong impact on kinetic Sunyaev-Zel'dovich measurements, especially in the presence of astrophysical contaminants, like the CMB (recall §2.3). Note that the maximum overdensity for gas is much less than that for the dark matter particles – 10^3 compared to 10^4, respectively; a direct comparison is shown in Fig. 4.4. Note the point at which the errors in the mean begin to increase for dark matter: overdensities of $\sim 10^2\,(\rho/\langle\rho\rangle)$ mark the scale at which the dark matter halos become well-defined (*i.e.,* $\Delta = 200$; recall §1.4).

Next, we briefly consider the errors in dynamical quantities. For dark matter particles, we show errors in the density, which is derived from the nearest-neighbor distance, in Fig. 4.5 (top, left panel). The mean density error is normalized to the mean dark matter density at that epoch ($\langle \mathrm{d}\rho\rangle/\langle\rho\rangle$). The mean fractional error in the density is defined as $f_\rho = \mathrm{d}\rho/\rho_{true}$ – the fractional difference between the interpolated density and the true density of the particle at the target snapshot; each fractional quantity from here on is defined in an analogous way. In the highest density regions, the fractional error in the mean density can be as much as 50%. The absolute mean error of the R_{NN} interpolation

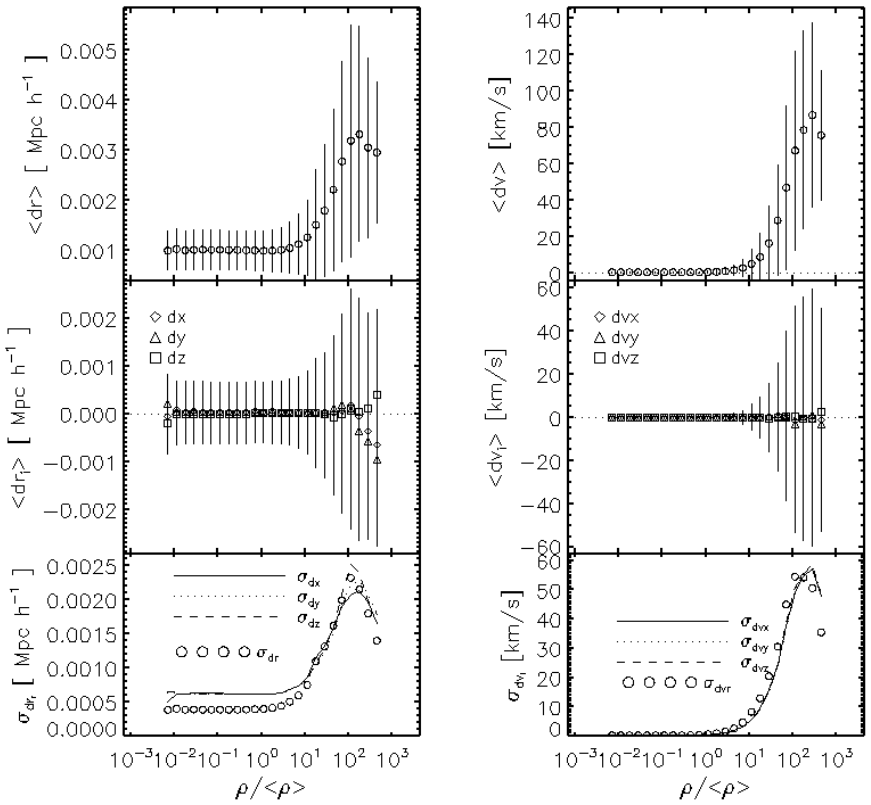

Figure 4.3: Same as Fig. 4.2, but for *gas* particles.

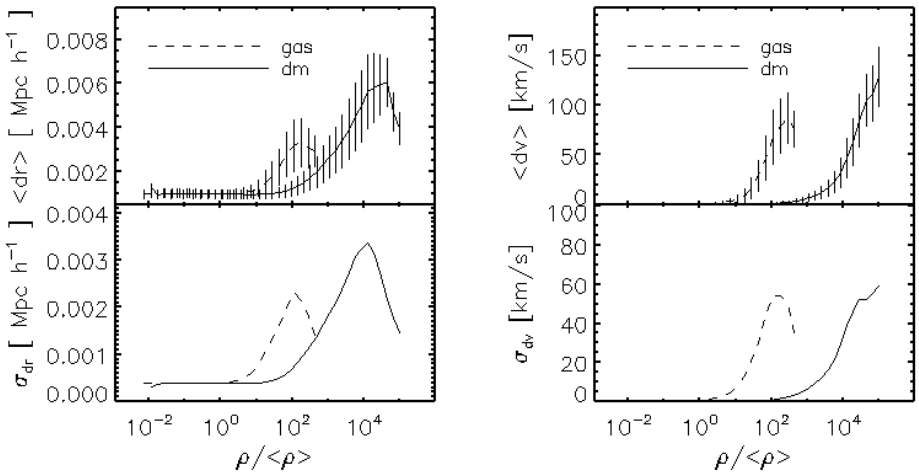

Figure 4.4: Comparison of interpolation errors in the position and velocity between gas (dashed curves) and dark matter particles (solid curves) for an interpolation interval, $ds = 1$, at redshift, $z \sim 0$. Error bars in the top panels are 0.5σ.

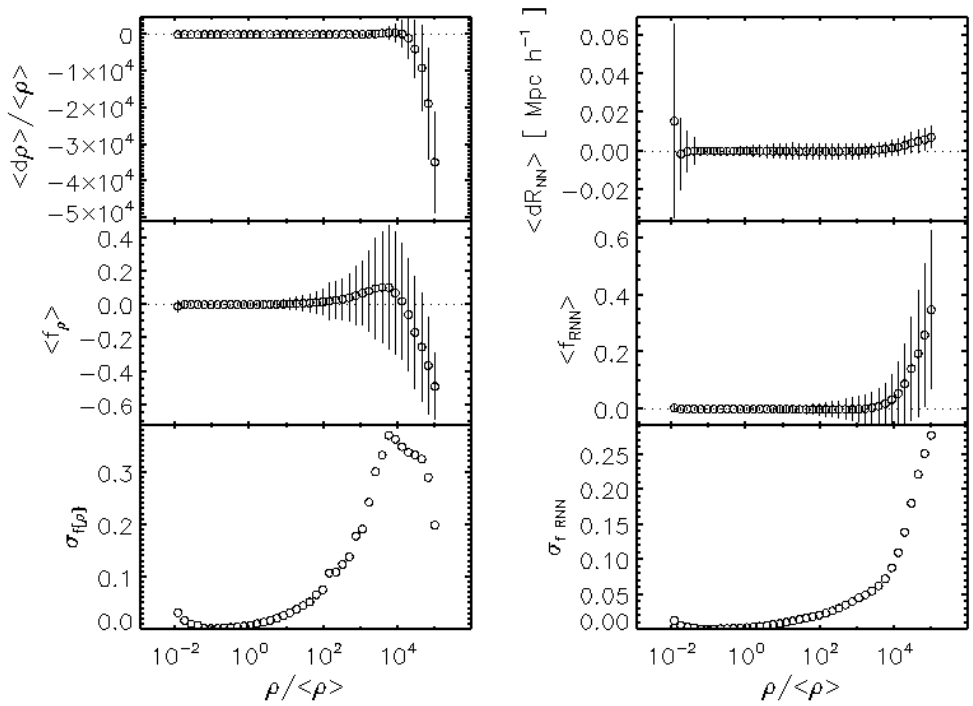

Figure 4.5: Interpolation error in the the nearest neighbor distance, $R_{\rm NN}$ (local density, ρ) of dark matter particles at redshift, $z \sim 0$. The top panel shows the mean error in density (nearest-neighbor distance). The middle panels show the mean fractional error in the density (nearest-neighbor distance). The bottom panel shows the error in the mean of the fractional density (nearest-neighbor distance).

can be as large as $\sim 15\,h^{-1}\,$kpc at the highest densities, and the mean fractional error can be as large as $\sim$40%. These errors occur near the centers of massive halos, the exact locations of which actually need not be identified within $25\,h^{-1}\,$kpc; for halo-finding, we only need to determine that there is a large overdensity centered near there. The errors drop to 5% in the mean fractional density error (and near 0% in $R_{\rm NN}$) near the nominal edge of halos – overdensities of $\sim 10^2\,(\rho/\langle\rho\rangle)$; thus, the errors in defining halo mass via the spherical overdensity method will be negligible – less than a few percent, which is smaller than the discrepancy with the theoretical halo mass function (which will be discussed in §4.4). As shown in Fig. 4.6, the gas particle densities (ρ_g) and energies (u_g) experience very little error ($f_{\rho_g} \leq 1\%$ and $f_u \leq 0.5\%$), even at the highest local densities – crucial for

precision measurements of the X-ray- and SZ-based mass proxies.

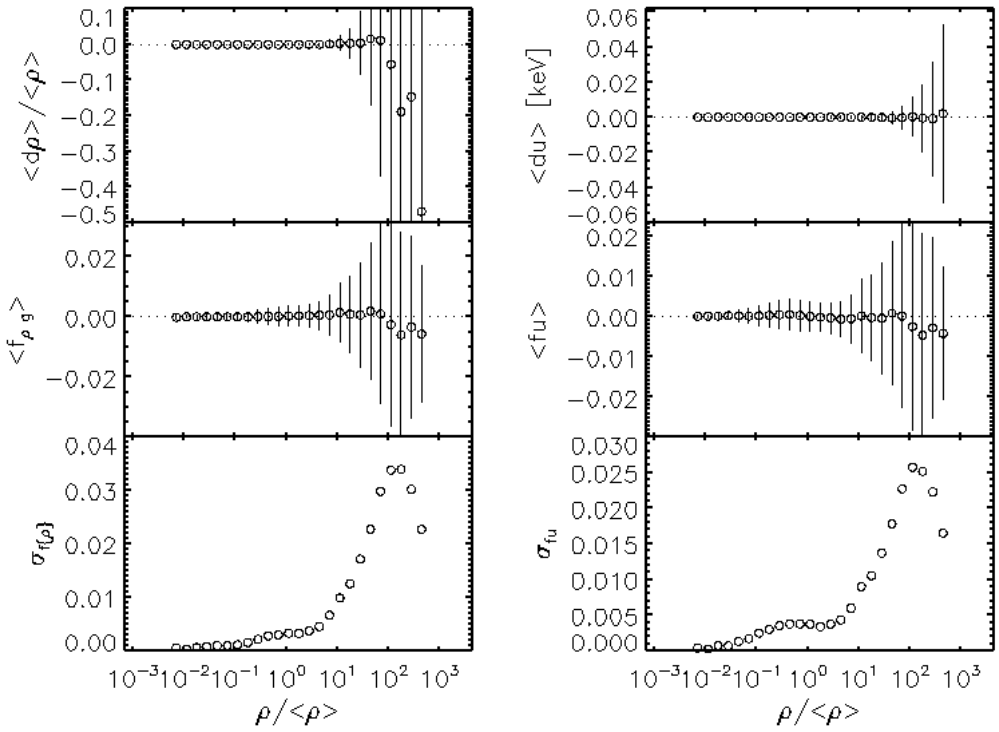

Figure 4.6: Interpolation errors in the gas energy and density for an interpolation interval, $\mathrm{d}s = 1$, at redshift, $z \sim 0$. The top panel shows the mean error in density (nearest-neighbor distance). The middle panels show the mean fractional error in the density (nearest-neighbor distance). The bottom panel shows the error in the mean of the fractional density (nearest-neighbor distance).

Next, we briefly look at a similar set of results – the comparison of errors in a series of interpolation intervals, $\mathrm{d}s$. In Fig. 4.7, the mean errors and errors in the mean increase with the local density, as well as the interpolation interval, which is expected: the larger the interpolation interval, the more time there is for a particle's trajectory to be modified. The largest errors in position (*i.e.,* $12\,h^{-1}\,\mathrm{kpc}$ at $\mathrm{d}s = 4$) are still less than the simulation resolution set by the softening length. The mean errors in the velocity in the densest regions increase by about 30% from $\mathrm{d}s = 1$ to $\mathrm{d}s = 4$. The errors in kinematics for gas particles, however, undergo much smaller changes with increasing snapshot interval

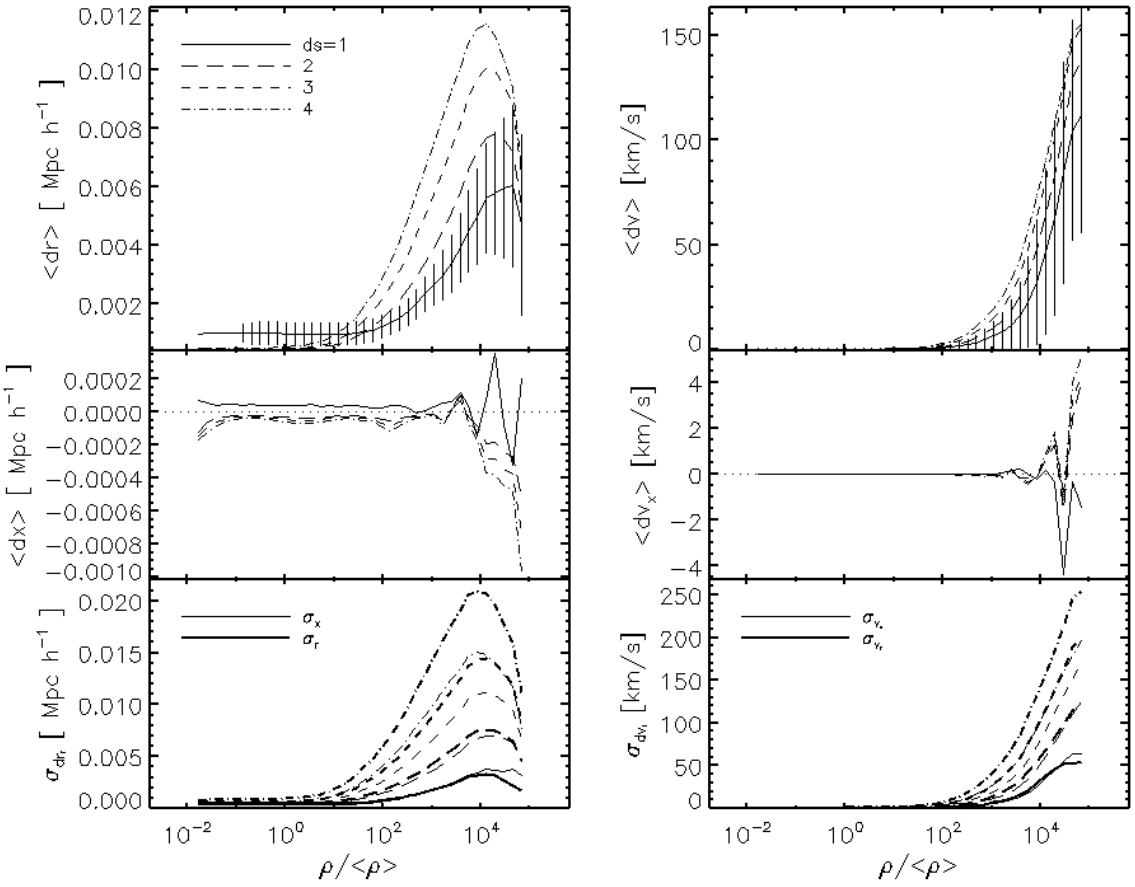

Figure 4.7: Interpolation errors in position and velocity for dark matter particles, comparing multiple interpolation intervals, ds, at redshift $z = 0$. The top panel shows the *mean deviation* in the three-dimensional position, $\langle \mathrm{d}r \rangle$, (velocity, $\langle \mathrm{d}v \rangle$). The middle panel shows the mean deviations in position (velocity) for each cartesian coordinate, $\mathrm{d}r_i$ ($\mathrm{d}v_i$). The bottom panels show the error in the mean position, $\sigma_{\mathrm{d}r_i}$, (velocity, $\sigma_{\mathrm{d}v_i}$) for both the three-dimensional quantity and the individual cartesian coordinates.

(Fig. 4.8): the positional errors are much less than the softening length. The exercise is again repeated at the highest redshift that the MGS lightcone can reasonably probe, $z \sim 2$. The co-moving distances between snapshots are much larger at high redshift, so the errors are expected to increase more quickly with snapshot interval. In Fig. 4.9, we show the results for gas particle kinematics: for an interval, $\mathrm{d}s = 1$ (solid), the errors are of the same order of magnitude or less as at low redshift. The mean positional error begins to exceed the softening length when two intervals ($\mathrm{d}s = 2$) are used. We also show the error in

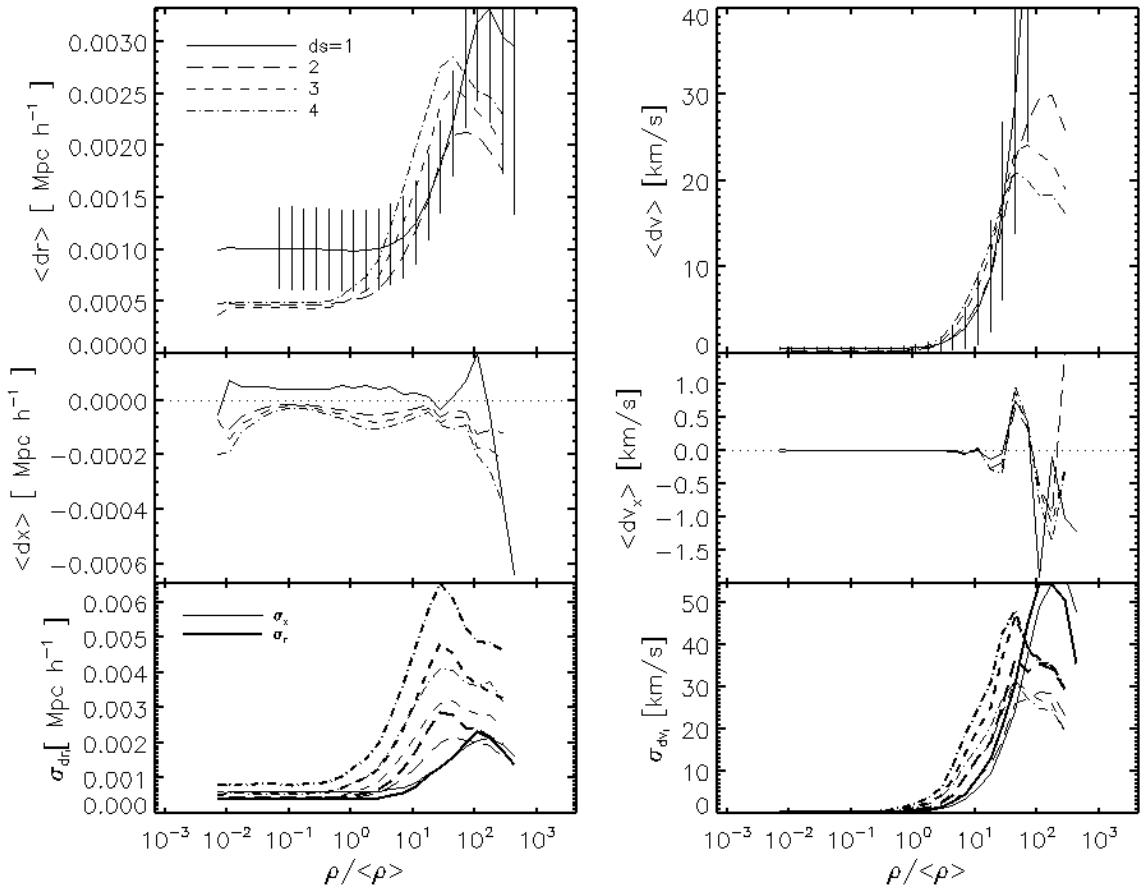

Figure 4.8: Same as Fig. 4.7, but for *gas* particles.

dynamical properties at high redshift and for multiple interpolation intervals in Fig. 4.10. Again, the errors rapidly increase with interval size, and they remain within acceptable bounds ($\leq 5\%$) for d$s = 1$ only. While at late times, acceptable levels of error can be achieved with larger interpolation intervals, single intervals are required at high redshift.

Finally, we briefly discuss particle trajectories for some of the densest particles in our quarter-billion particle sub-sample. To provide a visual sense of the kinematics and the effect of interpolation during a trajectory, Fig.'s 4.11 and 4.12 shows the x-y plane trajectories of dark matter and gas particles, respectively. Each trajectory starts at redshift, $z \sim 0.0526$, and concludes at $z = 0$. At the time (in snapshot steps) half-way through the

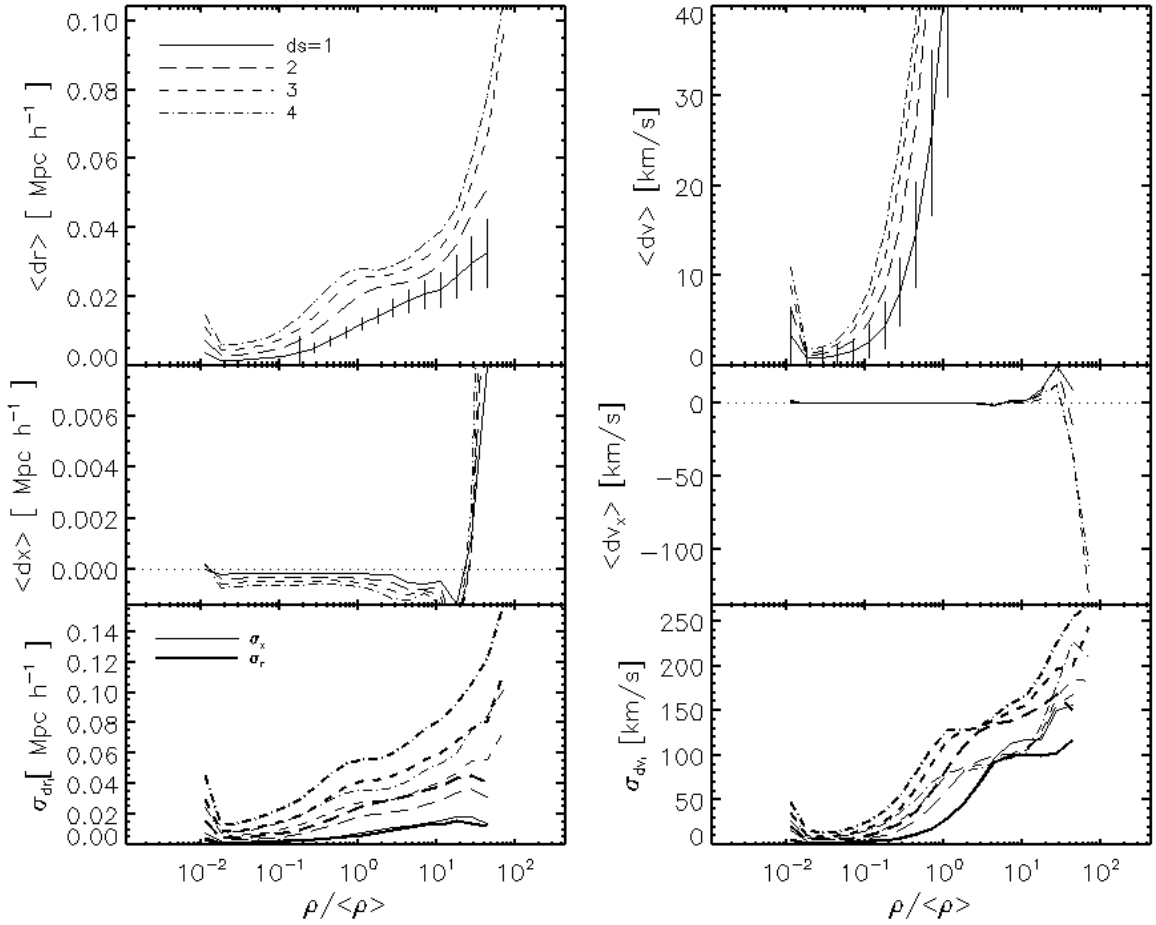

Figure 4.9: Same as Fig. 4.8, but at redshift, $z = 1.95$

trajectory, the interpolated position is marked with a red filled circle, where the interpolation is performed with snapshot interval, d$s = 1$. By visual inspection, the interpolated positions do not deviate significantly from the true trajectories, even for the substantially curved trajectories; note the $50h^{-1}$ kpc scale bar at the bottom of each box. In contrast, gas particles experience collisional forces (*i.e.,* pressure), which leads to more uniform trajectories.

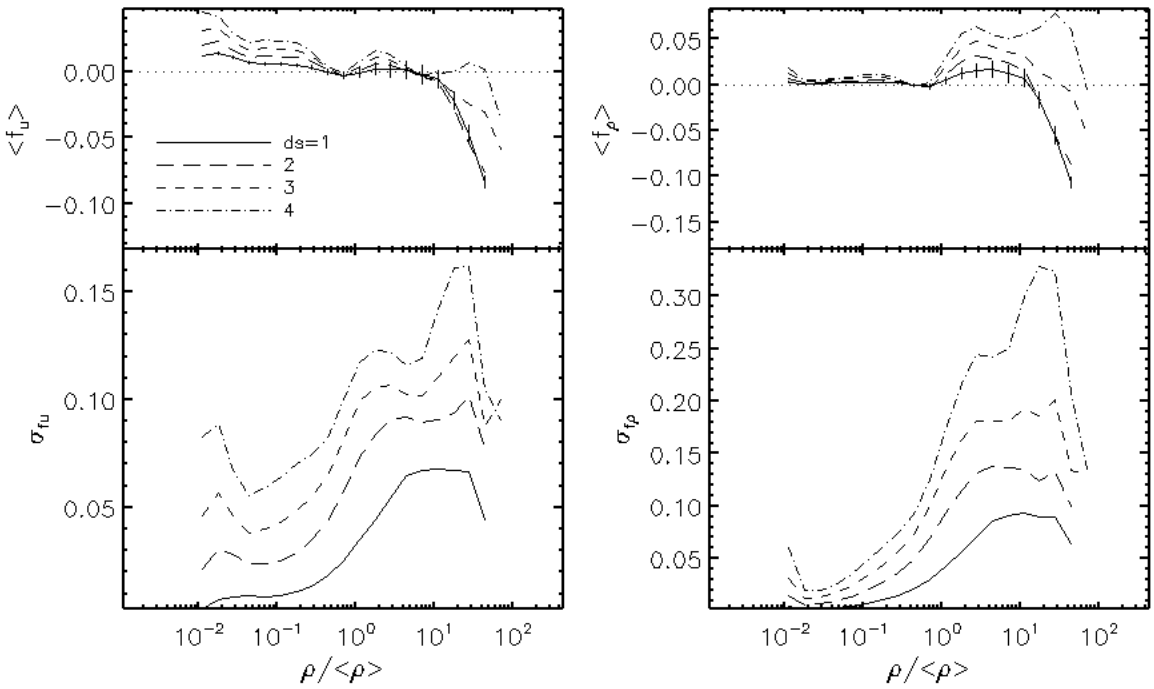

Figure 4.10: Interpolation errors in gas energy and density, comparing multiple interpolation intervals, ds, at redshift $z = 1.95$.

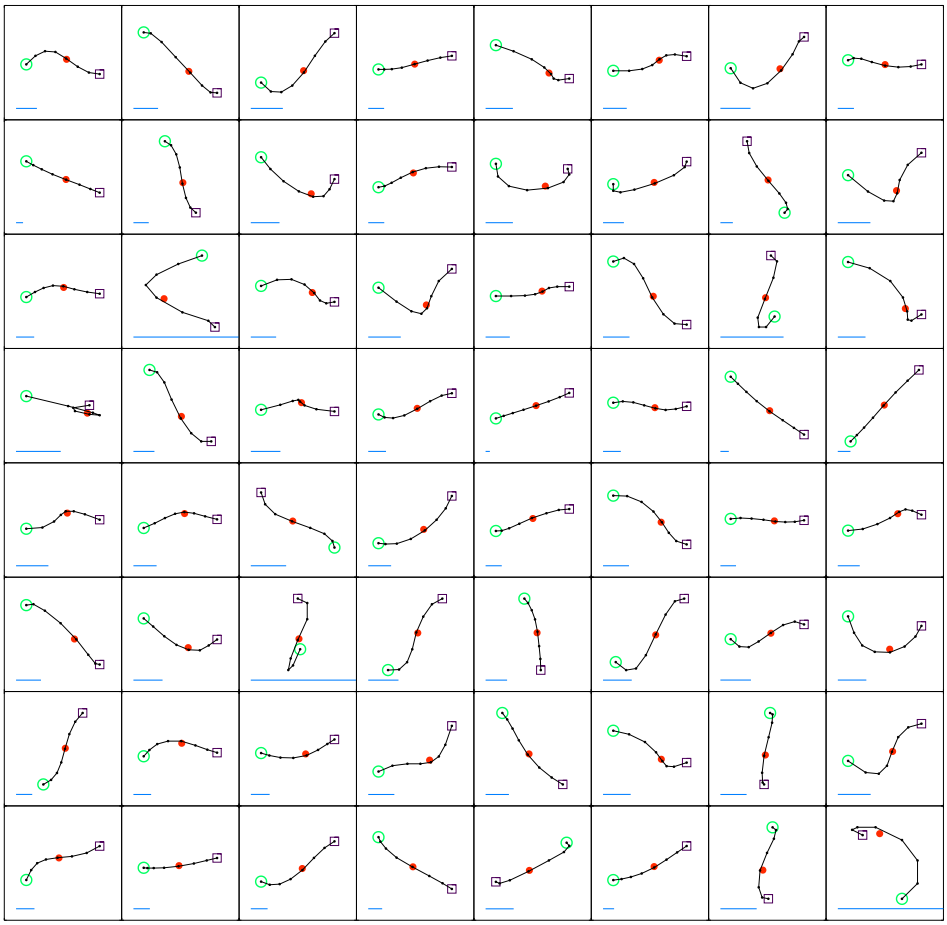

Figure 4.11: The trajectories in x-y position space of the 64 densest dark matter particles in a random sampling of the MGS volume near redshift, $z \sim 0.05$. The particle starts at the earliest epoch at redshift, $z \sim 0.0526$ (green, open circle), and travels through the interpolated position (red, open circle) at the target snapshot at redshift, $z \sim 0.026$. It's trajectory concludes at the lowest redshift, $z = 0$ (open, purple square). The (blue) solid lines represent a scale of $50h^{-1}$ kpc, which is equivalent for both axes (x is horizontal, y is vertical).

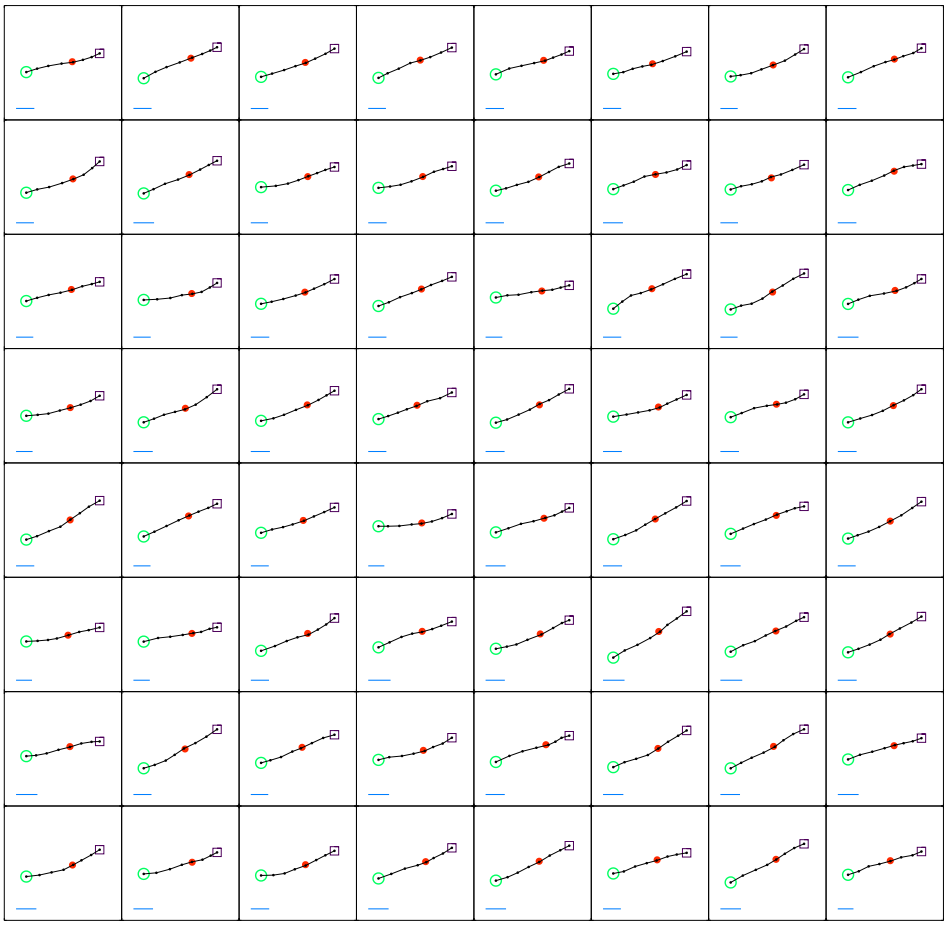

Figure 4.12: Same as Fig. 4.11, but for gas particles.

4.4 Halo Measurements

First, we measure the gas fraction within halos as function of the total halo mass at four epochs to trace the evolution of the ICM through the lightcone. Fig. 4.13 shows that the gas fraction ($f_{\rm gas} \equiv M_{\rm gas}/M_{\rm tot}$) at the current epoch is $\sim 13\%$ for halos with mass, $\sim 5 \times 10^{14}$ M$_\odot\, h^{-1}$, and just 8% for halos with mass $\sim 5 \times 10^{13}$ M$_\odot\, h^{-1}$. The lower gas fraction of smaller halos is driven by the pre-heating of the gas at high redshift: highly energetic gas is driven outside the shallower potential well of smaller halos, while it remains captive within deeper potential wells. The measurements in the MGSVSS are consistent with those made in the full simulation volume (shown as the solid curves here; Stanek et al., 2009) at high and low redshifts.

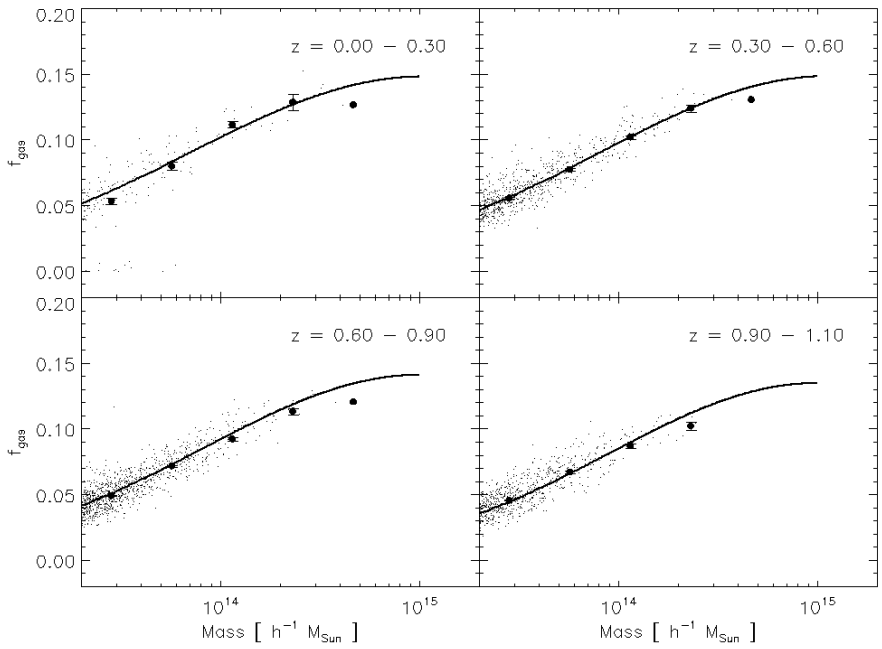

Figure 4.13: Gas fraction within halos at four epochs. In each panel, the dots are individual halos, the filled circles represent halos binned by mass, with errors on the mean of those bins, and the line is the gas fraction as measured in the full-box simulation. .

Next, we compare the halo mass distribution in redshift slices of the MGSVSS with

the expectation of the Tinker mass function (TMF Tinker et al., 2008). At each epoch, the halo abundance is systematically lower than the TMF by $10 - 15\%$ for all masses; the scatter at low redshift is expected from small-number statistics. We find a comparable level of discrepancy as Stanek et al. (2009), who measured the distribution of halos at redshifts $z = 0$ and 1 in the full simulation volume. In that work, the authors again find the difference to be caused by the pre-heat prescription. The gravity-only run of the MGS has no pre-heat mechanism, and comparisons with the TMF show strong agreement. The expulsion of high-entropy gas in the pre-heat run causes a reduction in the local baryon fraction, which in turn aids in the reduction of the potential well depth.

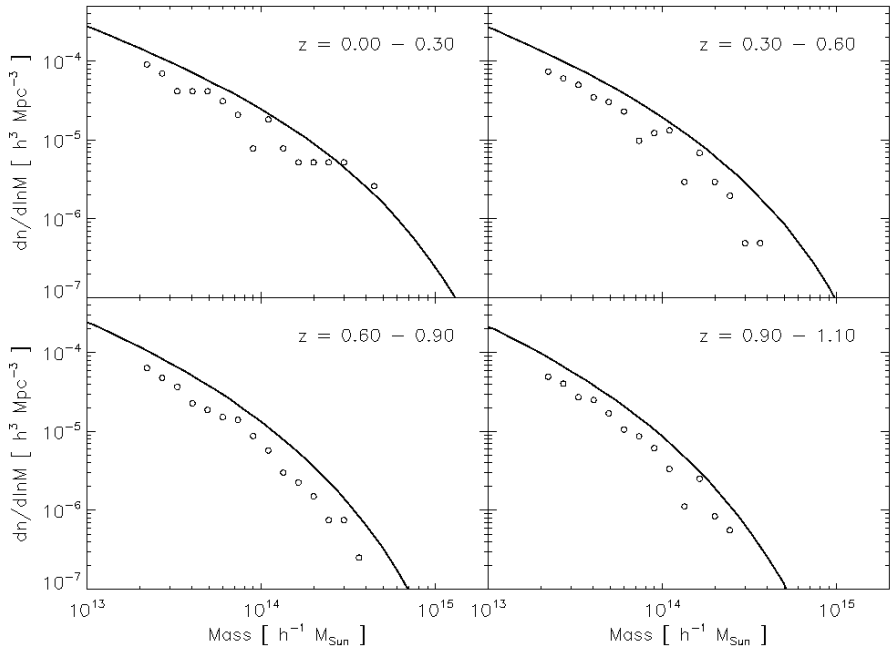

Figure 4.14: Halo mass function at four epochs. In each panel, the open circles are the number densities of halos binned in mass, while the solid line is the Tinker mass function at the median redshift of the redshift range for that panel. .

It is important to note that an error in the original halo-finding algorithm initially caused an incorrect measurement of halo properties. However, the first part of the two-fold

halo-finding process (*i.e.,* identifying potential halo centers as high-density particles), was not affected by this error. The second part – the identification of the halo edge, and thus the mass – was indeed affected. The halos used in this dissertation have had their properties re-measured, given the original set of halo centers. We have found that most properties, as evidenced in this section, are not biased by this (after re-measurement); however, as will be seen below, some properties of the galaxy distribution may yet be due to this original error. The final publication of this work will include a new set of cleanly measured halos.

4.5 Galaxies

There exist several methods for adding galaxies to N-body simulations. However, they typically rely on very low-mass (sub)halos, which are not well-resolved in MGS ($M_{\rm th} \sim 5 \times 10^{13}$ $M_\odot$) – *e.g.,* halo occupation distribution/conditional luminosity function methods; or they are not fully calibrated to observations, such as Semi-Analytic Models (SAMs). In contrast, ADDGALS (**A**dding **D**ensity-**D**etermined **GA**laxies to **L**ightone **S**imulations) is based on a luminosity-dependent biasing scheme: it relies on a 1) relationship between local dark matter densities and luminosity, which 2) is calibrated tightly with a luminosity-dependent galaxy 2-point correlation function observed in SDSS. Below, we describe the process in more detail.

High-resolution simulations, in which SAMs and subhalo methods have been applied, constrain the probability, $P(\delta|L/L_*)$, of galaxy counts in a region with local dark matter (over)density, δ, conditional on the local luminosity density, L/L_*. The parameters of the conditional probability are taken from fits to the observed 2-point correlation function in the SDSS galaxy catalogues for a given luminosity bin, L. Then, as luminosities are drawn from luminosity functions of the SDSS galaxy population, galaxies are randomly placed at the locations of dark matter particles according to the local density measure. A galaxy

then receives real dynamical information from the dark matter particle. The properties of high-redshift galaxies are evolved passively from low-redshift populations. Since high-redshift galaxies are not as well understood as those in the local universe, ADDGALS is under continuous development to refine the application of galaxies at early times.

For the purposes of cluster-finding, galaxy photometry provides important proxy measures of line-of-sight distance. ADDGALS achieves high photometric fidelity by creating realistic local color-density relationships. First, a local density for each galaxy is measured based on a nearest neighbor measurement of galaxies; the density estimate is then combined with its luminosity to choose the most closely related spectral energy distribution (SED) from the SDSS galaxy catalogue. Evolution is incurred by K-correcting the SED to the appropriate redshift. Also critical for many cluster-finders is the existence of brightest

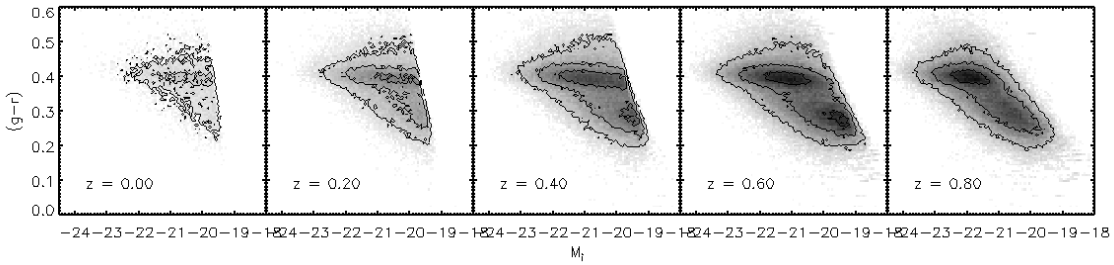

Figure 4.15: Color-magnitude diagram at five epochs with *absolute* i-band magnitude and color, $(g - r)$. The bright red sequence and dimmer blue "cloud" are apparent at each epoch. These galaxies have all met a luminosity cut of $0.4L_*$

cluster galaxies (BCGs), which hold a unique place in the cluster environment: each cluster is thought to have (at least) one BCG near its center. Therefore, while typical galaxies are inserted into the lightcone with only knowledge of the local *dark matter* density, BCGs are instead inserted directly at the center of halos with zero velocity and according to the host halo mass. BCG luminosities are set according to the observed location of BCGs in the galaxy luminosity function and by the inferred relationship between halo mass and BCG (Hansen et al., 2009); but colors are added in the same manner as for all other galaxies.

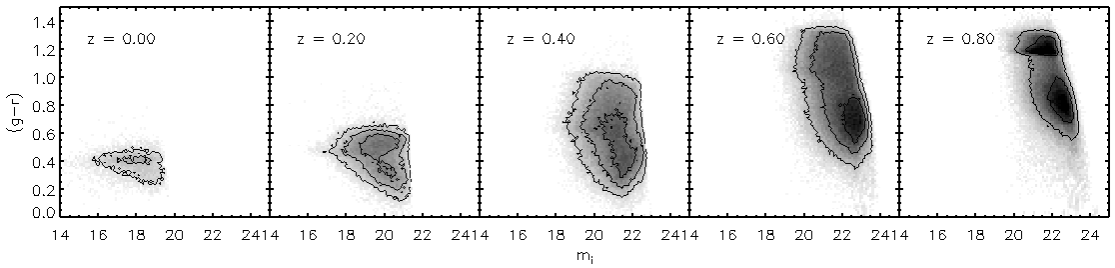

Figure 4.16: Same as Fig. 4.15, but with *apparent* magnitudes. The bright red sequence and dimmer, blue cloud show clearly for redshift, $z \leq 0.4$, and then disappear until redshift, ~ 0.8.

The creators of ADDGALS have performed extensive tests and comparisons with real-sky data to ensure the observational fidelity of their mock catalogues in several different N-body simulations. We next present results from a suite of diagnostic tests, designed to check the fidelity of the ADDGALS application to the MGSVSS. We measure several properties for comparison against galaxy observations, many of which were noted in Chapter II. Some of the tests may appear simplistic, but the ADDGALS algorithm is still under development and several simple tests should be covered to make apparent any potentially problematic aspects of the galaxy population. For most of the following discussion, we impose a minimum absolute magnitude at each redshift, by limiting the galaxy population to those galaxies which are brighter than $0.4L_*$.

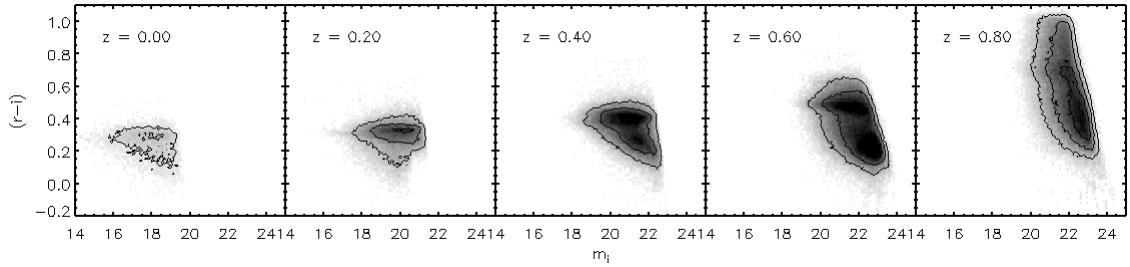

Figure 4.17: Same as Fig. 4.16, but for $(r - i)$. A red sequence is clearly differentiated from the dimmer blue cloud at redshifts, $z \sim 0.4 - 0.8$.

First, we consider the color-magnitude distribution of the galaxies, which will be the primary driver for the cluster-finder discussed in Chapter V. The red sequence appears at each epoch of the color-*absolute* magnitude diagram of Fig. 4.15, while it disappears at intermediate redshifts in the color-*apparent* magnitude diagram of Fig. 4.16. The reappearance of the red sequence in the apparent magnitude at high redshifts ($z \sim 0.8$) is unexpected. In Fig.'s 4.17 and 4.18, we also show the color-apparent magnitude distribu-

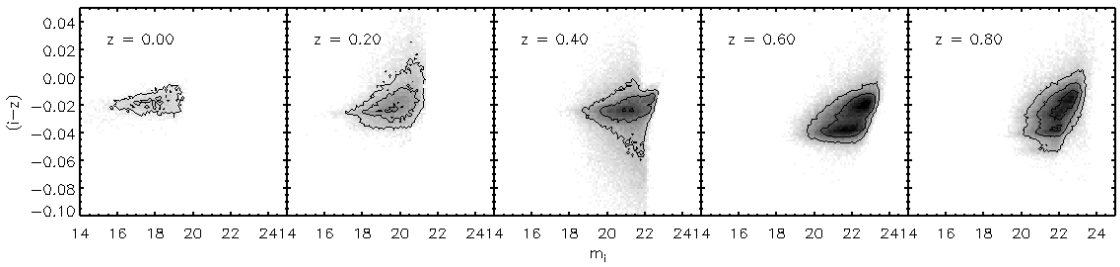

Figure 4.18: Same as Fig. 4.16, but for $(i - z)$. Blue and red galaxies are not clearly differentiated in color until redshift, $z \sim 0.6$; and the reddest galaxies are dimmer than the blue galaxies, a characteristic opposite that of the other color-magnitude diagrams shown here.

tions for $(r - i)$ vs. i and $(i - z)$ vs. i, since these colors will be used for cluster-finding at intermediate and high redshifts. The red sequence appears in $(r - i)$ color near redshift $z \sim 0.2$; the color segregation becomes apparent by $z \sim 0.4$, when it disappears in $(g - r)$. For the $(i - z)$ vs. i distribution, blue and red galaxies become vaguely segregated by redshift, $z \sim 0.6$; however, that blue galaxies are brighter than red is unexpected, and may inhibit the profitability of this measure in cluster-finding. The total number counts of galaxies as a function of color (Fig. 4.19) also depict the prevalence of bluer galaxies in $(i - z)$. Nevertheless, red populations in the field and in clusters are clear in the $(g - r)$ and $(r - i)$ colors. Despite the unexpected color distribution, the $(i - z)$ color may be useful as a proxy for distance. Fig. 4.20 shows the evolution of each color, both for non-BCG galaxies (upper panel) and BCGs alone (lower panel); where the slope in the color-z diagrams is

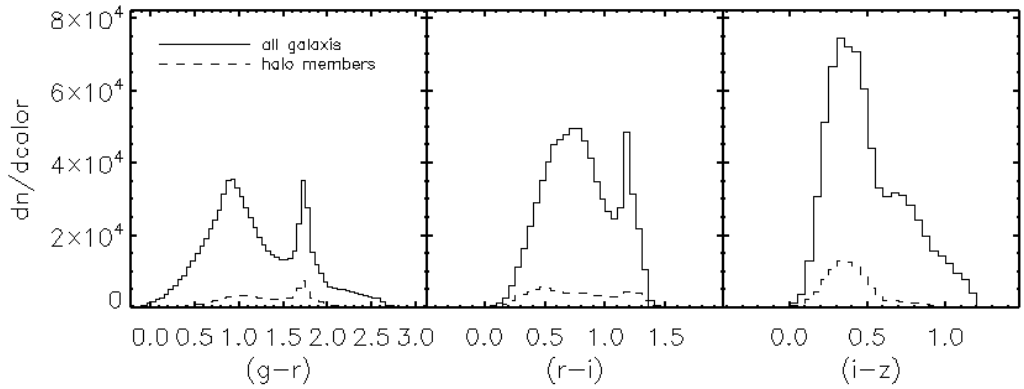

Figure 4.19: The number of galaxies, d$n$dcolor, at all epochs as a function of color for $(g-r)$, $(r-i)$, and $(i-z)$ colors. All galaxies are shown (solid), along with the subset of galaxies that are within R_{200} of a halo center (dashed)

steep enough, the relationship between color and redshift is sufficiently unique to assist in mapping color to redshift. Usually, $(g-r)$ is the prominent distance proxy at low redshifts, where its slope with redshift is steepest; at $z \sim 0.4$, the slope for $(r-i)$ steepens, and at $z \sim 0.8$, the same happens for $(r-i)$.

Finally, we present the luminosity function for all galaxies (without the $0.4L_*$ cut) in Fig. 4.21 in four bands – g, r, i, and z. We perform a fit to the Schechter function at low redshift, $z = 0.1$, and find M_* in agreement within 0.25 magnitudes with the results of Blanton et al. (2003), who measured the SDSS galaxy sample at $z = 0.1$.

4.6 Measurements of Halos by Mass Proxy

In this section, we discuss halos in terms of intrinsic mass proxies. First, the intrinsic halo occupation distribution of galaxies is shown in Fig. 4.22. The galaxies are declared as halo members if they reside within R_{200} of the halo center. The power-law trend between M_{200} and $N_{\rm gal}$ extends from the highest masses all the way down to $2 \times 10^{13}\ h^{-1}\ \mathrm{M}_\odot$; accompanying the power-law is a scatter whose magnitude is approximately constant across all masses. Galaxy formation is highly sensitive to the local environment, including the

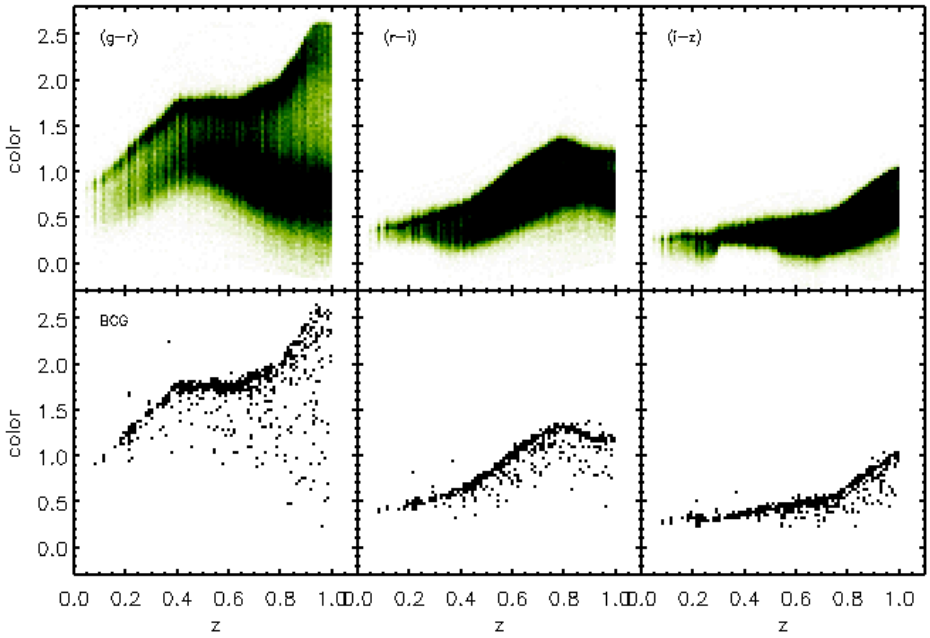

Figure 4.20: The evolution of galaxy color with redshift for all galaxies and for brightest cluster galaxies (BCGs) in three colors, $(g-r)$, $(r-i)$, $(i-z)$.

total halo potential, as well as the thermal complexity and activity within the ICM. For example, AGN in clusters of any mass can potentially impede galaxy formation, driving down the richness in those clusters. A more complete investigation of the scatter in this sample remains to be undertaken.

Next, the scaling relations for the integrated and central SZ flux are shown in Fig. 4.23: Y_{int} is the total SZ flux within R_{200} (recall Eqn. 2.22), and the central decrement is measured within a few $h^{-1}\,\mathrm{kpc}$. Y_{int} experiences very little scatter at all masses, except for a few halos which lie very far from the mean; these remain to be investigated. On the other hand, the central flux experiences a relatively high degree of scatter in flux at fixed mass for all masses. The difference and cause of the scatter was discussed in §2.3.2.

Finally, we show the number distribution of halos in terms of their intrinsic richness, N_{gal}, and total flux, Y_{int}, in Fig. 4.24. Note the power-law behavior above $Y_{int} = 2 \times$

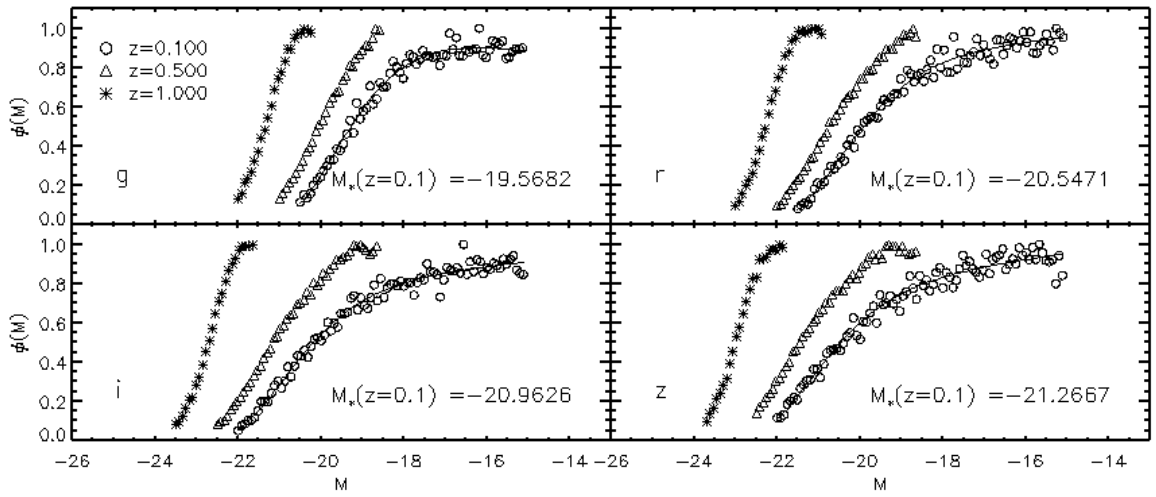

Figure 4.21: The luminosity density function of galaxies at three epochs as a function of absolute magnitude, in four bands – g, r, i, and z. All galaxies are included at redshift $z \sim 0.1$, while, for clarity, the dimmer galaxies in the higher redshift bins are not shown. The galaxies in the lowest redshift bin (at $z = 0.1$ with width 0.1) are fit the Schechter function, giving M_*, the magnitude at which the luminosity markedly turns over (*i.e.,* , the 'knee').

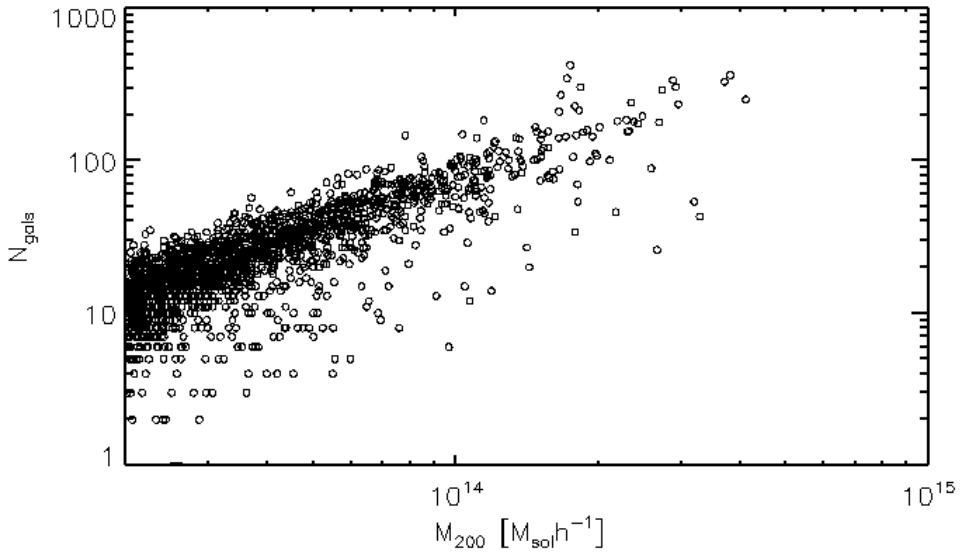

Figure 4.22: Intrinsic halo occupation of galaxies within the MGS sky survey. The galaxy population has been limited to above $0.4L_*$ appropriate for the galaxy's redshift.

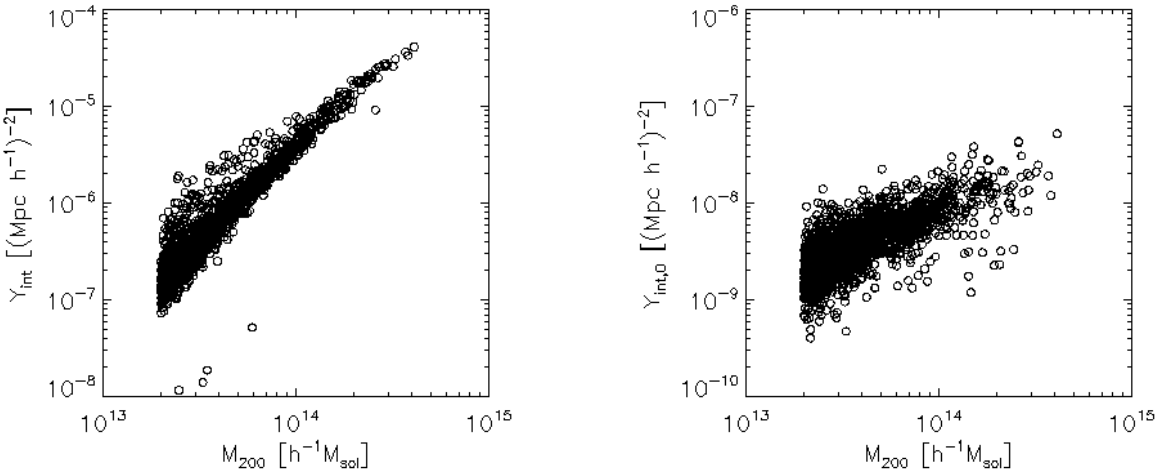

Figure 4.23: The total intrinsic SZ flux, Y_{int}, within R_{200} of the halo (left) and central flux (right).

$10^{-7}(h^{-1}\,\mathrm{Mpc})^{-2}$ for the flux distribution and the approximate power-law for the richness distribution. Both are consistent with expectations from the form of the halo mass function and the observed richness distribution in the maxBCG catalogue (recall Fig. 1.13).

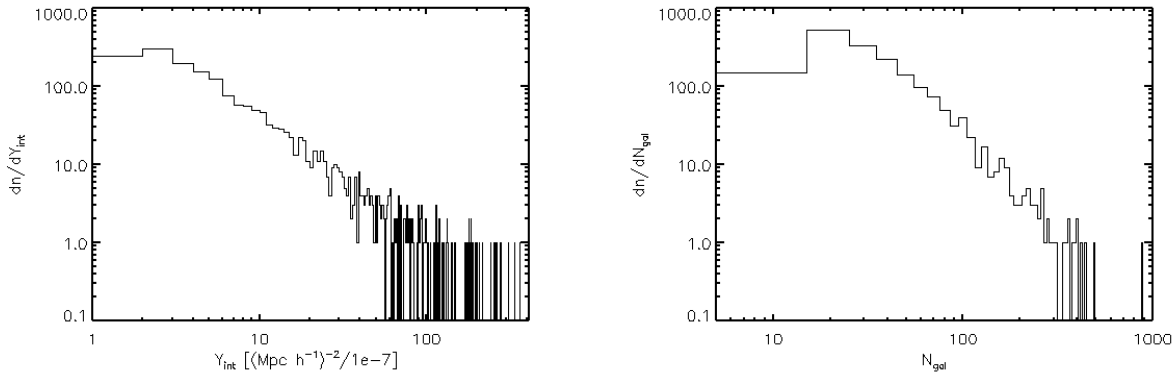

Figure 4.24: The number of halos as a function of the total intrinsic flux (left) and as a function of the intrinsic halo occupation of galaxies N_{gal} (right).

4.7 Sky Maps

The SZ sky maps in Fig. 4.25 are constructed by summing particle pressures or velocities along the line of sight. Each snapshot's contribution to the SZ signal is given by

summing the energy within a *voxel* (or volumetric pixel, with area in the plane of the sky and depth in redshift),

$$\langle y_{\rm tSZ}\rangle_{\rm vox} = \frac{\sigma_{\rm T}}{m_{\rm e}c^2}\,(\gamma-1)\,M_{\rm g}\,\frac{\sum_{\rm p} u_{\rm p}}{A_{\rm vox}}, \tag{4.2}$$

where γ is the adiabatic index; $M_{\rm g}$ is the mass of the gas particle; $u_{\rm p}$ is the internal energy of the gas particle; $A_{\rm vox} = \Omega_{\rm vox} d_{\rm A}^2(z)$ is the physical area of the voxel; $\Omega_{\rm vox}$ is the angular area of the voxel in the sky (which is set by the chosen resolution of the map); and $d_{\rm A}(z)$ is the angular diameter distance from the origin (observer) to the voxel that lies at redshift, z. Eqn. 4.2 is derived from the definition of the thermal SZ effect (Eqn. 2.14). Fig. 4.25 shows the resultant $\sim$100deg.^{2} SZ map at 150 GHz; the left map shows the decrement in linear units, while the right map shows the same field in logarithmic units.

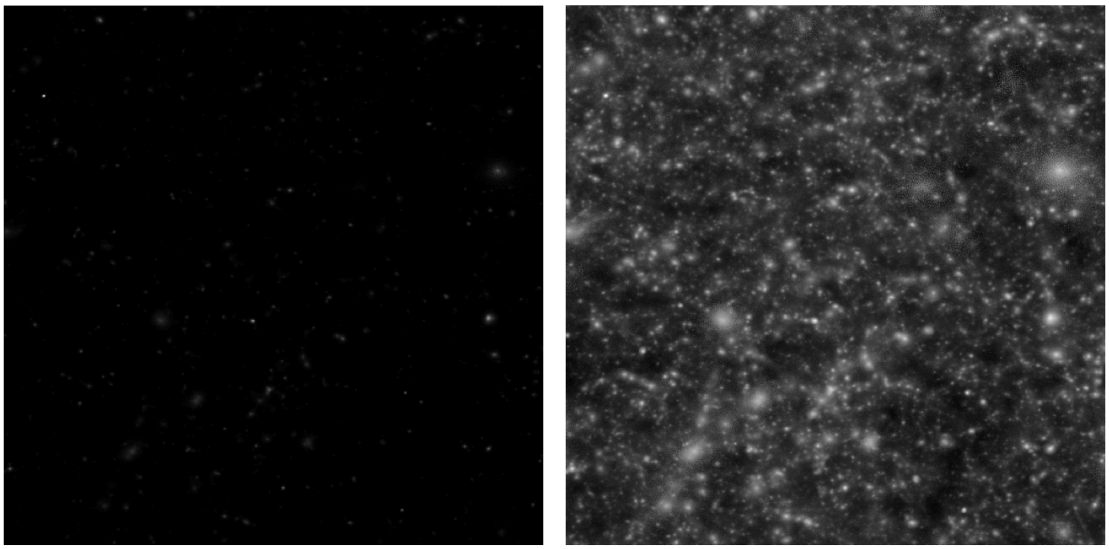

Figure 4.25: Maps of $\sim$100 deg^2 of the MGSVSS SZ sky, with intensity on a linear scale (left) and on a logarithmic scale (right). These maps do *not* include any observational (neither astrophysical sources, telescope, nor atmospheric) noise. This covers 50-60 deg. in latitude and longitude.

Beyond the construction of the pure SZ signal from the lightcone particles, we transform the signal into one more like that found in the real observed sky of the South Pole Telescope

(SPT), which is observing the microwave sky at three frequencies. For a full description of SPT, please see Ruhl et al. (2004). The process for adding astrophysical signals and observational noise to signal-only sky map is encapsulated by

$$\mathbf{M}_{\rm tot} = \mathbf{M}_{\rm inst} + \mathbf{M}_{\rm beam} \otimes [\mathbf{M}_{\rm astro} + \mathbf{M}_{\rm SZ}] \,, \tag{4.3}$$

where $\mathbf{M}_{tot}$ refers to the total noise map, which is composed of *inst*rumental noise, as well as the *astro*physical signal and the *SZ* signal maps, as observed with a telescope of a given *beam*size. The vector notation denotes that the map set contains maps at multiple frequencies.

The most important astrophysical signals for SZ cluster-finding are the CMB and point sources. Though we reserve the point source addition for another work, we simulate the CMB in the following way. First, we simulate a CMB power spectrum via CMBFAST (Seljak and Zaldarriaga, 1996) with input parameters of the MGS cosmology. The CMB power is then placed on a two-dimensional map in frequency space, where the power has been randomized with Gaussian noise. This map is then Fourier transformed to produce an angular space map. The flat-sky approximation (White et al., 1999) is valid, since 100 deg^2 is but a small fraction (0.24%) of the total sky. The SZ temperature decrement (recall Eqn. 2.19) is then simply added to the CMB map, producing a minimalist microwave sky. To mimic the SPT beam, we convolve the microwave sky with one-arc-minute Gaussian beam. The one-arc-minute smoothed microwave sky is shown in Fig. 4.26. SPT's instrumental noise has two constituents. First, the white noise is simulated via the addition of a random Gaussian distribution to the smoothed microwave map $\mathcal{O}(17\mu\text{K})$. The second constituent, 'Atmospheric noise', originates in observed spatial fluctuations in atmospheric emission driven by wind and the azimuthal scanning method of the survey. We simulate this composite noise by adding $1/f^{\alpha}$ noise, where the frequency, f, is taken from the telescope scan speed; the power is set to $\alpha = 2$ by SPT simulations and observations of the

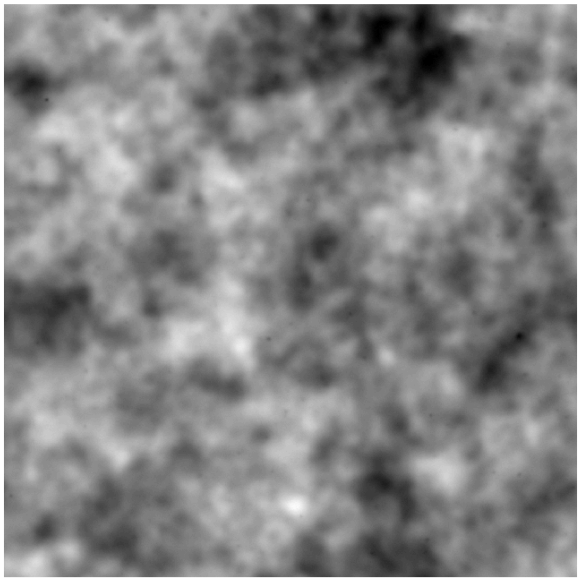

Figure 4.26: Same sky patch as Fig. 4.25, except CMB has been added and the scale is now linear in temperature.

atmosphere. Finally, we mimic the SPT data reduction pipeline by removing these atmospheric variations with a high-pass filter. This simple process consists merely of removing the largest modes of the map, the result of which can be seen in Fig. 4.27. One of the brightest clusters can be seen just below and to the left of the center of all four maps. For complete descriptions of the SPT and the phenomena of $1/f$, bolometer, and atmospheric noise, we refer the reader to the following resources: Mather (1982); Ruhl et al. (2004); Milotti (2002); Chang et al. (2009).

4.8 Discussion and Conclusion

In this chapter, we discussed the construction and validation of the MGSVSS lightcone, some diagnostics and a general description of the galaxy population in the MGSVSS, and the construction of the SZ sky maps including noise. We have developed this simulated survey to be used in the following chapter and later works to optimize our methods for

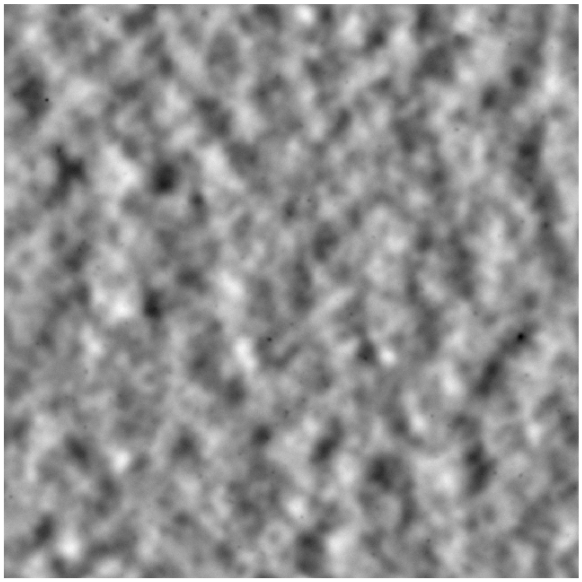

Figure 4.27: Same sky patch as Fig. 4.25 and Fig. 4.26, but atmospheric (1/f) noise and white noise (at 6μK) has been added. The map has also been high-pass filtered, consistent with SPT processing pipelines.

cross-calibrating SZ-optical information and to find clusters through joint-signal search methods.

The MGSVSS lightcone has been constructed by interpolating particle properties between time snapshots of the Millennium Gas Simulation (MGS). The fidelity of the interpolation method is such that errors in position for both gas and dark matter particles are smaller than the force-softening length; also, the dynamic quantities (energy and density) of the gas particles have sub-percent interpolation errors – much less than required for developing the next stage of joint cluster-finders and cross-correlation methods. The MGSVSS halos needed to be re-measured (in size and mass) after an error in the original finder was discovered. This resulted in a few changes to the halo distribution, but they are in general agreement with theoretical expectations of the halo mass function; also, the gas fraction-total mass relation takes a form expected from previous measurements of the halo distribution within full MGS halo sample.

The galaxies were added to the MGSVSS lightcone via the ADDGALS method. They have been shown to follow closely the observed distributions in color and magnitude. The halo occupation, however, displays substantial scatter that appears to be linked to the luminosity evolution of the galaxy distribution. This requires a great deal more investigation, as does the color and luminosity-spatial distribution within halos. We have also constructed a 10x10 $\deg^2$ SZ sky map upon which to perform mock cluster detection exercises; the SZ sky has also been dressed with various levels of astrophysical, atmospheric, and instrument noise to mimic the observational properties of the South Pole Telescope (SPT).

The next major steps for this work include work on the halo catalogue, the galaxy populations, and the SPT noise maps. First, we will re-find all halos in the lightcone after correcting the bug, and then perform halo diagnostic exercises again. Then, we will re-implement ADDGALS to get a new set of halo galaxies, including BCGs. Given the new halo occupation distribution, we will characterize the galaxy distributions in more detail and link them more closely to more observed distributions and other simulated galaxy distributions. Much of this work will be done on a halo-by-halo basis to obtain a more acute understanding of the galaxy occupation. Finally, we will implement a more sophisticated atmospheric noise, along with point sources, in the SZ sky maps.

CHAPTER V

Multi-signal Cluster-finding in the MGSVSS

As we have discussed, mass proxies provide the key connection between galaxy cluster abundances and cosmological constraints. Until now, clusters have been found in a single signal and then correlated with mass. With the advent of overlapping sky surveys at distinct wavelengths, the possibility arises of correlating signals to inform the signal-mass relations, as well as the cluster-finding process. This has the potential to provide a more robust and complete, albeit probably more complex, cluster abundance measurement. For example, the detection of a cluster in two signals, each with low likelihood, might be compounded to obtain a higher-confidence detection for that cluster.

In this chapter, we focus on the preliminary issue of understanding cross-correlations between clusters detected through multiple distinct signals – *i.e.,* SZ and optical. To that end, we perform cluster-finding independently in the optical and sub-mm wavelengths (*i.e.,* galaxy richness and SZ decrement) within the MGSVSS and measure the cross-correlated richness and SZ flux. The sky survey for this work is composed of 5x5 $\deg^2$, within the larger 10x10 $\deg^2$ sky described in the previous chapter.

5.1 Optically-selected Clusters

There exists a plethora of optical cluster-finding algorithms with distinct approaches, such as those based on a matched filter, the red sequence, or the centrality of the BCG

(*e.g.,* Postman et al., 1996; Gladders and Yee, 2000; Koester et al., 2007, respectively). For a broad survey of algorithms, we refer the reader to a recent overview by Gal (2008), which discusses many of the optical cluster-finding methods that have been used to date.

Despite the variety of algorithms, the typical two-step process is to 1) find the points of likely overdensity (potential center); and 2) then collect members that are associated with that overdensity; note that this is similar to halo finding, except that it occurs primarily in two spatial dimensions, where the third must be obtained through a proxy, such as color. The first part of the algorithm is the search for high-density regions in the galaxy field. Unlike halos, cluster centers are difficult to find in the two-dimensional sky, because measures of the local density depend on imperfect proxies. For example, the color-morphology-density relation (Dressler, 1980) is robust for high-richness clusters, but smaller clusters have less well-defined color segregation, and with fewer galaxies are more poorly resolved. The search for unique galaxies which tend to lie near cluster centers is largely motivated by this challenge (recall §2.1). The second part – collecting galaxies within some edge – is susceptible to the same issue of characterizing local density. This step encounters an additional challenge of segregating true members from field galaxies, a challenge which is driven by highly imperfect information about galaxy redshift/distance.

Though there are many algorithms, very few comparison studies have been undertaken, (Kim et al., 2002; Bahcall et al., 2003; Rizzo et al., 2004; Lopes et al., 2004), and none of them comprehensive across the classes of finders. Future experiments, like the Dark Energy Survey, will require a robust and comprehensive comparison study in order to maximize the information drawn from galaxy surveys.

5.1.1 Red Sequence Cluster-finding

The 'red sequence' (§2.1.1 of this dissertation and CRS of Gladders and Yee, 2000) is among the most useful signatures of a cluster. We employ an algorithm here that is focused

on the use of the red sequence, with the addition of centering on BCG-like galaxies. Below we summarize the algorithm, and then present the process in detail, highlighting key inputs, concluding with a discussion of the robust features and failure modes.

We begin by producing an absolute, i-band magnitude-limited sample of galaxies out to redshift, $z = 1$ where the brightness minimum is $0.4L^*$, and L^* marks the break in the galaxy luminosity function. Since we don't have full luminosity functions at each redshift to measure L^*, we require another method to obtain the proper limit at each redshift. Instead, we use a previously constructed evolving and K-corrected i-band limit derived from galaxy formation models. We then apply a multi-dimensional filter in color-magnitude-position space to obtain neighborhoods of galaxies, where all pairs within a neighborhood have galaxies which lie within some maximum distance of each other in that multi-dimensional space. The neighborhoods are potential clusters, which are later filtered again, but more strictly according to the width of the color ridge-line.

Next, the local spatial density of each galaxy within a neighborhood is measured through its local two-dimensional potential, $\phi \propto \sum_g 1/(r + r_{\rm soft})^\alpha$, where r is the distance between a galaxy and one of its neighbors, and $r_{\rm soft}$ is a softening length to reduce the likelihood of galaxies in projection from becoming centers in the filtered neighborhood of galaxies. We add a buffer in the measurement of the central density proxy to prevent projected galaxies that are very close to the center from appearing as a cluster center. This is more likely to happen for neighborhoods at higher redshift, where even stringent requirements on color proximity can permit distant galaxies to project into the potential cluster. All galaxies then are sorted by local density, producing a list of rank-ordered potential cluster centers. We then rank galaxies by local density Finally, we iterate over the list of potential centers and search for members within the neighborhoods of those high-density galaxies; members are chosen to be dimmer than the central galaxy, and nearby in color

space. They are all marked so as to preclude from being centers of other clusters.

Next, we present the major steps in the process, highlighting the input parameters.

1. Find all potential clusters, grouping them by their proximity in angular distance, color ($(g-r)$, $(r-i)$, and $(i-z)$), and luminosity.

    - The angular distance is derived from the angular diameter distance and a physical aperture (chosen as $1h^{-1}$ Mpc, the size of a typical cluster); this requires an assumption of the cosmology (via the Hubble parameter and the mean cosmic matter density), as well as the galaxy redshift. This is the only point at which we assume knowledge of the galaxy redshift.

    - All of the galaxies must be within 0.1 of each other in color space. This parameter sets the balance between the multiplicity of clusters per halo (breaking up halos into multiple clusters) and blending of multiple halos into a single cluster; it is calibrated through multiple runs of the cluster finder and through prior knowledge of ridge-line widths.

    - Pairs of galaxies in a local neighborhood must differ by no more than six magnitudes; this choice of magnitude difference is obtained through trial error, balancing between preventing projected non-cluster galaxies from entering the neighborhood with ensuring that all of a cluster's galaxies are included in the neighborhood.

2. Measure the local density,

$$\phi \propto \sum_{g} 1/(r + r_{\rm soft})^{\alpha}$$

    , around each galaxy to determine potential centers:

    - Varying α has very little effect on the output cluster sample, and is set to 1.2.

The softening length is set to $30\,h^{-1}$ kpc, slightly larger than the MGS particular softening.

3. Rank order the potential centers by how locally dense they are (according to Eqn. 2), where the brightest cluster galaxy is expected to be near, or at, the center.

4. Search through the list of potential centers and collect members within a color-magnitude space smaller than in Step 1; if the potential center is a cluster member already, go to the next potential center. If the potential center is not already a member of another cluster, find the galaxies that are nearby in color and magnitude with the following user-defined inputs.

   - Measure the variance in color, σ, of the galaxies in the potential center's neighborhood. Keep members that are within $\pm 2\sigma$ for $(g-r)$ and $(r-i)$ and $\pm 3\sigma$ for $(i-z)$; these pre-factors of 2 and 3 are user-defined.
   - Members must be within four magnitudes of the potential center (See Step 1 for how the magnitude difference is chosen).

5. We set the size of all clusters uniformly to 3' in consideration of the low-resolution maps of SPT, to which these clusters will later be matched. There exist robust methods for measuring size and richness estimates (Hansen et al., 2005; Rozo et al., 2009), which will be employed in the revision of this work.

We briefly comment on the galaxy population and the distribution within halos. We find that for low-mass halos ($< 10^{14}\ h^{-1}\ \mathrm{M}_{\odot}$), approximately one-third of the halos have brightest galaxies that are bluer than the median color of the halo galaxies; for high-mass halos ($> 10^{14}\ h^{-1}\ \mathrm{M}_{\odot}$), 20% of the brightest galaxies are blue. Also, as seen through visual inspection of many clusters, the central galaxy as determined through the measure

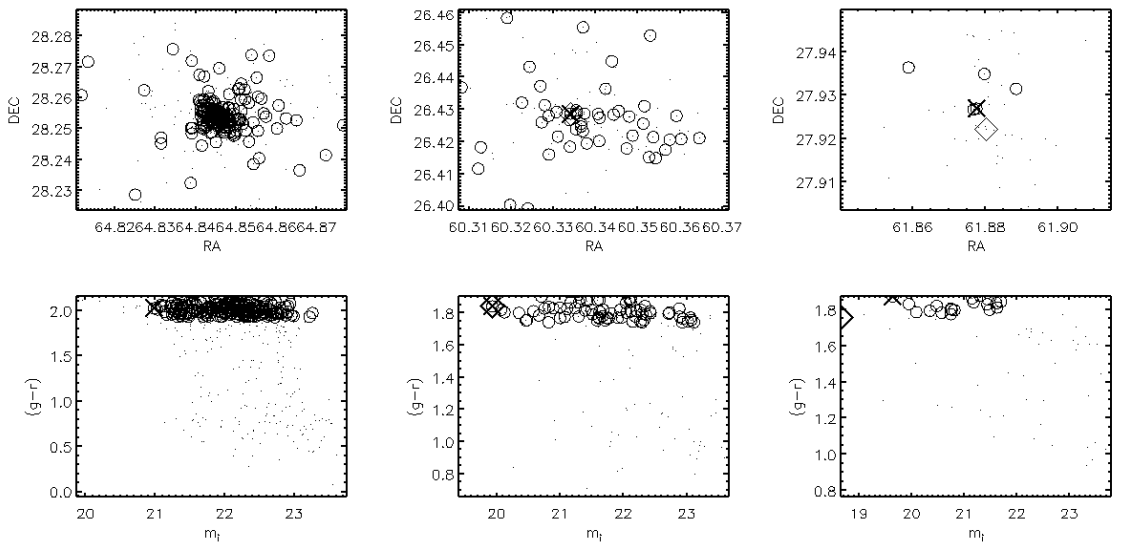

Figure 5.1: Three halos and the largest optically selected clusters found for each halo shown on the sky (top row) and in the $(g-r)$-$m_{\rm i}$ color-magnitude space (bottom row). Dots mark the galaxies that are members of the halos, the diamond shows the galaxy nearest the halo center, the open circles show the galaxies that are found by the cluster-finder, and the large 'x' marks the detected cluster center. The halos shown here have $N_{gal} = 225, 90, 20$, where the first is the largest in the survey, and the other two were selected based on their richness and nothing else.

of the local density (Eqn. 2) is not always the brightest galaxy. The combination of these two factors can potentially confuse the cluster-finder, which is constructed to seek bright red objects in cluster centers (in the densest part of the cluster). An example of this error is shown examples of detected clusters in Fig. 5.1: we present three halos and the detected cluster that shares the most members with each halo. The two larger clusters clearly find the red ridgelines of their respective halos, ignoring the "blue cloud," as expected. The largest cluster has a very red galaxy as its center, but not the brightest halo galaxy; consequently the finder appears to miss at least six galaxies. The members of the intermediate-richness cluster are not as concentrated on the plane of the sky, but they form a tight ridgeline, and the cluster center is also the halo center and the brightest halo galaxy. Finally, the poorest cluster is probably a false detection, as most of the cluster members are not also halo members. To further revise and characterize the finder, we would analyze

these clusters, particularly the failure in the poor cluster; it may be a high-redshift halo, where projected galaxies were combined with members of this halo.

To mitigate against the mis-centering issue, membership designation within our cluster-finder is not exclusive. Galaxies that are members of one cluster cannot be centers of a new cluster, but they can be non-central members. This mitigates the consequences of a poor choice of cluster center: if one cluster has a non-optimal center or reduced richness, then there may be other detections in the same region with a better measurement of the local richness and location. Multiple overlapping clusters within the region of a single halo can be detected and judicious post-processing can re-combine clusters into an optimal composite cluster – *e.g.,* if two clusters share more than 50% of their galaxies, and they are co-located within $\sim 1'$ (the resolution of SPT), then they can be combined into a single cluster.

The size of the initial color cut is a strong lever on the rest of the cluster-finding implementation: it controls the size of local neighborhoods from which clusters can be selected. The smaller the color ball is, the smaller the resultant clusters. On the other hand, the larger the color ball, the higher the probability of more distant galaxies projecting into the cluster from higher redshifts, producing blends; this highlights the peril of color as a detection feature, because it is also a distance discriminator that fails at high redshift, where galaxy colors are more heterogeneous, and the variance in color is larger.

5.1.2 Cluster Sample Selection Function

Matching

Folded into the cluster diagnostics is the matching process, which is easily refined, but crucial for characterizing our confidence in a cluster-finder, and for optimizing cross-calibration between finders in different signatures. For this exercise, we use matching based on the largest overlap in the number of members that are shared by a halo-cluster pair;

this represents the truest form of $1-1$ matching. We employ this method by searching through cluster-halo pairs and selecting those with the greatest membership overlap, where the members are signified by a unique identification number. This method, however, is computationally expensive, because we must match (by galaxy id) for each possible halo-cluster pair, and each matching is itself an expensive process. The membership-matching method is expected to succeed in the face of mis-centering, which afflicts spatial matching techniques.

As we begin to undertake multi-signal finding, matching will probably be trickier for signal cross-correlation. In working with SZ data, there is no information for the cluster distance, so we will be forced to use cylindrical matching. Cylindrical matching starts with defining an aperture around the target object, where the aperture is particular to each object or set by the survey resolution. Next, we find all counterparts whose objects lie within that aperture. Since there will likely be several optical clusters along the line of sight of a single SZ detection, we will need a way to find the best matched optical cluster for that SZ detection. One good choice is the richest cluster, because the SZ detection will often result from a large contribution from a single cluster along the line of sight; this is what we use for SZ-optical matches.

Sample Characterization

In this section, we measure the cluster selection function to diagnose the fidelity of our cluster-finder. The selection function has two components. The *completeness* signifies the number of halos that are actually detected by the cluster-finder, and the *purity* signifies the number of clusters that are true detections – *i.e.,* whose members actually belong to halos. First of all, the completeness for our sample is shown in Fig. 5.2 for both types of matching (membership and cylindrical) as function of halo mass and epoch. The lower mass and richness limits are $2\times10^{13}\ h^{-1}\ \mathrm{M}_{\odot}$ and 10 galaxies, respectively. The completeness remains

above 80% for all halo masses for both types of matching; and it generally decreases with redshift. This is a general indication the cluster-finder finds almost all of the halos above the lower mass limit of the MGSVSS.

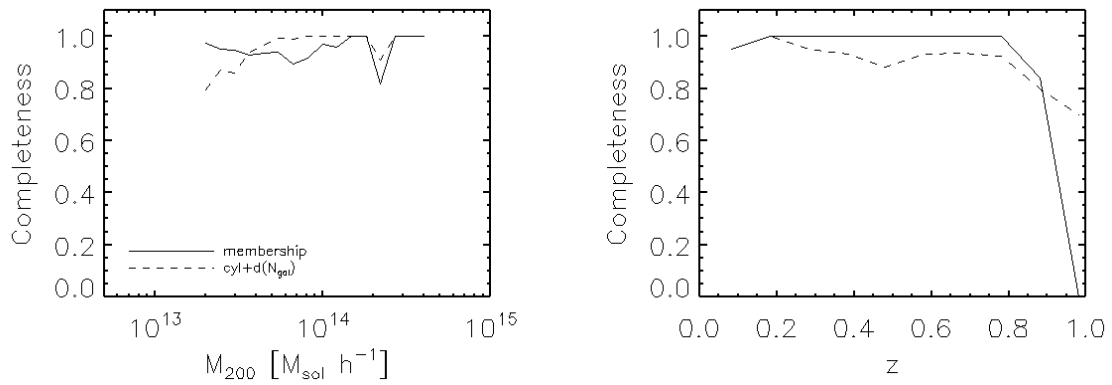

Figure 5.2: Completeness of the optical cluster-finding survey shown for two types of matching clusters to halos – membership-based matching (solid line), cylindrical-richness matching (dashed line).

We can also ask about how closely the richness of the clusters traces that of the halo it's matched to, especially given the abundance of blue galaxies in halos, as seen in Fig. 5.1. To this end, we measure the fraction of galaxies, $f_{\rm mem}$, shared by halos and their matched clusters, as well as the relationship between the true richness $N_{\rm gal,true}$, and the observed richness, $N_{\rm gal,obs}$. The results are shown in Fig. 5.3. We measure the same quantities, but where only *red* galaxies are kept for each halo-cluster pair, because this is what the cluster-finder is designed to detect. For each halo and cluster, we measure the median color of the member galaxies, and remove all galaxies bluer than the median color; the results are shown in Fig. 5.4. Note the increase in fractional membership and the decrease in scatter in the $N_{\rm gal,true}$-$N_{\rm gal,obs}$ relation from Fig. 5.3 to Fig. 5.4.

The color-coded richness distribution is shown in Fig. 5.5: cluster whose median color is less than the median color of it's host halo is considered *blue*, while a cluster whose median color is greater than that of its host halo is considered *red*. As shown, there are

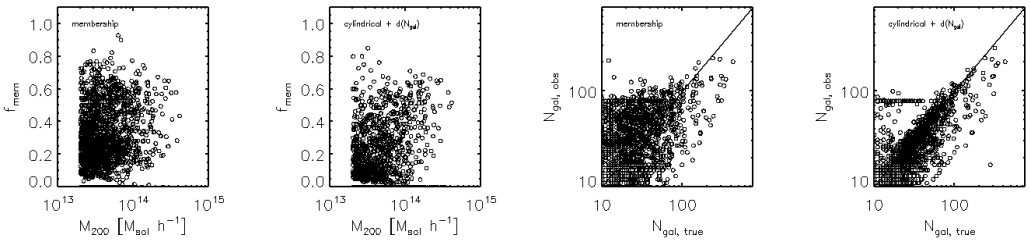

Figure 5.3: Richness diagnostics of clusters for two types of matching scenarios – matching by galaxy membership and by cylindrical volume-richness difference – for clusters matched to halos; membership matching gives the best match by highest overlap of member galaxies. *The two left panels* show the fractional membership, $f_{\rm mem}$, for each type of matching, as a function of mass. Note the high density of points at low fractional membership for both matching scenarios. The *two right panels* compare the richnesses of the best-matched observed cluster and halo – $N_{\rm gal,obs}$ and $N_{\rm gal,true}$, respectively. The solid line shows a $1-1$ correlation. Note the relatively high degree of scatter for membership matching: it becomes asymmetric at high richness ($N_{\rm gal} \sim 100$), when the observed richness clearly begins to under-predict the true richness. For cylindrical matching, scatter is markedly smaller, because we chose the cluster-halo match with the minimum richness difference.

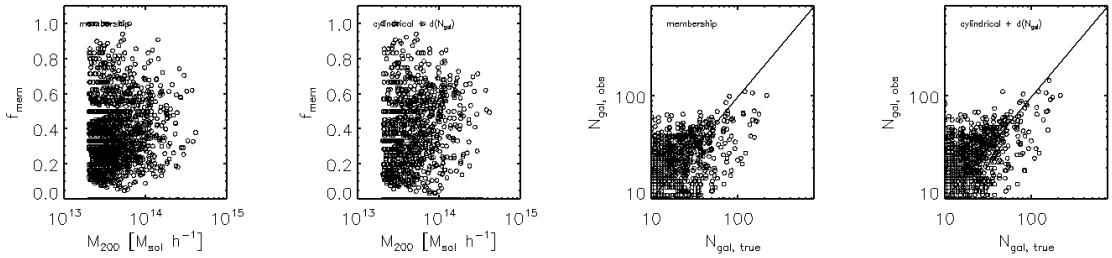

Figure 5.4: Same as Fig. 5.3, but the galaxies have been culled from the clusters and halos by their color; only galaxies that are redder than the cluster or halo median color are retained within the respective object.

many more small blue clusters than red ones; and most of the large, rich clusters are red. This presents a strength and a weakness of our cluster-finder. First, the cluster-finder finds the red ridge-line of most halos, albeit sometimes with high multiplicity and high overlap, but it also finds many distinct ridge-lines within the blue cloud of a single halo. The high multiplicity of clusters for each halo, along with a lack of any post-processing to combine these clusters, all but guarantees a low purity for our halo sample.

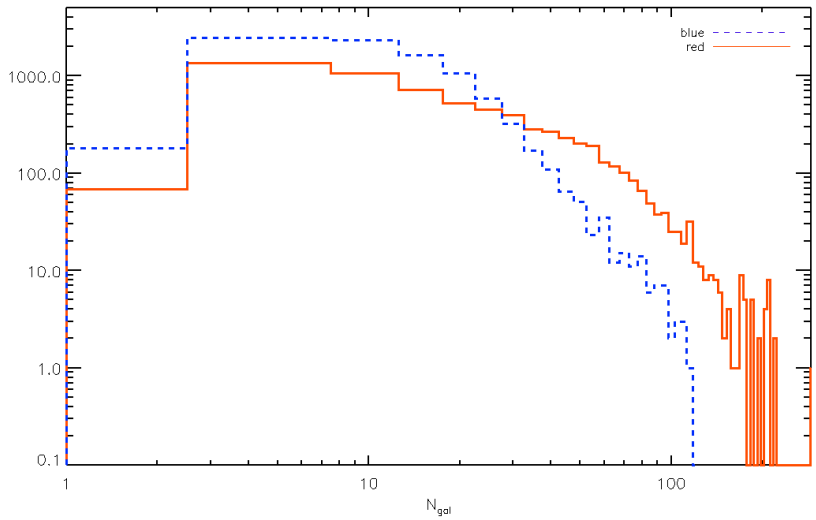

Figure 5.5: Number distribution of richness in the optically selected cluster sample, segregated by mean *cluster* color with respect to the matched median *halo* color. The distribution of blue clusters (dashed, blue line) is steeper than that of the red galaxies (solid, red line) because many more small blue clusters are found within each halo than are red clusters. The red clusters are those that we expect to find along the ridge-line, and comprise most of the halo to which it is matched. The cluster-halo matches were found based on galaxy membership.

5.2 SZ-Selected Clusters

Several methods have been suggested for finding clusters via the SZ signal. Some were tailored to meet specific needs, such as the removal of point sources (*e.g.,* Vale and White, 2005). However, the general method optimal matched filter was introduced to the SZ community by (Haehnelt and Tegmark, 1996; Tegmark and de Oliveira-Costa, 1998), and has proved the most useful, both in single- and multi-frequency incarnations (*e.g.,* Herranz et al., 2002). We refer the reader to Melin et al. (2006), who gives a very brief review of the multitude of cluster-finders – from wavelets to matched filters. The matched filter method has been taken on broadly by the CMB/SZ community, including SPT, and so we use this method here. We first discuss the method and then results from the cluster-finder.

5.2.1 Matched Filter Cluster-finding

Finder Outline

We first briefly review the key elements of the optimal filter construction, but refer the reader to Melin et al. (2006) and Haehnelt and Tegmark (1996) for a derivation and details of implementation. The general principle of the matched filter algorithm is to match expected cluster structure with the closest observation on a map, where the map is assumed to be composed of signal (*i.e.,* temperature, T) and noise ($\mathbf{N}$):

$$\mathbf{M}(\boldsymbol{\theta}) = y_0 g(x) T_{\theta_c}(\boldsymbol{\theta} - \boldsymbol{\theta}_0) + \mathbf{N}(\boldsymbol{\theta}); \tag{5.1}$$

g(x) embodies the frequency dependence of the thermal SZ signal discussed in §2.3 (recall Eqn. 2.16); $\boldsymbol{\theta}$ is the two-dimensional position on the plane of the sky; and $\boldsymbol{\theta}_0$ is the position of the cluster of interest. As discussed previously (§2.2), the known template for the radial distribution of an SZ cluster's decrement, under the assumption of an isothermal ICM, is

the β profile:

$$y(\theta|\beta,\theta_{\rm c}) = y_0\left[1+\left(\frac{\theta}{\theta_{\rm c}}\right)^2\right]^{(1-3\beta)/2}, \tag{5.2}$$

where the core radius $\theta_{\rm c}$ clearly parametrizes the breadth of the profile, while β gives the cuspiness. For future higher resolution surveys, it will be profitable to use a density profile that corresponds to a temperature profile (*e.g.,* Hallman et al., 2007a).

The best estimate of a cluster's central decrement, $\hat{y}_0$, arises from optimally filtering the sky map, $\mathbf{M}$, given models of the noise and the cluster profile. A unique filter is obtained through the requirement of minimizing the variance and requiring the bias between the best estimate and the true value of the detected peak to be zero. The resultant filter is a bandpass filter localized to the scale of the modeled cluster. A frequency-space example is shown in Fig. 5.6. The Matched Filter method relies on the accuracy of the noise model

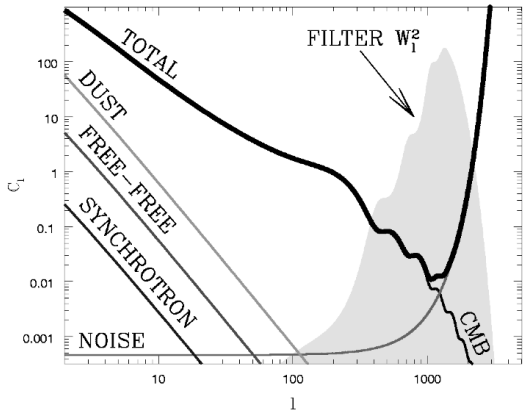

Figure 5.6: Example of a band-pass filter used in SZ source detection – optimized to remove large-scale CMB and 'atmospheric' noise, as well as point sources (Tegmark and de Oliveira-Costa, 1998).

employed within the optimized filter. The noise model, $\mathbf{P}$, is a combination of astrophysical signals (CMB, point sources, dust) and observational noise (beam size, scanning correlation, etc.). In frequency space, the noise power spectrum arises from a combination of the

instrumental and sky noise:

$$P_{ij} = P_i^{\rm noise}\delta_{ij} + B_i(\ell)B_j^{\dagger}(\ell)P_{ij}^{\rm sky}; \tag{5.3}$$

, where the B is the beam, i and j indicate uncorrelated frequency channels, $P^{\rm inst}$ gives the instrumental noise and $P^{\rm sky}$ gives the sky noise, which includes the CMB, the diffuse SZ background, and the point sources (in general, but not in our current study. We compute the CMB power spectrum with CMBFAST (Seljak and Zaldarriaga, 1996) with the simulation's cosmological parameters. The beam is assumed to be Gaussian, with frequency-space character of $B_\ell = {\rm e}^{\theta\ell(\ell+1)/2}$, and of *rms* width, $\theta_B = \theta_{\rm FWHM}/(8{\rm ln}2)^{1/2}$. The diffuse background is constant for all scales. We use just one channel ($\nu = 150GHz$) in our mock observations.

Matched Filter Procedure

Next, we present the application of the matched filter with an algorithm adapted from Melin et al. (2006). An input sky map is first filtered by the optimized two-dimensional β-profile filter, for a series of core radii to produce a filtered map library, $\widetilde{\mathbf{M}}$. Next, a set of smaller maps – just a few times larger than the typical core radius of a cluster – is created: these templates that are likely to match a cluster profile of particular radius; this is the template library. Next, the brightest peak among all the maps of the filtered map library is identified. The filter scale, $\theta_{\rm f}$, of the map with the highest peak is then taken as the core radius of the cluster identified by its peak value, $\hat{y}_0$. One of the smaller templates is then scaled by this decrement and removed from the map library. This process is repeated until no clusters above a prescribed certain signal-to-noise ratio remain.

1. Filter the sky map for each filter frequency, θ_f, to obtain a set of n_{θ_f} maps, $\widetilde{\mathbf{M}}$.

2. Create a set of cluster templates, modeled on the β profile, for a range of core radii.

3. Filter each cluster template at the set of filter frequencies, to obtain a set of $n_{\theta_f} \times n_{\theta_c}$ maps.

4. Find clusters:

   (a) Find the brightest pixel among *any* of the filtered maps, $\widetilde{\mathbf{M}}$. The decrement of this brightest pixel must be higher than the noise variance by a preset threshold factor $q_{\rm th}$, such that $y_0 \geq q_{\rm th}\,\sigma_{\theta_c}$. The decrement is the estimated decrement for this cluster. The filter scale of the map from which this pixel is selected gives the core radius of the selected cluster.

   (b) Scale this template by the estimated central decrement, and integrate over the extent to obtain the integrated cluster flux.

   (c) Add cluster to list

5. Select from the template library those templates with core radius, $\tilde{\theta}$, that match that of the found cluster; in Step 3, this template was also filtered over every filter scale found in the filtered maps.

6. Scale this template by the decrement of the found cluster.

7. Remove the scaled template (and thus the detected cluster) from all filtered maps $\widetilde{\mathbf{M}}$.

8. return to Step 4 and repeat until no more pixels exceed the signal-to-noise threshold, $q_{\rm th}$

5.2.2 Cluster Sample Diagnostics and SZ-Optical Cross-Correlation

In this section, we briefly discuss the ability of the cluster-finder to recover the intrinsic halo population. The pixel size for our map is 0.25', and we choose $\beta = 1$ for all cluster

template profiles. The noise included in the SZ map is only astrophysical noise from the CMB and instrumental white noise of 6μK, about one-third that of SPT. There were fewer than 100 clusters detected above $S/N = 4$ in the full sample. We measure the completeness (Fig. 5.7) by matching clusters to halos within each halo's known angular extent. The completeness declines sharply near $2 \times 10^{14}\ h^{-1}\ \mathrm{M}_{\odot}$, and is low ($< 5\%$) at all epochs. This is driven by the low beam resolution of 1' and the instrumental noise. We

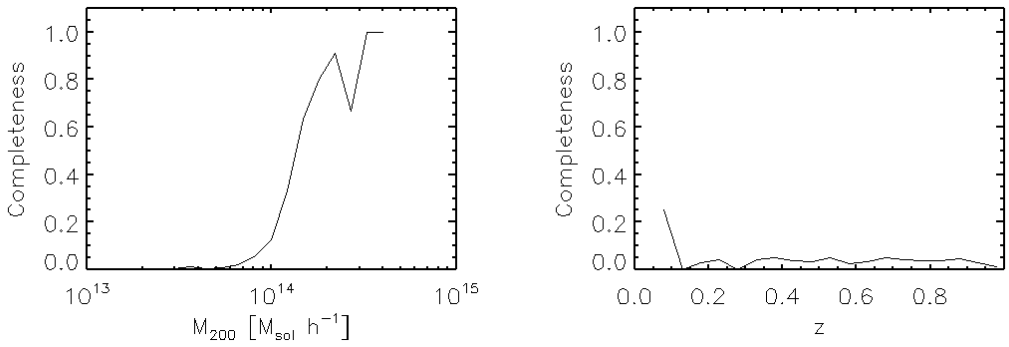

Figure 5.7: Completeness as a function of mass and redshift for the SZ-selected cluster population.

measure the purity (shown in Fig. 5.8) by matching halos to clusters within the measured core radius of the observed cluster and within a 4' aperture. The purity is moderate on average with large fluctuations for the range of fluxes and S/N ratios, except at high flux. We can see more clearly the cause of this impurity at high flux in Fig. 5.8, where the sky map is overlaid with the 10 highest-flux clusters (open circles) and the 10 most massive halos in the MGSVSS (open diamonds). If we include less massive halos, then all but three of the detected clusters are matched. There are two potential explanations for some of these highest-flux clusters not being matched to halos. First, there could be a large amount of filamentary gas along these lines of sight, although that should be a rarer phenomenon. The other, more likely, potential cause is that halo finder did not find some of the halos. We will investigate this further. To measure the false-positive rate that could be caused

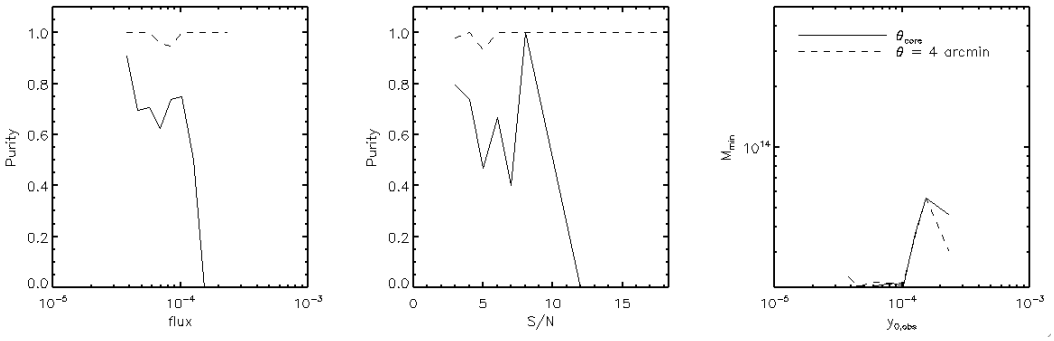

Figure 5.8: Purity in the SZ-selected cluster population as a function of the central flux and S/N, and the minimum mass detectable as a function of the observed central flux. Halos have been matched to each observed cluster, within the observed core radius, θ_{core}, (solid line) and within a constant aperture of $4'$ (dashed line).

by CMB fluctuations alone, we also run the cluster finder on an identical sky without the simulation (*i.e.,* including CMB and white noise only). For detections of $S/N \geq 3$, there are 48 false detections, and for $S/N \geq 4$, there are two false detections – all with $\theta_c \geq 3.2$; this scale is larger than the typical cluster, as expected if CMB fluctuations are the cause of the detection. Therefore, we will not include in our final sample any of our cluster detections for $S/N < 4$.

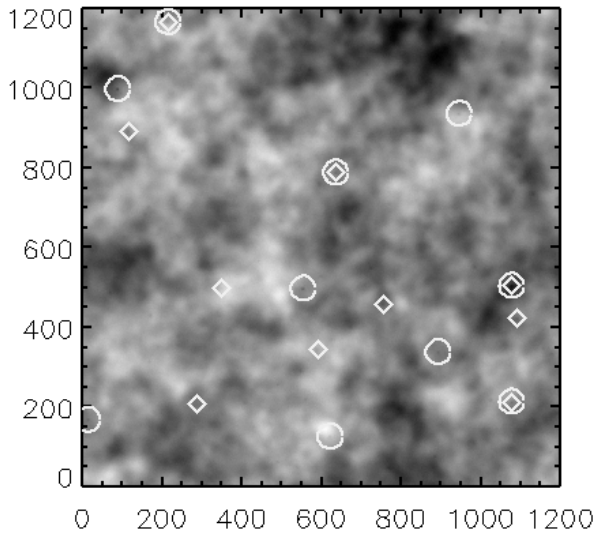

Figure 5.9: Map of SZ sky with CMB, white noise and SZ signal, along with the top-10-S/N SZ-selected clusters (open circles) and the top-10 most massive halos (open diamonds) in the MGS.

Finally, we measure the richness of the SZ-detected clusters (Fig. 5.10) by finding the richest optical cluster within the core radius of each SZ-selected cluster. The hard threshold on the S/N ratio may inhibit observation of low-S/N objects. Also the small observational volume provides fewer bright clusters. These two factors can contribute to the extraordinary flatness in the observed scaling relations. This issue begs further examination.

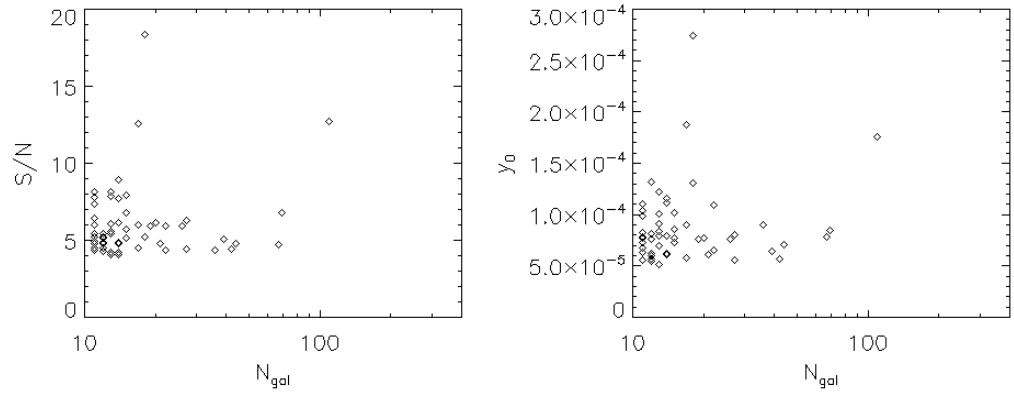

Figure 5.10: Correlation between optical richness, N_{gal} and SZ signal-to-noise and central decrement.

5.3 Discussion and Conclusion

In this chapter, we performed a preliminary set of cluster-finder exercises in the SZ sky map and optical galaxy catalogue of the MGSVSS, along with a very basic cross-correlation measurement of the richness-decrement relation. The optical cluster-finder is based on the detection of the cluster red sequence and uses bright central galaxies as points around which to search for cluster members. Our algorithm has fewer than 10 tunable parameters, but lacks flexibility sufficient to eliminate projection and consistently select the brightest galaxy as the cluster center; moreover, the large abundance of blue galaxies increases the number of clusters found for each halo: several blue ridge-lines are found in each halo. Nevertheless, the completeness for our red sequence cluster-finder is above 80% for all halo

masses and at all but the highest redshifts.

The SZ cluster-finder is a matched filter finder, and we assume the cluster-finding to be insensitive to variations in most of the tunable parameters – *i.e.,* the power of the β profile; we also assume an instrument noise level at 1/3 that of the actual SPT noise in order to obtain a sufficiently large test sample. The completeness in our SZ cluster sample remain above 80% for halo masses above $2 \times 10^{14}\ h^{-1}\ \mathrm{M}_{\odot}$, but stays below 10% at nearly all redshifts. This is lower than expected, but not extraordinarily so: SZ-detected clusters contain no redshift information and halos within the beam and along the line of sight all contribute to the same observed cluster. The SZ-optical cross-correlation test results in an extremely flat scaling relation between richness and SZ decrement: we initially attribute this to a S/N limits at the low-richness end, along with a lack of bright clusters at the high-richness end; however, it is also likely due to high scatter in the richness with halo mass, as well as the initial bug in the halo finder.

In the next round of cluster-finding in the MGSVSS, I intend to develop a suite of improvements for these cluster-finders and the cross-correlation process. We will further refine the parameter choices of the optical cluster-finder; for example, some of them should evolve with redshift. Also, we intend to include observation-induced errors, like random error on the redshifts. For the final version of this work, me may in fact use a more thoroughly tested optical cluster-finder, such as maxBCG or one of its derivatives. On the SZ side, we intend to more completely characterize the line-of-sight contamination caused both by halos and by extra-cluster gas. Also, I will investigate the cross-correlation of clusters on a cluster-by-cluster and halo-by-halo basis to characterize the fidelity of each SZ-optical combination.

CHAPTER VI

Summary and Conclusions

In this dissertation, I focus on the study of galaxy cluster populations in observational, theoretical, and simulated environments, with the aim of informing constraints on the dark energy equation of state through multi-wavelength analyses of galaxy cluster populations. In particular, I demonstrate the utility of a multi-variate approach to cluster population analysis in addressing confusion born from observational biases and a naive approach to scaling relation deconstruction. Also, I have created a simulated sky survey that will be used to refine our cluster-finding methods in preparation for joint cluster surveys: we have performed preliminary cluster-finding on our simulated skies to begin investigations of cross-correlating SZ and optical signals in the same sky. With just a little further refinement, the MGSVSS will be the most sophisticated multi-wavelength (*i.e.,* SZ-optical) simulated sky survey to date: it includes physics from a gasdynamic simulation, several types and levels of noise in the SZ sky, as well as state-of-the-art galaxy population models.

The work following this dissertation will build upon each part, from the multi-variate analysis to cross-correlation. First, I intend to follow up on measuring the intrinsic correlation between X-ray luminosity and temperature in the HIFLUGCS cluster sample and in the Millennium Gas Simulation. The largest next steps, however, will be taken in the arena of joint cluster finding with SZ and optical signatures of clusters. I will enlarge

the field of view of the MGSVSS, refine the halo catalogue, and understand in detail the galaxy population within halos and in the field of the MGSVSS lightcone; we will use a more thoroughly calibrated optical cluster finder or refine our simple red sequence finder to balance completeness and multiplicity. Also, I will add more sophisticated types of noise to the SZ sky map, and measure the sensitivity of each aspect of the matched filter cluster finder to the tunable parameters. Finally, we will explore methods of joint cluster selection in an effort to recover the optimal cluster catalogue for dark energy science.

Bibliography

Abell, G. O. The distribution of rich clusters of galaxies. *Astrophysical Journal Supplement*, 3:211, 1958. doi:10.1086/190036.

Adams, F. C., Bloch, A. M., Butler, S. C., Druce, J. M. and Ketchum, J. A. Orbital instabilities in a triaxial cusp potential. *The Astrophysical Journal*, 670:1027, 2007. doi:10.1086/522581.

Allen, S. W., Schmidt, R. W., Ebeling, H., Fabian, A. C. and Speybroeck, L. V. Constraints on dark energy from chandra observations of the largest relaxed galaxy clusters. *Monthly Notices of the Royal Astronomical Society*, 353:457, 2004. doi:10.1111/j.1365-2966.2004.08080.x.

Allen, S. W., Schmidt, R. W. and Fabian, A. C. Cosmological constraints from the x-ray gas mass fraction in relaxed lensing clusters observed with chandra. *Monthly Notices of the Royal Astronomical Society*, 334:L11, 2002. doi:10.1046/j.1365-8711.2002.05601.x.

Andersson, K. et al. X-ray properties of the first sze-selected galaxy cluster sample from the south pole telescope. *eprint arXiv*, 1006:3068, 2010. 28 pages, 19 figures, submitted to ApJ.

Annis, J. et al. The maxbcg technique for finding galaxy clusters in sdss data. *American Astronomical Society*, 195:1391, 1999.

Arnaud, K. A. XSPEC: The First Ten Years. In G. H. Jacoby & J. Barnes, editor, *Astronomical Data Analysis Software and Systems V*, volume 101 of *Astronomical Society of the Pacific Conference Series*, pages 17–+. 1996.

Arnaud, M. and Evrard, A. E. The $L_{\rm x} - T$ relation and intracluster gas fractions of x-ray clusters. *Monthly Notices of the Royal Astronomical Society*, 305:631, 1999. doi:10.1046/j.1365-8711.1999.02442.x.

Bahcall, N. A., Fan, X. and Cen, R. Constraining omega with cluster evolution. *Astrophysical Journal Letters v.485*, 485:L53, 1997. doi:10.1086/310814.

Bahcall, N. A. et al. A merged catalog of clusters of galaxies from early sloan digital sky survey data. *The Astrophysical Journal Supplement Series*, 148:243, 2003. doi:10.1086/377167.

Balogh, M. L., Babul, A., Voit, G. M., McCarthy, I. G., Jones, L. R., Lewis, G. F. and Ebeling, H. An analytic investigation of the scatter in the integrated x-ray properties of galaxy groups and clusters. *Monthly Notices of the Royal Astronomical Society*, 366:624, 2006. doi:10.1111/j.1365-2966.2005.09917.x.

Bardeen, J. M., Bond, J. R., Kaiser, N. and Szalay, A. S. The statistics of peaks of gaussian random fields. *Astrophysical Journal*, 304:15, 1986. doi:10.1086/164143.

Battaglia, N., Bond, J. R., Pfrommer, C., Sievers, J. L. and Sijacki, D. Simulations of the sunyaev-zel'dovich power spectrum with agn feedback. *eprint arXiv*, 1003:4256, 2010.

Becker, M. R. et al. The mean and scatter of the velocity dispersion-optical richness relation for maxbcg galaxy clusters. *The Astrophysical Journal*, 669:905, 2007. doi:10.1086/521920. (c) 2007: The American Astronomical Society.

Bekenstein, J. D. An alternative to the dark matter paradigm: relativistic mond gravita-

tion. *eprint arXiv*, page 12652, 2004.

Benson, A. J., Reichardt, C. and Kamionkowski, M. Statistics of sunyaev-zel'dovich cluster surveys. *Monthly Notices of the Royal Astronomical Society*, 331:71, 2002. doi:10.1046/j.1365-8711.2002.05139.x.

Benson, B. A., Church, S. E., Ade, P. A. R., Bock, J. J., Ganga, K. M., Henson, C. N. and Thompson, K. L. Measurements of sunyaev-zel'dovich effect scaling relations for clusters of galaxies. *The Astrophysical Journal*, 617:829, 2004. doi:10.1086/425677.

Bergmann, P. G. Comments on the scalar-tensor theory. *International Journal of Theoretical Physics*, 1:25, 1968. doi:10.1007/BF00668828.

Berlind, A. A. and Weinberg, D. H. The halo occupation distribution: Toward an empirical determination of the relation between galaxies and mass. *The Astrophysical Journal*, 575:587, 2002. doi:10.1086/341469.

Bertschinger, E. Self-similar secondary infall and accretion in an einstein-de sitter universe. *Astrophysical Journal Supplement Series (ISSN 0067-0049)*, 58:39, 1985. doi:10.1086/191028.

Bialek, J. J., Evrard, A. E. and Mohr, J. J. Effects of preheating on x-ray scaling relations in galaxy clusters. *The Astrophysical Journal*, 555:597, 2001. doi:10.1086/321507. (c) 2001: The American Astronomical Society.

Blanton, E. L., Sarazin, C. L., McNamara, B. R. and Wise, M. W. Chandra observation of the radio source/x-ray gas interaction in the cooling flow cluster abell 2052. *The Astrophysical Journal*, 558:L15, 2001. doi:10.1086/323269.

Blanton, M. R. et al. The galaxy luminosity function and luminosity density at redshift z = 0.1. *The Astrophysical Journal*, 592:819, 2003. doi:10.1086/375776.

Bode, P., Ostriker, J. P., Weller, J. and Shaw, L. Accurate realizations of the ionized gas in galaxy clusters: Calibrating feedback. *The Astrophysical Journal*, 663:139, 2007. doi:10.1086/518432.

Boehringer, H. et al. Unveiling the structure of galaxy clusters with combined eso-vlt wfi, and xmm-newton observations. *The Messenger*, 123:49, 2006.

Böhringer, H. et al. The rosat-eso flux-limited x-ray (reflex) galaxy cluster survey. iv. the x-ray luminosity function. *The Astrophysical Journal*, 566:93, 2002. doi:10.1086/338072.

Böhringer, H. et al. Substructure of the galaxy clusters in the rexcess sample: observed statistics and comparison to numerical simulations. *Astronomy and Astrophysics*, 514:32, 2010. doi:10.1051/0004-6361/200913911.

Bolzonella, M., Miralles, J.-M. and Pelló, R. Photometric redshifts based on standard sed fitting procedures. *Astronomy and Astrophysics*, 363:476, 2000.

Bond, J. R., Kofman, L. and Pogosyan, D. How filaments of galaxies are woven into the cosmic web. *Nature*, 380:603, 1996. doi:10.1038/380603a0.

Bond, J. R. and Myers, S. T. The peak-patch picture of cosmic catalogs. i. algorithms. *Astrophysical Journal Supplement v.103*, 103:1, 1996. doi:10.1086/192267.

Bower, R. G., Lucey, J. R. and Ellis, R. S. Precision photometry of early-type galaxies in the coma and virgo clusters: A test of the universality of the colour-magnitude relation.

i - the data. ii. analysis. *Royal Astronomical Society*, 254:589, 1992.

Bryan, G. L., Abel, T. and Norman, M. L. Achieving extreme resolution in numerical cosmology using adaptive mesh refinement: Resolving primordial star formation. *eprint arXiv*, page 12089, 2001.

Buote, D. A. and Tsai, J. C. Quantifying the morphologies and dynamical evolution of galaxy clusters. i. the method. *Astrophysical Journal v.452*, 452:522, 1995. doi: 10.1086/176326.

Busha, M. T., Adams, F. C., Wechsler, R. H. and Evrard, A. E. Future evolution of structure in an accelerating universe. *arXiv*, astro-ph, 2003.

Carlstrom, J. E., Holder, G. P. and Reese, E. D. Cosmology with the sunyaev-zel'dovich effect. *Annual Review of Astronomy and Astrophysics*, 40:643, 2002. doi: 10.1146/annurev.astro.40.060401.093803.

Carlstrom, J. E. et al. The 10 meter south pole telescope. *eprint arXiv*, 0907:4445, 2009. 42 pages, 12 figures, submitted to PASP.

Carrera, F. J. et al. The xmm-newton serendipitous survey. iii. the axis x-ray source counts and angular clustering. *Astronomy and Astrophysics*, 469:27, 2007. doi:10.1051/0004-6361:20066271.

Cavaliere, A. and Fusco-Femiano, R. X-rays from hot plasma in clusters of galaxies. *Astronomy and Astrophysics*, 49:137, 1976. A&AA ID. AAA017.161.005.

Chang, C. L. et al. Spt-sz: a sunyaev-zepdovich survey for galaxy clusters. *The Thirteenth International Workshop on Low Temperature Detectors-LTD13. AIP Conference Proceedings*, 1185:475, 2009. doi:10.1063/1.3292381.

Chaudhuri, A. and Majumdar, S. Sunyaev-zel'dovich scaling relations from a simple phenomenological model for galaxy clusters. *arXiv*, astro-ph.CO, 2010. 6 pages, submitted to ApJL.

Cohn, J. D., Evrard, A. E., White, M., Croton, D. and Ellingson, E. Red-sequence cluster finding in the millennium simulation. *Monthly Notices of the Royal Astronomical Society*, 382:1738, 2007. doi:10.1111/j.1365-2966.2007.12479.x.

Cohn, J. D. and White, M. Issues in joint sz and optical cluster finding. *Monthly Notices of the Royal Astronomical Society*, 393:393, 2009. doi:10.1111/j.1365-2966.2008.14215.x.

Collister, A. A. and Lahav, O. Annz: Estimating photometric redshifts using artificial neural networks. *The Publications of the Astronomical Society of the Pacific*, 116:345, 2004. doi:10.1086/383254.

Connolly, A. J., Csabai, I., Szalay, A. S., Koo, D. C., Kron, R. G. and Munn, J. A. Slicing through multicolor space: Galaxy redshifts from broadband photometry. *Astronomical Journal v.110*, 110:2655, 1995. doi:10.1086/117720.

Conroy, C. and Ostriker, J. P. Thermal balance in the intracluster medium: Is agn feedback necessary? *The Astrophysical Journal*, 681:151, 2008. doi:10.1086/587861.

Cooray, A. R. An sz temperature decrement-x-ray luminosity relation for galaxy clusters. *Monthly Notices*, 307:841, 1999. doi:10.1046/j.1365-8711.1999.02660.x.

Corless, V. L. and King, L. J. A statistical study of weak lensing by triaxial dark matter

haloes: consequences for parameter estimation. *Monthly Notices of the Royal Astronomical Society*, 380:149, 2007. doi:10.1111/j.1365-2966.2007.12018.x.

Culverhouse, T. L. et al. Galaxy clusters at z¿=1: Gas constraints from the sunyaev-zel'dovich array. *eprint arXiv*, 1007:2853, 2010. 6 pages, 2 figures, submitted on ApJL.

Cunha, C. Cross-calibration of cluster mass observables. *Physical Review D*, 79:63009, 2009. doi:10.1103/PhysRevD.79.063009. (c) 2009: The American Physical Society.

da Silva, A. C., Barbosa, D., Liddle, A. R. and Thomas, P. A. Hydrodynamical simulations of the sunyaev-zel'dovich effect: the kinetic effect. *Monthly Notices of the Royal Astronomical Society*, 326:155, 2001. doi:10.1046/j.1365-8711.2001.04580.x.

Dai, X., Kochanek, C. S. and Morgan, N. D. The x-ray properties of optically selected galaxy clusters. *The Astrophysical Journal*, 658:917, 2007. doi:10.1086/509651.

Diego, J. M. and Partridge, B. The sunyaev-zel'dovich effect in wilkinson microwave anisotropy probe data. *Monthly Notices of the Royal Astronomical Society*, 402:1179, 2010. doi:10.1111/j.1365-2966.2009.15949.x.

Donahue, M. et al. Distant cluster hunting: A comparison between the optical and x-ray luminosity functions from an optical/x-ray joint survey. *The Astrophysical Journal*, 552:L93, 2001. doi:10.1086/320334.

Dressler, A. Galaxy morphology in rich clusters - implications for the formation and evolution of galaxies. *Astrophysical Journal*, 236:351, 1980. doi:10.1086/157753. A&AA ID. AAA027.158.034.

Dressler, A. et al. Evolution since z = 0.5 of the morphology-density relation for clusters of galaxies. *Astrophysical Journal v.490*, 490:577, 1997. doi:10.1086/304890.

Dunsby, P. K. S., Elizalde, E., Goswami, R., Odintsov, S. and Saez-Gomez, D. cdm universe in f(r) gravity. *Physical Review D*, 82:23519, 2010. doi:10.1103/PhysRevD.82.023519. (c) 2010: The American Physical Society.

Dvali, G., Gabadadze, G. and Porrati, M. 4d gravity on a brane in 5d minkowski space. *Physics Letters B*, 485:208, 2000. doi:10.1016/S0370-2693(00)00669-9.

Ebeling, H., Edge, A. C., Bohringer, H., Allen, S. W., Crawford, C. S., Fabian, A. C., Voges, W. and Huchra, J. P. The rosat brightest cluster sample - i. the compilation of the sample and the cluster log n-log s distribution. *Monthly Notices of the Royal Astronomical Society*, 301:881, 1998. doi:10.1046/j.1365-8711.1998.01949.x.

Eisenstein, D. J. and Hu, W. Baryonic features in the matter transfer function. *Astrophysical Journal v.496*, 496:605, 1998. doi:10.1086/305424.

Evrard, A. E. Real or virtual large-scale structure? *Proceedings of the National Academy of Sciences of the United States of America*, 96:4228, 1999.

Evrard, A. E. Virtual galaxy formation. *Philosophical Transactions of the Royal Society of London*, 358:2143, 2000. doi:10.1098/rsta.2000.0636.

Evrard, A. E. et al. Galaxy clusters in hubble volume simulations: Cosmological constraints from sky survey populations. *The Astrophysical Journal*, 573:7, 2002. doi:10.1086/340551.

Evrard, A. E. et al. Virial scaling of massive dark matter halos: Why clusters prefer a high

normalization cosmology. *The Astrophysical Journal*, 672:122, 2008. doi:10.1086/521616.

Fabbri, R. Spectrum of the sunyaev-zel'dovich effect for high electron temperatures. *Astrophysics and Space Science*, 77:529, 1981. doi:10.1007/BF00649478. A&AA ID. AAA029.066.054.

Fairley, B. W., Jones, L. R., Scharf, C., Ebeling, H., Perlman, E., Horner, D., Wegner, G. and Malkan, M. The warps survey - iv. the x-ray luminosity-temperature relation of high-redshift galaxy clusters. *Monthly Notices of the Royal Astronomical Society*, 315:669, 2000. doi:10.1046/j.1365-8711.2000.03512.x.

Fixsen, D. J. et al. Cosmic microwave background dipole spectrum measured by the cobe firas instrument. *The Astrophysical Journal*, 420:445, 1994. doi:10.1086/173575.

Folkes, S. et al. The 2df galaxy redshift survey: spectral types and luminosity functions. *Monthly Notices*, 308:459, 1999. doi:10.1046/j.1365-8711.1999.02721.x.

Frenk, C. S. et al. The santa barbara cluster comparison project: A comparison of cosmological hydrodynamics solutions. *The Astrophysical Journal*, 525:554, 1999. doi:10.1086/307908.

Friedman, R. B. et al. Small angular scale measurements of the cosmic microwave background temperature power spectrum from quad. *The Astrophysical Journal Letters*, 700:L187, 2009. doi:10.1088/0004-637X/700/2/L187.

Fukugita, M., Ichikawa, T., Gunn, J. E., Doi, M., Shimasaku, K. and Schneider, D. P. The sloan digital sky survey photometric system. *Astronomical Journal v.111*, 111:1748, 1996. doi:10.1086/117915.

Gal, R. R. Optical detection of clusters of galaxies. *A Pan-Chromatic View of Clusters of Galaxies and the Large-Scale Structure*, 740:119, 2008.

Gal, R. R., Lopes, P. A. A., de Carvalho, R. R., Kohl-Moreira, J. L., Capelato, H. V. and Djorgovski, S. G. The northern sky optical cluster survey. iii. a cluster catalog covering pi steradians. *The Astronomical Journal*, 137:2981, 2009. doi:10.1088/0004-6256/137/2/2981.

Gazzola, L. and Pearce, F. R. A heating model for the millennium gas run. *arXiv*, astro-ph, 2006.

Gerdes, D. W., Sypniewski, A. J., McKay, T. A., Hao, J., Weis, M. R., Wechsler, R. H. and Busha, M. T. Arborz: Photometric redshifts using boosted decision trees. *The Astrophysical Journal*, 715:823, 2010. doi:10.1088/0004-637X/715/2/823.

Gerke, B. F. et al. The deep2 galaxy redshift survey: First results on galaxy groups. *The Astrophysical Journal*, 625:6, 2005. doi:10.1086/429579.

Gladders, M. D., Lopez-Cruz, O., Yee, H. K. C. and Kodama, T. The slope of the cluster elliptical red sequence: A probe of cluster evolution. *Astrophysical Journal v.501*, 501:571, 1998. doi:10.1086/305858.

Gladders, M. D. and Yee, H. K. C. A new method for galaxy cluster detection. i. the algorithm. *The Astronomical Journal*, 120:2148, 2000. doi:10.1086/301557.

Gladders, M. D. and Yee, H. K. C. The red-sequence cluster survey. i. the survey and cluster catalogs for patches rcs 0926+37 and rcs 1327+29. *The Astrophysical Journal Supplement Series*, 157:1, 2005. doi:10.1086/427327.

Goto, T. et al. The cut-and-enhance method: Selecting clusters of galaxies from the sloan digital sky survey commissioning data. *The Astronomical Journal*, 123:1807, 2002. doi: 10.1086/339303.

Green, P. et al. The chandra multiwavelength project: Optical follow-up of serendipitous chandra sources. *The Astrophysical Journal Supplement Series*, 150:43–43–71–71, 1. doi:doi:10.1086/379818.

Haehnelt, M. G. and Tegmark, M. Using the kinematic sunyaev-zeldovich effect to determine the peculiar velocities of clusters of galaxies. *Monthly Notices of the Royal Astronomical Society*, 279:545, 1996.

Hallman, E. J., Burns, J. O., Motl, P. M. and Norman, M. L. The -model problem: The incompatibility of x-ray and sunyaev-zeldovich effect model fitting for galaxy clusters. *The Astrophysical Journal*, 665:911, 2007a. doi:10.1086/519447. (c) 2007: The American Astronomical Society.

Hallman, E. J., Motl, P. M., Burns, J. O. and Norman, M. L. Challenges for precision cosmology with x-ray and sunyaev-zeldovich effect gas mass measurements of galaxy clusters. *The Astrophysical Journal*, 648:852, 2006. doi:10.1086/505317.

Hallman, E. J., O'Shea, B. W., Burns, J. O., Norman, M. L., Harkness, R. and Wagner, R. The santa fe light cone simulation project. i. confusion and the warm-hot intergalactic medium in upcoming sunyaev-zel'dovich effect surveys. *The Astrophysical Journal*, 671:27, 2007b. doi:10.1086/522912. (c) 2007: The American Astronomical Society.

Halverson, N. W. et al. Sunyaev-zel'dovich effect observations of the bullet cluster (1e 0657-56) with apex-sz. *The Astrophysical Journal*, 701:42, 2009. doi:10.1088/0004-637X/701/1/42.

Hansen, S. M., McKay, T. A., Wechsler, R. H., Annis, J., Sheldon, E. S. and Kimball, A. Measurement of galaxy cluster sizes, radial profiles, and luminosity functions from sdss photometric data. *The Astrophysical Journal*, 633:122, 2005. doi:10.1086/444554.

Hansen, S. M., Sheldon, E. S., Wechsler, R. H. and Koester, B. P. The galaxy content of sdss clusters and groups. *The Astrophysical Journal*, 699:1333, 2009. doi:10.1088/0004-637X/699/2/1333.

Hao, J. et al. Precision measurements of the cluster red sequence using an error-corrected gaussian mixture model. *The Astrophysical Journal*, 702:745, 2009. doi: 10.1088/0004-637X/702/1/745.

Harrison, E. R. Fluctuations at the threshold of classical cosmology. *Phys. Rev. D*, 1(10):2726–2730, 1970. doi:10.1103/PhysRevD.1.2726.

Hartle, J. B. and Hawking, S. W. Wave function of the universe. *Physical Review D (Particles and Fields)*, 28:2960, 1983. doi:10.1103/PhysRevD.28.2960.

Hartley, W. G., Gazzola, L., Pearce, F. R., Kay, S. T. and Thomas, P. A. Nature versus nurture: The curved spine of the galaxy cluster x-ray luminosity - temperature relation. *arXiv*, astro-ph, 2007. 8 pages, 7 figures, submitted to MNRAS.

Hernández-Monteagudo, C., Verde, L., Jimenez, R. and Spergel, D. Correlation properties of the kinematic sunyaev-zel'dovich effect and implications for dark energy. *The Astrophysical Journal*, 643:598–598–615–615, 2006. doi:doi:10.1086/503190.

Herranz, D., Sanz, J. L., Hobson, M. P., Barreiro, R. B., Diego, J. M., Martínez-González, E. and Lasenby, A. N. Filtering techniques for the detection of sunyaev-zel'dovich clusters in multifrequency maps. *Monthly Notice of the Royal Astronomical Society*, 336:1057, 2002. doi:10.1046/j.1365-8711.2002.05704.x. (c) RAS.

Hildebrandt, H. et al. Phat: Photo-z accuracy testing. *eprint arXiv*, 1008:658, 2010. 22 pages, 15 figures, A&A in press.

Hincks, A. D. et al. The Atacama Cosmology Telescope (ACT): Beam profiles and first sz cluster maps. *eprint arXiv*, 0907:461, 2009.

Holder, G. Gilbert Holder; Galaxy Clusters: `http://www.physics.mcgill.ca/~holder/research.html`. 2010.

Holder, G., Haiman, Z. and Mohr, J. J. Constraints on m, , and 8 from galaxy cluster redshift distributions. *The Astrophysical Journal*, 560:L111, 2001. doi:10.1086/324309.

Holder, G. P. Measuring cluster peculiar velocities and temperatures at centimeter and millimeter wavelengths. *The Astrophysical Journal*, 602:18, 2004. doi:10.1086/380916.

Holder, G. P. and Carlstrom, J. E. Understanding cluster gas evolution and fine-scale cosmic microwave background anisotropy with deep sunyaev-zeldovich effect surveys. *The Astrophysical Journal*, 558:515, 2001. doi:10.1086/322313.

Holder, G. P., McCarthy, I. G. and Babul, A. The sunyaev-zeldovich background. *Monthly Notices of the Royal Astronomical Society*, 382:1697, 2007. doi:10.1111/j.1365-2966.2007.12430.x.

Holmberg, E. On the clustering tendencies among the nebulae. ii. a study of encounters between laboratory models of stellar systems by a new integration procedure. *Astrophysical Journal*, 94:385, 1941. doi:10.1086/144344.

Hu, W. Acceleration from modified gravity: Lessons from worked examples. *Nuclear Physics B Proceedings Supplements*, 194:230, 2009. doi:10.1016/j.nuclphysbps.2009.07.086.

Hubble, E. P. Realm of the nebulae. *Realm of the Nebulae*, 1936.

Iliev, I. T., Pen, U.-L., Bond, J. R., Mellema, G. and Shapiro, P. R. The kinetic sunyaev-zel'dovich effect from radiative transfer simulations of patchy reionization. *The Astrophysical Journal*, 660:933, 2007. doi:10.1086/513687.

Ivezic, Z., Tyson, J. A., Allsman, R., Andrew, J., Angel, R. and for the LSST Collaboration. Lsst: from science drivers to reference design and anticipated data products. *eprint arXiv*, 0805:2366, 2008.

Jarosik, N. et al. Seven-year wilkinson microwave anisotropy probe (wmap) observations: Sky maps, systematic errors, and basic results. *eprint arXiv*, 1001:4744, 2010.

Jelić, V. et al. A cross-correlation study between the cosmological 21 cm signal and the kinetic sunyaev-zel'dovich effect. *Monthly Notices of the Royal Astronomical Society*, 402:2279–2279–2290–2290, 2003. doi:doi:10.1111/j.1365-2966.2009.16086.x.

Jenkins, A. et al. Evolution of structure in cold dark matter universes. *Astrophysical Journal v.499*, 499:20, 1998. doi:10.1086/305615.

Jenkins, A. et al. The mass function of dark matter haloes. *Monthly Notices of the Royal*

Astronomical Society, 321:372, 2001. doi:10.1046/j.1365-8711.2001.04029.x.

Johnston, D. E., Sheldon, E. S., Tasitsiomi, A., Frieman, J. A., Wechsler, R. H. and McKay, T. A. Cross-correlation lensing: Determining galaxy and cluster mass profiles from statistical weak-lensing measurements. *The Astrophysical Journal*, 656:27, 2007. doi:10.1086/510060. (c) 2007: The American Astronomical Society.

Juin, J.-B., Pires, S., Yvon, D., Refregier, A., Yeche, C., Moudden, Y., Anthoine, S. and Pierpaoli, E. Sunyaev zel'dovich galaxy cluster wide surveys for cosmology. *VI Reunion Anual Sociedad Chilena de Astronomia (SOCHIAS)*, page 23, 2007.

Kaiser, N. Evolution and clustering of rich clusters. *Royal Astronomical Society*, 222:323, 1986.

Kellogg, E., Gursky, H., Tananbaum, H., Giacconi, R. and Pounds, K. The extended x-ray source at m87. *Astrophysical Journal*, 174:L65, 1972. doi:10.1086/180950. A&AA ID. AAA007.142.108.

Kim, D. et al. Chandra multiwavelength project. i. first x-ray source catalog. *The Astrophysical Journal Supplement Series*, 150:19–19–41–41, 1a. doi:doi:10.1086/379819.

Kim, R. et al. Detecting clusters of galaxies in the sloan digital sky survey. i. monte carlo comparison of cluster detection algorithms. *The Astronomical Journal*, 123:20–20–36–36, 1b. doi:doi:10.1086/324727.

Kim, R. S. J. et al. Detecting clusters of galaxies in the sloan digital sky survey. i. monte carlo comparison of cluster detection algorithms. *The Astronomical Journal*, 123:20, 2002. doi:10.1086/324727.

King, I. R. The structure of star clusters. iii. some simple dynamical models. *Astronomical Journal*, 71:64, 1966. doi:10.1086/109857.

Kitzbichler, M. G. and White, S. D. M. The high-redshift galaxy population in hierarchical galaxy formation models. *Monthly Notices of the Royal Astronomical Society*, 376:2, 2007. doi:10.1111/j.1365-2966.2007.11458.x.

Kleinmann, S. G. et al. The two micron all sky survey. *Astrophysics and Space Science (ISSN 0004-640X)*, 217:11, 1994. doi:10.1007/BF00990014.

Kodama, T. and Arimoto, N. Origin of the colour-magnitude relation of elliptical galaxies. *Astronomy and Astrophysics*, 320:41, 1997.

Koester, B. P. et al. A maxbcg catalog of 13,823 galaxy clusters from the sloan digital sky survey. *The Astrophysical Journal*, 660:239, 2007. doi:10.1086/509599. (c) 2007: The American Astronomical Society.

Komatsu, E. and Seljak, U. Universal gas density and temperature profile. *Monthly Notices of the Royal Astronomical Society*, 327:1353, 2001. doi:10.1046/j.1365-8711.2001.04838.x.

Komatsu, E. and Seljak, U. The sunyaev-zel'dovich angular power spectrum as a probe of cosmological parameters. *Monthly Notice of the Royal Astronomical Society*, 336:1256, 2002. doi:10.1046/j.1365-8711.2002.05889.x.

Komatsu, E. et al. Seven-year wilkinson microwave anisotropy probe (wmap) observations: Cosmological interpretation. *eprint arXiv*, 1001:4538, 2010.

Kompaneets, A. The establishment of thermal equilibrium between quanta and electrons.

Sov Phys Jetp-Ussr, 4(5):730–737, 1957.

Koo, D. C. The deep project. *Highlights of Astronomy Vol. 11A*, 11:468, 1998.

Kotov, O. and Vikhlinin, A. Xmm-newton observations of evolution of cluster x-ray scaling relations at z=0.4-0.7. *The Astrophysical Journal*, 633:781, 2005. doi:10.1086/433170.

Krick, J. E. and Bernstein, R. A. Diffuse intracluster light in 10 clusters at 0.05 ¡ z ¡ 0.31. *Outskirts of Galaxy Clusters: Intense Life in the Suburbs. Edited by Antonaldo Diaferio*, page 220, 2004. doi:10.1017/S1743921304000468. ISBN: 052184908X.

Krick, J. E. and Bernstein, R. A. Diffuse optical light in galaxy clusters. ii. correlations with cluster properties. *The Astronomical Journal*, 134:466, 2007. doi:10.1086/518787.

Langlois, D. Brane cosmology. *Progress of Theoretical Physics Supplement*, 148:181, 2002. doi:10.1143/PTPS.148.181.

Larson, D. et al. Seven-year wilkinson microwave anisotropy probe (wmap) observations: Power spectra and wmap-derived parameters. *eprint arXiv*, 1001:4635, 2010.

Levine, E. S., Schulz, A. E. and White, M. Future galaxy cluster surveys: The effect of theory uncertainty on constraining cosmological parameters. *The Astrophysical Journal*, 577:569, 2002. doi:10.1086/342119.

Li, R., Mo, H. J., Fan, Z., van den Bosch, F. C. and Yang, X. Probing hot gas in galaxy groups through the sunyaev-zeldovich effect. *eprint arXiv*, 1006:4760, 2010. 22 pages, 14 figures, submitted to mnras.

Liao, Y.-W. et al. Amiba: Sunyaev-zel'dovich effect-derived properties and scaling relations of massive galaxy clusters. *The Astrophysical Journal*, 713:584, 2010. doi:10.1088/0004-637X/713/1/584.

Lima, M. and Hu, W. Self-calibration of cluster dark energy studies: Counts in cells. *Physical Review D*, 70:43504, 2004. doi:10.1103/PhysRevD.70.043504.

Lima, M. and Hu, W. Self-calibration of cluster dark energy studies: Observable-mass distribution. *Physical Review D*, 72:43006, 2005. doi:10.1103/PhysRevD.72.043006.

Linde, A. D. Eternal chaotic inflation. *Modern Physics Letters A*, 1:81, 1986. doi:10.1142/S0217732386000129.

Loken, C., Norman, M. L., Nelson, E., Burns, J., Bryan, G. L. and Motl, P. A universal temperature profile for galaxy clusters. *The Astrophysical Journal*, 579:571, 2002. doi:10.1086/342825.

Lopes, P. A. A., de Carvalho, R. R., Gal, R. R., Djorgovski, S. G., Odewahn, S. C., Mahabal, A. A. and Brunner, R. J. The northern sky optical cluster survey. iv. an intermediate-redshift galaxy cluster catalog and the comparison of two detection algorithms. *The Astronomical Journal*, 128:1017, 2004. doi:10.1086/423038.

Lopes, P. A. A., de Carvalho, R. R., Kohl-Moreira, J. L. and Jones, C. Nosocs in sdss. ii. mass calibration of low redshift galaxy clusters with optical and x-ray properties. *eprint arXiv*, 0907:3753, 2009.

Lueker, M. et al. Measurements of secondary cosmic microwave background anisotropies with the south pole telescope. *The Astrophysical Journal*, 719:1045, 2010. doi:10.1088/0004-637X/719/2/1045.

Lukić, Z., Reed, D., Habib, S. and Heitmann, K. The structure of halos: Implications for group and cluster cosmology. *The Astrophysical Journal*, 692:217, 2009. doi:10.1088/0004-637X/692/1/217.

Lumb, D. H. et al. The xmm-newton project. i. the x-ray luminosity-temperature relation at z>0.4. *Astronomy and Astrophysics*, 420:853, 2004. doi:10.1051/0004-6361:20035687.

Maddox, S. J., Efstathiou, G., Sutherland, W. J. and Loveday, J. Galaxy correlations on large scales. *Royal Astronomical Society*, 242:43P, 1990.

Majumdar, S. and Mohr, J. J. Self-calibration in cluster studies of dark energy: Combining the cluster redshift distribution, the power spectrum, and mass measurements. *The Astrophysical Journal*, 613:41, 2004. doi:10.1086/422829.

Malu, S. S., Subrahmanyan, R., Wieringa, M. and Narasimha, D. Compact sunyaev-zeldovich 'hole' in the bullet cluster. *eprint arXiv*, 1005:1394, 2010. 5 pages, 3 figures.

Maraston, C., Strömbäck, G., Thomas, D., Wake, D. A. and Nichol, R. C. Modelling the colour evolution of luminous red galaxies - improvements with empirical stellar spectra. *Monthly Notices of the Royal Astronomical Society: Letters*, 394:L107, 2009. doi:10.1111/j.1745-3933.2009.00621.x.

Markevitch, M. The l x-t relation and temperature function for nearby clusters revisited. *Astrophysical Journal v.504*, 504:27, 1998. doi:10.1086/306080.

Marrone, D. P. et al. Locuss: A comparison of sunyaev-zel'dovich effect and gravitational-lensing measurements of galaxy clusters. *The Astrophysical Journal Letters*, 701:L114, 2009. doi:10.1088/0004-637X/701/2/L114.

Martin and Long. Abell 2390 `http://www.spacetelescope.org/images/heic0814d/`. 2008.

Massardi, M., Ekers, R. D., Ellis, S. C. and Maughan, B. High angular resolution observation of the sunyaev–zel'dovich effect in the massive z 0.83 cluster cl j0152–1357. *The Astrophysical Journal Letters*, 718:L23, 2010. doi:10.1088/2041-8205/718/1/L23.

Massarotti, M., Iovino, A. and Buzzoni, A. A critical appraisal of the sed fitting method to estimate photometric redshifts. *Astronomy and Astrophysics*, 368:74, 2001. doi:10.1051/0004-6361:20000553.

Mather, J. C. Bolometer noise: nonequilibrium thoery. *Applied Optics*, 21:1125, 1982.

Maughan, B. J., Jones, L. R., Ebeling, H. and Scharf, C. The evolution of the cluster x-ray scaling relations in the wide angle rosat pointed survey sample at 0.6 ¡ z ¡ 1.0. *Monthly Notices of the Royal Astronomical Society*, 365:509, 2006. doi:10.1111/j.1365-2966.2005.09717.x.

Mazzotta, P., Rasia, E., Moscardini, L. and Tormen, G. Comparing the temperatures of galaxy clusters from hydrodynamical n-body simulations to chandra and xmm-newton observations. *Monthly Notices of the Royal Astronomical Society*, 354:10, 2004. doi:10.1111/j.1365-2966.2004.08167.x.

Melin, J.-B., Bartlett, J. G. and Delabrouille, J. Catalog extraction in sz cluster surveys: a matched filter approach. *Astronomy and Astrophysics*, 459:341, 2006. doi:10.1051/0004-6361:20065034.

Menanteau, F. et al. Southern cosmology survey. i. optical cluster detections and pre-

dictions for the southern common-area millimeter-wave experiments. *The Astrophysical Journal*, 698:1221, 2009. doi:10.1088/0004-637X/698/2/1221.

Menanteau, F. et al. Southern cosmology survey ii: Massive optically-selected clusters from 70 square degrees of the sze common survey area. *eprint arXiv*, 1002:2226, 2010.

Mennella, A. et al. Planck pre-launch status: Low frequency instrument calibration and expected scientific performance. *eprint arXiv*, 1001:4562, 2010.

Metzler, C. A. and Evrard, A. E. Simulations of the intracluster medium incorporating galactic feedback. *American Astronomical Society*, 25:1426, 1993. (c) 1993: American Astronomical Society.

Mewe, R., Gronenschild, E. H. B. M. and van den Oord, G. H. J. Calculated x-radiation from optically thin plasmas. v. *Astronomy and Astrophysics Supplement Series (ISSN 0365-0138)*, 62:197, 1985.

Mewe, R., Lemen, J. R. and van den Oord, G. H. J. Calculated x-radiation from optically thin plasmas. vi - improved calculations for continuum emission and approximation formulae for nonrelativistic average gaunt factors. *Astronomy and Astrophysics Supplement Series (ISSN 0365-0138)*, 65:511, 1986.

Miller, C. J., Melott, A. L. and Nichol, R. C. Wavelength doesn't matter: Optical vs. x-ray luminosities of galaxy clusters. *eprint arXiv*, page 12362, 1999.

Miller, C. J. et al. The c4 clustering algorithm: Clusters of galaxies in the sloan digital sky survey. *The Astronomical Journal*, 130:968, 2005. doi:10.1086/431357.

Milotti, E. 1/f noise: a pedagogical review. *arXiv*, physics.class-ph, 2002.

Motl, P. M., Hallman, E. J., Burns, J. O. and Norman, M. L. The integrated sunyaev-zeldovich effect as a superior method for measuring the mass of clusters of galaxies. *The Astrophysical Journal*, 623:L63, 2005. doi:10.1086/430144.

Mushotzky, R. F. and Scharf, C. A. The luminosity-temperature relation at z=0.4 for clusters of galaxies. *Astrophysical Journal Letters v.482*, 482:L13, 1997. doi:10.1086/310676.

Nagai, D. The impact of galaxy formation on the sunyaev-zel'dovich effect of galaxy clusters. *The Astrophysical Journal*, 650:538, 2006. doi:10.1086/506467.

NASA / WMAP Science Team. A timeline of the history of the universe. `http://map.gsfc.nasa.gov/media/060915/index.html`. 2010a.

NASA / WMAP Science Team. Images, CMB Images, Seven Year Microwave Sky: `http://wmap.gsfc.nasa.gov/media/101080/index.html`. 2010b.

Navarro, J. F., Frenk, C. S. and White, S. D. M. A universal density profile from hierarchical clustering. *Astrophysical Journal v.490*, 490:493, 1997. doi:10.1086/304888.

Newton, I. Philosophiae naturalis principia mathematica, vol. 1 - 4. *Colonia*, 1760.

Nord, B., Stanek, R., Rasia, E. and Evrard, A. E. Effects of selection and covariance on x-ray scaling relations of galaxy clusters. *Monthly Notices of the Royal Astronomical Society: Letters*, 383:L10, 2008. doi:10.1111/j.1745-3933.2007.00407.x.

Novicki, M. C., Sornig, M. and Henry, J. P. The evolution of the galaxy cluster luminosity-temperature relation. *The Astronomical Journal*, 124:2413, 2002. doi:10.1086/344162.

O'Shea, B. W., Nagamine, K., Springel, V., Hernquist, L. and Norman, M. L. Comparing amr and sph cosmological simulations. i. dark matter and adiabatic simulations. *The Astrophysical Journal Supplement Series*, 160:1, 2005. doi:10.1086/432645.

Ostriker, J. P., Bode, P. and Babul, A. A simple and accurate model for intracluster gas. *The Astrophysical Journal*, 634:964, 2005. doi:10.1086/497122.

Ostriker, J. P. and Vishniac, E. T. Effect of gravitational lenses on the microwave background, and 1146+111b,c. *Nature (ISSN 0028-0836)*, 322:804, 1986a. doi: 10.1038/322804a0.

Ostriker, J. P. and Vishniac, E. T. Generation of microwave background fluctuations from nonlinear perturbations at the era of galaxy formation. *Astrophysical Journal*, 306:L51, 1986b. doi:10.1086/184704.

Pace, F., Maturi, M., Bartelmann, M., Cappelluti, N., Dolag, K., Meneghetti, M. and Moscardini, L. Statistical properties of sz and x-ray cluster detections. *Astronomy and Astrophysics*, 483:389, 2008. doi:10.1051/0004-6361:200809550.

Park, C. and Gott, J. R. Simulation of deep one- and two-dimensional redshift surveys. *Royal Astronomical Society*, 249:288, 1991.

Percival, W. J. Cosmological structure formation in a homogeneous dark energy background. *Astronomy and Astrophysics*, 443:819, 2005. doi:10.1051/0004-6361:20053637.

Perlmutter, S. Supernovae, dark energy, and the accelerating universe. *Physics Today*, 56:53, 2003. doi:10.1063/1.1580050.

Perlmutter, S., Turner, M. S. and White, M. Constraining dark energy with type ia supernovae and large-scale structure. *Physical Review Letters*, 83:670, 1999a. doi:10.1103/PhysRevLett.83.670.

Perlmutter, S. et al. Measurements of and from 42 high-redshift supernovae. *The Astrophysical Journal*, 517:565, 1999b. doi:10.1086/307221.

Pierre, M. and Consortium, X.-L. Cosmological applications of the xmm-lss cluster sample. *36th COSPAR Scientific Assembly. Held 16 - 23 July 2006*, 36:1742, 2006.

Pires, S., Juin, J. B., Yvon, D., Moudden, Y., Anthoine, S. and Pierpaoli, E. Sunyaev-zel'dovich cluster reconstruction in multiband bolometer camera surveys. *Astronomy and Astrophysics*, 455:741, 2006. doi:10.1051/0004-6361:20053820.

Popesso, P., Böhringer, H., Brinkmann, J., Voges, W. and York, D. G. Rass-sdss galaxy clusters survey. i. the catalog and the correlation of x-ray and optical properties. *Astronomy and Astrophysics*, 423:449, 2004. doi:10.1051/0004-6361:20035818.

Postman, M., Lubin, L. M., Gunn, J. E., Oke, J. B., Hoessel, J. G., Schneider, D. P. and Christensen, J. A. The palomar distant clusters survey. i. the cluster catalog. *Astronomical Journal v.111*, 111:615, 1996. doi:10.1086/117811.

Press, W. H. and Schechter, P. Formation of galaxies and clusters of galaxies by self-similar gravitational condensation. *Astrophysical Journal*, 187:425, 1974. doi:10.1086/152650. A&AA ID. AAA011.162.012.

Ramella, M., Geller, M. J. and Huchra, J. P. The distribution of galaxies within the 'great wall'. *Astrophysical Journal*, 384:396, 1992. doi:10.1086/170882.

Rasia, E., Ettori, S., Moscardini, L., Mazzotta, P., Borgani, S., Dolag, K., Tormen, G., Cheng, L. M. and Diaferio, A. Systematics in the x-ray cluster mass estimators. *Monthly Notices of the Royal Astronomical Society*, 369:2013, 2006. doi:10.1111/j.1365-2966.2006.10466.x.

Rasia, E., Mazzotta, P., Borgani, S., Moscardini, L., Dolag, K., Tormen, G., Diaferio, A. and Murante, G. Mismatch between x-ray and emission-weighted temperatures in galaxy clusters: Cosmological implications. *The Astrophysical Journal*, 618:L1, 2005. doi:10.1086/427554.

Rasia, E., Tormen, G. and Moscardini, L. A dynamical model for the distribution of dark matter and gas in galaxy clusters. *Monthly Notices of the Royal Astronomical Society*, 351:237, 2004. doi:10.1111/j.1365-2966.2004.07775.x.

Reichardt, C. L. et al. Constraints on the high-ell power spectrum of millimeter-wave anisotropies from apex-sz. *The Astrophysical Journal*, 701:1958, 2009. doi:10.1088/0004-637X/701/2/1958.

Reiprich, T. H. The galaxy cluster x-ray luminosity-gravitational mass relation in the light of the wmap 3rd year data. *Astronomy and Astrophysics*, 453:L39, 2006. doi:10.1051/0004-6361:20065525.

Reiprich, T. H. and Böhringer, H. The mass function of an x-ray flux-limited sample of galaxy clusters. *The Astrophysical Journal*, 567:716, 2002. doi:10.1086/338753.

Renzini, A. Stellar population diagnostics of elliptical galaxy formation. *Annual Review of Astronomy & Astrophysics*, 44:141, 2006. doi:10.1146/annurev.astro.44.051905.092450.

Riess, A. et al. Observational evidence from supernovae for an accelerating universe and a cosmological constant. *The Astronomical Journal*, 116:1009–1009–1038–1038, 1999. doi:doi:10.1086/300499.

Rines, K., Geller, M. J. and Diaferio, A. Comparison of hectospec virial masses with sunyaev-zel'dovich effect measurements. *The Astrophysical Journal Letters*, 715:L180, 2010. doi:10.1088/2041-8205/715/2/L180.

Rizzo, D., Adami, C., Bardelli, S., Cappi, A., Zucca, E., Guiderdoni, B., Chincarini, G. and Mazure, A. Comparison of two optical cluster finding algorithms for the new generation of deep galaxy surveys. *Astronomy and Astrophysics*, 413:453, 2004. doi:10.1051/0004-6361:20031547.

Roncarelli, M., Moscardini, L., Branchini, E., Dolag, K., Grossi, M., Iannuzzi, F. and Matarrese, S. Imprints of primordial non-gaussianities in x-ray and sz signals from galaxy clusters. *Monthly Notices of the Royal Astronomical Society*, 402:923, 2010. doi:10.1111/j.1365-2966.2009.15978.x.

Rozo, E., Wechsler, R. H., Koester, B. P., McKay, T. A., Evrard, A. E., Johnston, D., Sheldon, E. S., Annis, J. and Frieman, J. A. Cosmological constraints from sdss maxbcg cluster abundances. *eprint arXiv*, page 3571, 2007. 10 pages, 6 figures, ApJ Submitted.

Rozo, E. et al. Improvement of the richness estimates of maxbcg clusters. *The Astrophysical Journal*, 703:601, 2009. doi:10.1088/0004-637X/703/1/601.

Rozo, i. Understand the mass-richness relation in galaxy clusters. 2010.

Ruhl, J. et al. The south pole telescope. *Millimeter and Submillimeter Detectors for*

Astronomy II. Edited by Jonas Zmuidzinas, 5498:11, 2004. doi:10.1117/12.552473.

Ruhl, J. E. et al. Improved measurement of the angular power spectrum of temperature anisotropy in the cosmic microwave background from two new analyses of boomerang observations. *The Astrophysical Journal*, 599:786, 2003. doi:10.1086/379345.

Rykoff, E. S. et al. The lx-m relation of clusters of galaxies. *Monthly Notices of the Royal Astronomical Society: Letters*, 387:L28, 2008. doi:10.1111/j.1745-3933.2008.00476.x.

Sarazin, C. L. X-ray emission from clusters of galaxies. *Reviews of Modern Physics*, 58:1, 1986. doi:10.1103/RevModPhys.58.1. (c) 1986: The American Physical Society.

Sayers, J. et al. A search for cosmic microwave background anisotropies on arcminute scales with bolocam. *The Astrophysical Journal*, 690:1597, 2009. doi:10.1088/0004-637X/690/2/1597.

Schäfer, B. M., Pfrommer, C., Bartelmann, M., Springel, V. and Hernquist, L. Detecting sunyaev-zel'dovich clusters with planck - i. construction of all-sky thermal and kinetic sz maps. *Monthly Notices of the Royal Astronomical Society*, 370:1309, 2006. doi:10.1111/j.1365-2966.2006.10552.x.

Scharf, C. A., Jones, L. R., Ebeling, H., Perlman, E., Malkan, M. and Wegner, G. The wide-angle rosat pointed x-ray survey of galaxies, groups, and clusters. i. method and first results. *Astrophysical Journal v.477*, 477:79, 1997. doi:10.1086/303698.

Schuecker, P. and Böhringer, H. Construction of x-ray cluster surveys and their spatial analyses. *Clusters of galaxies and the high redshift universe observed in X-rays*, page 21, 2001.

Schuecker, P. and Böhringer, H. m and 8 from the abundance and clustering of reflex clusters of galaxies. *Matter and Energy in Clusters of Galaxies*, 301:97, 2003. ISBN: 1-58381-149-4.

Sehgal, N., Bode, P., Das, S., Hernandez-Monteagudo, C., Huffenberger, K., Lin, Y.-T., Ostriker, J. P. and Trac, H. Simulations of the microwave sky. *The Astrophysical Journal*, 709:920, 2010. doi:10.1088/0004-637X/709/2/920.

Sehgal, N., Trac, H., Huffenberger, K. and Bode, P. Microwave sky simulations and projections for galaxy cluster detection with the atacama cosmology telescope. *The Astrophysical Journal*, 664:149, 2007. doi:10.1086/518880. (c) 2007: The American Astronomical Society.

Seljak, U. and Zaldarriaga, M. A line-of-sight integration approach to cosmic microwave background anisotropies. *Astrophysical Journal v.469*, 469:437, 1996. doi:10.1086/177793.

Serlemitsos, P. J., Smith, B. W., Boldt, E. A., Holt, S. S. and Swank, J. H. X-radiation from clusters of galaxies - spectral evidence for a hot evolved gas. *Astrophysical Journal*, 211:L63, 1977. doi:10.1086/182342. A&AA ID. AAA019.160.011.

Sharp, M. K. et al. A measurement of arcminute anisotropy in the cosmic microwave background with the sunyaev-zel'dovich array. *The Astrophysical Journal*, 713:82, 2010. doi:10.1088/0004-637X/713/1/82.

Shaw, L. D., Holder, G. P. and Bode, P. The impact of halo properties, energy feedback, and projection effects on the mass-sz flux relation. *The Astrophysical Journal*, 686:206,

2008. doi:10.1086/589849. (c) 2008: The American Astronomical Society.

Sheldon, E. S. et al. Weak-lensing measurements of 42 sdss/rass galaxy clusters. *The Astrophysical Journal*, 554:881, 2001. doi:10.1086/321395.

Sheldon, E. S. et al. Cross-correlation weak lensing of sdss galaxy clusters. i. measurements. *The Astrophysical Journal*, 703:2217, 2009. doi:10.1088/0004-637X/703/2/2217.

Sheth, R. K. and Tormen, G. Large-scale bias and the peak background split. *Monthly Notices of the Royal Astronomical Society*, 308:119, 1999. doi:10.1046/j.1365-8711.1999.02692.x.

Skibba, R. A., van den Bosch, F. C., Yang, X., More, S., Mo, H. and Fontanot, F. Are brightest halo galaxies central galaxies? *eprint arXiv*, 1001:4533, 2010. 17 pages, 11 figures. MNRAS, in press.

Spergel, D. N. et al. Wilkinson microwave anisotropy probe (wmap) three year results: Implications for cosmology. *arXiv*, astro-ph, 2006. doi:10.1086/513700.

Springel, V. The cosmological simulation code gadget-2. *Monthly Notices of the Royal Astronomical Society*, 364:1105, 2005. doi:10.1111/j.1365-2966.2005.09655.x.

Springel, V., Frenk, C. S. and White, S. D. M. The large-scale structure of the universe. *Nature*, 440:1137, 2006. doi:10.1038/nature04805.

Springel, V., White, M. and Hernquist, L. Hydrodynamic simulations of the sunyaev-zeldovich effect(s). *The Astrophysical Journal*, 549:681, 2001. doi:10.1086/319473. (c) 2001: The American Astronomical Society.

Springel, V., Yoshida, N. and White, S. D. M. Gadget: A code for collisionless and gas-dynamical cosmological simulations. *arXiv*, astro-ph, 2000. doi:10.1016/S1384-1076(01)00042-2.

Springel, V. et al. Simulations of the formation, evolution and clustering of galaxies and quasars. *Nature*, 435:629, 2005. doi:10.1038/nature03597. (c) 2005: Nature.

Stanek, R., Evrard, A. E., Böhringer, H., Schuecker, P. and Nord, B. The x-ray luminosity-mass relation for local clusters of galaxies. *The Astrophysical Journal*, 648:956, 2006. doi:10.1086/506248. (c) 2006: The American Astronomical Society.

Stanek, R., Rasia, E., Evrard, A. E., Pearce, F. and Gazzola, L. Massive halos in millennium gas simulations: Multivariate scaling relations. *The Astrophysical Journal*, 715:1508, 2010. doi:10.1088/0004-637X/715/2/1508.

Stanek, R., Rudd, D. and Evrard, A. E. The effect of gas physics on the halo mass function. *Monthly Notices of the Royal Astronomical Society: Letters*, 394:L11, 2009. doi:10.1111/j.1745-3933.2008.00597.x.

Staniszewski, Z. et al. Galaxy clusters discovered with a sunyaev-zel'dovich effect survey. *The Astrophysical Journal*, 701:32, 2009. doi:10.1088/0004-637X/701/1/32.

Steigman, G., Schramm, D. N. and Gunn, J. E. Cosmological limits to the number of massive leptons. *Physics Letters B*, 66:202, 1977. doi:10.1016/0370-2693(77)90176-9.

Sunyaev, R. A. and Zeldovich, I. B. Microwave background radiation as a probe of the contemporary structure and history of the universe. *In: Annual review of astronomy and astrophysics. Volume 18. (A81-20334 07-90) Palo Alto*, 18:537, 1980. doi:10.1146/

annurev.aa.18.090180.002541. A&AA ID. AAA028.162.060.

Sunyaev, R. A. and Zeldovich, Y. B. The observations of relic radiation as a test of the nature of x-ray radiation from the clusters of galaxies. *Comments on Astrophysics and Space Physics*, 4:173, 1972. A&AA ID. AAA008.160.027.

Taburet, N., Douspis, M. and Aghanim, N. The sunyaev-zel'dovich contribution in cmb analyses. *Monthly Notices of the Royal Astronomical Society*, 404:1197, 2010. doi:10.1111/j.1365-2966.2010.16372.x.

Tegmark, M. and de Oliveira-Costa, A. Removing point sources from cosmic microwave background maps. *Astrophysical Journal Letters v.500*, 500:L83, 1998. doi:10.1086/311410.

Tegmark, M. et al. Cosmological constraints from the sdss luminous red galaxies. *Physical Review D*, 74:123507, 2006. doi:10.1103/PhysRevD.74.123507.

The ACT Collaboration. The atacama cosmology telescope: A measurement of the 600 $< \ell <$ 8000 cosmic microwave background power spectrum at 148 ghz. *eprint arXiv*, 1001:2934, 2010. 15 pages, 8 figures. Submitted to ApJ.

The Dark Energy Survey Collaboration. The dark energy survey. *eprint arXiv*, page 10346, 2005.

The SPT Team. Secondary anisotropy of the Cosmic Microwave Background detected with the South Pole Telescope `http://cfcp.uchicago.edu/research/highlights/index.html`. 2010.

Thomas, P. A. et al. The structure of galaxy clusters in various cosmologies. *Monthly Notices of the Royal Astronomical Society*, 296:1061, 1998. doi:10.1046/j.1365-8711.1998.01491.x.

Tinker, J., Kravtsov, A. V., Klypin, A., Abazajian, K., Warren, M., Yepes, G., Gottlöber, S. and Holz, D. E. Toward a halo mass function for precision cosmology: The limits of universality. *The Astrophysical Journal*, 688:709, 2008. doi:10.1086/591439.

Tinker, J. L. and Ryden, B. S. The influence of triaxial halos on collisionless galactic disks. *eprint arXiv*, page 9165, 2002.

Truemper, J. Rosat - a new look at the x-ray sky. *Science (ISSN 0036-8075)*, 260:1769, 1993. doi:10.1126/science.260.5115.1769.

Vale, C. and White, M. Finding clusters in sz surveys. *arXiv*, astro-ph, 2005. doi:10.1016/j.newast.2005.07.005.

Vanderlinde, K. et al. Galaxy clusters selected with the sunyaev-zel'dovich effect from 2008 south pole telescope observations. *eprint arXiv*, 1003:3, 2010.

Ventimiglia, D. A., Voit, G. M., Donahue, M. and Ameglio, S. Substructure and scatter in the mass-temperature relations of simulated clusters. *The Astrophysical Journal*, 685:118, 2008. doi:10.1086/590485. (c) 2008: The American Astronomical Society.

Viana, P. T. P. and Liddle, A. R. Perturbation evolution in cosmologies with a decaying cosmological constant. *Physical Review D (Particles*, 57:674, 1998. doi:10.1103/PhysRevD.57.674.

Vikhlinin, A., Markevitch, M., Murray, S. S., Jones, C., Forman, W. and Speybroeck,

L. V. Chandra temperature profiles for a sample of nearby relaxed galaxy clusters. *The Astrophysical Journal*, 628:655, 2005. doi:10.1086/431142.

Vikhlinin, A., Speybroeck, L. V., Markevitch, M., Forman, W. R. and Grego, L. Evolution of the cluster x-ray scaling relations since z $>$ 0.4. *The Astrophysical Journal*, 578:L107, 2002. doi:10.1086/344591.

Vikhlinin, A. et al. Chandra cluster cosmology project iii: Cosmological parameter constraints. *The Astrophysical Journal*, 692:1060–1060–1074–1074, 2. doi:doi:10.1088/0004-637X/692/2/1060.

Visvanathan, N. and Sandage, A. The color-absolute magnitude relation for e and s0 galaxies. i - calibration and tests for universality using virgo and eight other nearby clusters. *Astrophysical Journal*, 216:214, 1977. doi:10.1086/155464. A&AA ID. AAA020.158.021.

Voges, W. et al. The rosat all-sky survey bright source catalogue. *Astronomy and Astrophysics*, 349:389, 1999.

Voit, G. M. Expectations for evolution of cluster scaling relations. *Advances in Space Research*, 36:701, 2005a. doi:10.1016/j.asr.2005.02.042.

Voit, G. M. Tracing cosmic evolution with clusters of galaxies. *Reviews of Modern Physics*, 77:207, 2005b. doi:10.1103/RevModPhys.77.207.

von der Linden, A., Best, P. N., Kauffmann, G. and White, S. D. M. How special are brightest group and cluster galaxies? *Monthly Notices of the Royal Astronomical Society*, 379:867, 2007. doi:10.1111/j.1365-2966.2007.11940.x.

Warren, M. S., Abazajian, K., Holz, D. E. and Teodoro, L. Precision determination of the mass function of dark matter halos. *The Astrophysical Journal*, 646:881, 2006. doi:10.1086/504962.

Weinberg, D. H., Davé, R., Katz, N. and Hernquist, L. Galaxy clustering and galaxy bias in a cdm universe. *The Astrophysical Journal*, 601:1, 2004. doi:10.1086/380481.

Wheeler, J. A. Geons. *Physical Review*, 97:511, 1955. doi:10.1103/PhysRev.97.511.

White, M. Studying clusters with planck. *The Astrophysical Journal*, 597:650, 2003. doi:10.1086/381218.

White, M., Carlstrom, J. E., Dragovan, M. and Holzapfel, W. L. Interferometric observation of cosmic microwave background anisotropies. *The Astrophysical Journal*, 514:12, 1999. doi:10.1086/306911.

White, M., Hernquist, L. and Springel, V. Simulating the sunyaev-zeldovich effect(s): Including radiative cooling and energy injection by galactic winds. *The Astrophysical Journal*, 579:16, 2002. doi:10.1086/342756. (c) 2002: The American Astronomical Society.

White, M. and Majumdar, S. Point sources in the context of future sz surveys. *The Astrophysical Journal*, 602:565, 2004. doi:10.1086/381162. (c) 2004: The American Astronomical Society.

White, S. D. M., Efstathiou, G. and Frenk, C. S. The amplitude of mass fluctuations in the universe. *Royal Astronomical Society*, 262:1023, 1993a.

White, S. D. M., Frenk, C. S., Davis, M. and Efstathiou, G. Clusters, filaments, and voids

in a universe dominated by cold dark matter. *Astrophysical Journal*, 313:505, 1987. doi:10.1086/164990.

White, S. D. M., Navarro, J. F., Evrard, A. E. and Frenk, C. S. The baryon content of galaxy clusters: a challenge to cosmological orthodoxy. *Nature*, 366:429, 1993b. doi: 10.1038/366429a0.

White, S. D. M. and Rees, M. J. Core condensation in heavy halos - a two-stage theory for galaxy formation and clustering. *Royal Astronomical Society*, 183:341, 1978. A&AA ID. AAA021.162.070.

Wright, E. L. Distortion of the microwave background by a hot intergalactic medium. *Astrophysical Journal*, 232:348, 1979. doi:10.1086/157294. A&AA ID. AAA026.162.006.

Wu, H.-Y., Rozo, E. and Wechsler, R. H. Annealing a follow-up program: Improvement of the dark energy figure of merit for optical galaxy cluster surveys. *The Astrophysical Journal*, 713:1207, 2010. doi:10.1088/0004-637X/713/2/1207.

Yang, X., Mo, H. J. and van den Bosch, F. C. Constraining galaxy formation and cosmology with the conditional luminosity function of galaxies. *Monthly Notice of the Royal Astronomical Society*, 339:1057, 2003. doi:10.1046/j.1365-8711.2003.06254.x.

York, D. G. et al. The sloan digital sky survey: Technical summary. *The Astronomical Journal*, 120:1579, 2000. doi:10.1086/301513.

Zeldovich, Y. B. and Sunyaev, R. A. The interaction of matter and radiation in a hot-model universe. *Astrophysics and Space Science*, 4:301, 1969. doi:10.1007/BF00661821.

Zentner, A. R. The excursion set theory of halo mass functions, halo clustering, and halo growth. *International Journal of Modern Physics D*, 16:763, 2007. doi:10.1142/S0218271807010511.

Zhang, P., Pen, U.-L. and Trac, H. Precision era of the kinetic sunyaev-zel'dovich effect: simulations, analytical models and observations and the power to constrain reionization. *Monthly Notices of the Royal Astronomical Society*, 347:1224, 2004. doi: 10.1111/j.1365-2966.2004.07298.x.

Zheng, Z., Zehavi, I., Eisenstein, D. J., Weinberg, D. H. and Jing, Y. P. Halo occupation distribution modeling of clustering of luminous red galaxies. *The Astrophysical Journal*, 707:554, 2009. doi:10.1088/0004-637X/707/1/554.

Zwicky, F. On the masses of nebulae and of clusters of nebulae. *Astrophysical Journal*, 86:217, 1937. doi:10.1086/143864.